Linear and Non-Linear Spin-to-Charge Conversion in a Quantum Point Contact

DISSERTATION ZUR ERLANGUNG DES
DOKTORGRADES DER NATURWISSENSCHAFTEN
(DR. RER. NAT.) DER FAKULTÄT FÜR PHYSIK
DER UNIVERSITÄT REGENSBURG

vorgelegt von

Benedikt Grünewald

aus Neu-Ulm

im Jahr 2024

Promotionsgesuch eingereicht am: 10.04.2024

Die Arbeit wurde angeleitet von: Prof. Dr. Mariusz Ciorga

Prüfungsausschuss:

Vorsitzender:	Prof. Dr. Jaroslav Fabian
Erstgutachter:	Prof. Dr. Mariusz Ciorga
Zweitgutachter:	Prof. Dr. Jörg Wunderlich
Weiterer Prüfer:	Prof. Dr. Franz J. Gießibl

Contents

Chapter 1

Introduction

1.1 Historical Background of Spintronics

Spintronics is a vast field ranging over many phenomena [1], which emerged many decades ago. In spintronics, the electron's spin degree of freedom plays a significant role in addition to its charge. At the heart lies the ability to control and manipulate the electron spin. This often refers to the orientation of a spin ensemble, which can be utilized to realise various devices such as magnetic random access memory [2, 3] or magnetic read heads [4, 5] for hard-disk drives.

Although the field of spintronics did not exist in 1857, it was understood that the resistance of bulk nickel and iron could be manipulated by changing the direction of an external magnetic field [6]. This first observation of magnetoresistance, where the resistance of a material can be altered in the presence of a magnetic field, is based on spin-dependent scattering due to spin-orbit coupling in the material [7]. At the time these experiments were conducted, the electron spin and, thus, both spin-orbit coupling and the physical origin of the magnetoresistance were unknown.

It was not until 1922 that the famous Stern-Gerlach experiment showed experimentally that the electron spin exists [8–10]. In this experiment, a beam of silver atoms was directed through an inhomogeneous magnetic field and detected using a glass plate. The gradient in magnetic field caused the atom beam to deviate from its original trajectory, resulting in a beam splitting into two: one for silver atoms with a spin-up configuration and one for silver atoms with a spin-down configuration, which contradicted predictions made from classical physics. This experiment demonstrated that individual silver atoms possess discrete magnetic moments, which are now known to depend on the atom's spin. In addition, this was the first time that the quantum-mechanical ground state of a system could be determined directly.

Two fundamental spintronic effects are the tunneling magnetoresistance (TMR) effect and the giant magnetoresistance (GMR) effect. The former was first measured in 1975 by Jullière in Fe/Ge/Co junctions [11]. The TMR effect involves two ferromagnetic electrodes that are separated by a thin tunnel barrier. Upon applying a voltage, the tunneling current through the junction changes by varying the relative orientation of the two ferromagnetic layers. This motivates *spin valve* measurements, where the relative change in resistance between a parallel R_P and an antiparallel R_AP configuration can be measured as $\mathrm{TMR} = \Delta R/R_\mathrm{P} = (R_\mathrm{P} - R_\mathrm{AP})/R_\mathrm{P}$. This way, the electric signal through the junction can be manipulated by means of an external magnetic field. Butler *et al.* [12] predicted a large magnetoresistance using MgO as a tunnel barrier, which eventually led to high TMR values at room temperature for CoFeB/MgO/CoFeB junctions [13].

The giant magnetoresistance (GMR) effect was discovered in 1988 independently by Grünberg [14] and Fert [15], for which they were awarded the Nobel prize in 2007 [16]. The GMR effect can be achieved by sandwiching a thin nonmagnetic, metallic layer between two ferromagnets. In the original works by Grünberg and Fert, Fe/Cr/Fe multilayers were used. The resistance of the system depends on the relative orientation of the two ferromagnetic layers. In a parallel state, the resistance is low, while the resistance is large in an antiparallel configuration.

Using the GMR or TMR effect, various devices can be realized [17]. The main advantages are nonvolatility and the fact that the magnetization state is retained after the power of the device is switched off. For most applications a large magnetoresistance is required.

To obtain a large magnetoresistance, materials with a large spin polarization are of interest. This refers to the fact that there is a different number of spin up electrons $N_\uparrow$ than spin down electrons $N_\downarrow$ at the Fermi energy E_F. For this reason, half-metallic magnets [18, 19] such as Heusler alloys [20], manganite perovskites [21] or ferromagnetic oxides [20, 22] are of great interest. These materials, however, exhibit low compatibility with semiconductors. Therefore, diluted magnetic semiconductors (DMS), which represent another group of magnets, have gathered considerable interest. In a DMS, a nonmagnetic semiconductor, such as GaAs, is doped with magnetic elements, such as Mn, in order to obtain magnetic properties. This approach enables compatibility between the magnetic components of a spintronic device with other semiconductor components. GaMnAs, which falls into the group of DMS [23–25], is the ferromagnetic material used in this work, which allows to fabricate all-semiconductor devices.

One possible application for new (spintronic) devices is to replace the

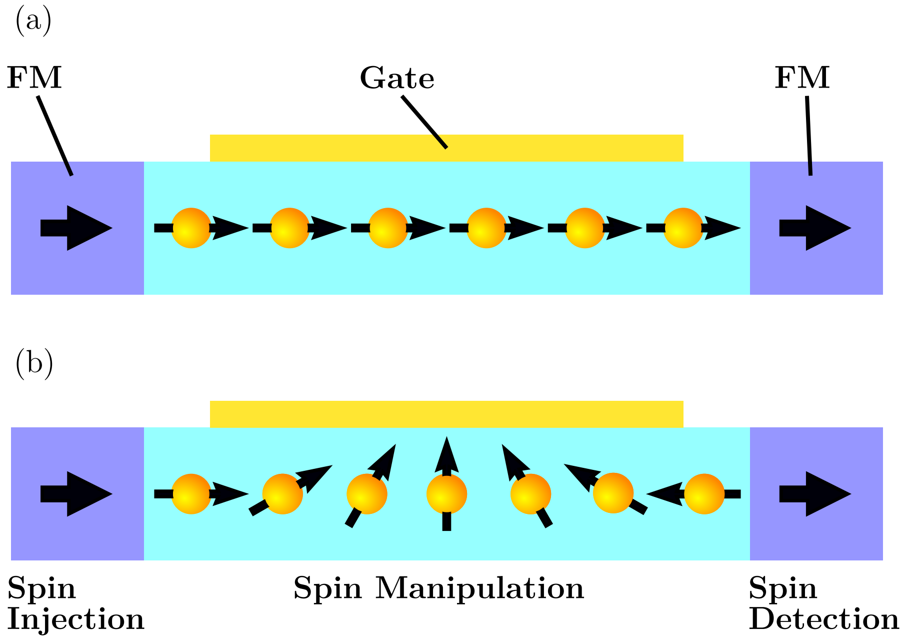

Figure 1.1: Spin analog of a field-effect transistor. A spin-polarized current is injected from the left ferromagnet (FM) into a nonmagnet towards a ferromagnetic drain, where the spins are detected. By means of a gate voltage, the spin-orbit coupling in the nonmagnet can be varied, which causes the spin ensemble to precess. (a) If the spin ensemble reaches the drain in a configuration parallel to the drain's magnetization, the current is large. (b) In the case of an antiparallel configuration, the current is low. Adapted from [28].

field-effect transistor in logic circuits. In a field-effect transistor, the flow of electrons in a conducting channel between the source and the drain can be switched "ON" and "OFF" through the usage of a gate [26]. A spin-analog of the field-effect transistor was proposed in 1989 by Datta and Das [27], and the device is sketched in figure 1.1. It consists of a nonmagnetic (NM) transport channel (shown in cyan), sandwiched between two ferromagnets (FM), which serve as the source and drain contacts, respectively. Similar to a field-effect transistor, the current flow through the transport channel can be controlled with a gate, which however manipulates the spin and not the charge of the electrons.

The left FM is utilized for spin injection. From here, a spin-polarized current is driven into the transport channel, whereas the ferromagnetic drain contact on the right serves for spin detection. In the NM, the spins precess about the spin-orbit coupling vector, whose magnitude can be modified by applying a gate voltage. As a result, the precession rate can be controlled using a gate.

At the transition between the NM and the FM on the right, the relative orientation between the spins and the magnetization of the right FM is of crucial importance. A parallel configuration, shown in (a), results in a large current, while an antiparallel configuration, shown in (b), causes a low current. Therefore, the current flow through the device can be controlled by varying the gate voltage, which serves as a switch between "ON" and "OFF".

To realize the spin transistor, four requirements must be met: efficient spin injection and spin transport, spin manipulation, and spin detection. All-electrical spin injection and spin detection have already been realized in various (semiconductor) materials, utilizing various ferromagnetic (half-) metals for spin injection [29–35]. Our group has realized all-electrical, all-semiconductor devices for spin injection and spin detection [36] in an inverted (Al,Ga)As/GaAs 2DEG [37] and in an (In,Ga)As quantum well [38]. While controlled spin manipulation has been demonstrated in our group by Eberle *et al.* [39], this work adresses spin detection.

According to Moore's law [40], the number of transistors in an integrated circuit grows exponentially with time [41], which is a phenomenological observation that requires miniaturization of the components [42]. This introduces several challenges. The spin transistor requires a clear single magnetic domain in the FM. Decreasing the size of the device and, therefore, the size of the FM, has a drastic impact on its magnetic characteristics. Therefore, it is advantageous to explore alternative means for spin detection that do not rely on FMs. One such alternative for spin detection is a quantum point contact (QPC).

This work investigates spin detection by means of a QPC, which acts as an energy barrier. Due to a splitting in quasichemical potential between spin-up and spin-down electrons, the transmission probability through the QPC is spin dependent. This enables linear and nonlinear *spin-to-charge conversion* for spin detection, which are both measured as a voltage-drop across the QPC.

1.2 Thesis Outline

This thesis investigates the detection of a spin accumulation by means of linear and nonlinear spin-to-charge conversion in a quantum point contact (QPC).

By employing a spin Esaki diode, comprised of GaMnAs and AlGaAs/GaAs, we inject a nonequilibrium spin accumulation into an inverted GaAs/AlGaAs two-dimensional electron gas (2DEG). From here, the spin accumulation diffuses into all directions.

Utilizing a second spin Esaki diode, the spin accumulation can be detected with the spin valve method, which provides an established and well-known experimental way of spin detection. The spin valve method requires sharp magnetic switching of the magnetization of the GaMnAs, which conflicts with miniaturization. The alternative of utilizing linear and nonlinear spin-to-charge conversion in a QPC for spin detection, which does not require a ferromagnet, is investigated here.

Chapter 2 shows the theoretical background of spin injection. Here, a spin accumulation is treated in terms of the spin quasichemical potential μ_s, which gives access to the basic concepts of spin transport. In addition, the basics of spin detection are described.

Chapter 3 introduces fundamental concepts of two-dimensional and one-dimensional transport. This includes the 2DEG and the QPC. For the latter, the characteristic step-like conductance behavior is derived.

Chapter 4 provides an overview of the material used, sample design and fabrication as well as measurement methods. The spin Esaki diode, which is used for spin injection, is described in detail. In addition, the layout of the heterostructure used in this work is explained. The cleanroom practise for sample fabrication required standard methods for nanofabrication, which are covered in detail. In addition, the measurement setup is described.

Chapter 5 shows the experimental characterization of the wafer's spin injection and spin transport properties by well established means, i.e., by (distance-resolved) spin valve measurements. In addition, the realization of the QPC is discussed. This includes a suitable split-gate design as well as a characterization of the QPC's parameters.

Chapter 6 comprises the main part of this work: linear and nonlinear spin-to-charge conversion in a QPC. First, the theory of spin-to-charge conversion is covered and the measurement setup is shown.

Next, measurement results for nonlinear spin-to-charge conversion are presented, followed by a section on the results of linear spin-to-charge conversion experiments. In both cases, the focus is on demonstrating that the measured signal is spin-related. In the case of nonlinear spin-to-charge conversion, this includes distance-resolved measurements and the use of out-of-plane magnetic fields, which suppress the spin-related signal. In the case of linear spin-to-charge conversion, the measured signal is compared with theoretical predictions. Finally, the results of nonlinear and linear spin-to-charge conversion experiments are compared.

Chapter 7 gives a summary of the experimental results.

Chapter 2

Theoretical Background of Spin Injection

2.1 Resistor Model

At thermodynamic equilibrium, the sum of drift and diffusion currents in an electron gas vanishes. From this, the Einstein relation can be derived, which connects the conductivity σ with the density of states $\mathcal{D}(E_\mathrm{F})$ and the diffusion constant D [28]:

$$\sigma = e^2\mathcal{D}(E_\mathrm{F})D, \tag{2.1}$$

where e is the electron charge. In a ferromagnet (FM), spin-up and spin-down electrons have different densities of states and, therefore, different conductivities. Based on the work of Mott [43, 44], which treats spin-up and spin-down electrons as separate channels, the process of spin injection from a FM into a nonmagnet (NM) can be described by the simple resistor model, which is shown in figure 2.1. In the resistor model spin-up and spin-down channels are treated as two resistors in a parallel circuit, with $R_\uparrow$ and $R_\downarrow$ representing the resistance for each respective channel. In a FM-NM-FM junction, the total resistance R

$$\frac{1}{R} = \frac{1}{R_\uparrow} + \frac{1}{R_\downarrow} \tag{2.2}$$

depends on the relative orientation of the magnetization of the FMs, which are assumed to be aligned either parallel or antiparallel. The spin current I_s in the NM,

$$I_s = I_\uparrow - I_\downarrow = (\Delta V_{\mathrm{NM},\uparrow} - \Delta V_{\mathrm{NM},\downarrow})/R_\mathrm{NM}, \tag{2.3}$$

is the difference in current between spin-up $I_\uparrow$ and spin-down $I_\downarrow$ electrons. R_NM is the resistance of the NM and $\Delta V_{\mathrm{NM},\uparrow/\downarrow}$ is the voltage drop for the respective spin in the NM, which depends on the relative magnetization of the FMs. The resistor model, which was treated extensively by Schmidt *et al.* [45], highlights the *conductivity mismatch problem* [46]: if the resistance of the NM greatly exceeds the resistance of the FM, the spin current I_s inside the NM will vanish (right side in figure 2.1). It was suggested by Rashba [47], that introducing a tunnel barrier (TB) between the FM and the NM would solve this problem. The resistor model, as presented here, neglects events which can change the spins orientation. As figure 2.1 suggests, spin-up and spin-down electrons have different chemical potentials at the FM-NM interface. In the next section, spins are treated in terms of the *quasichemical potential* close to the FM-NM interface.

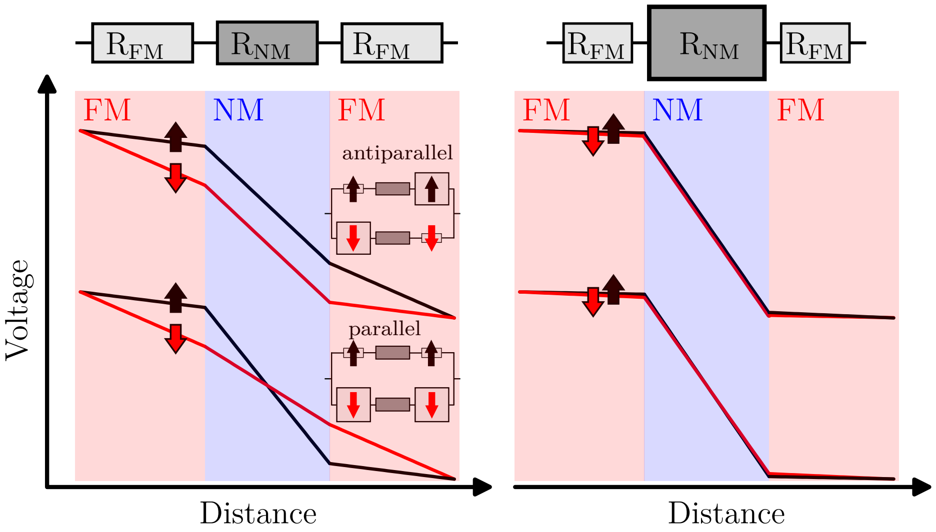

Figure 2.1: Voltage drop of spin-up and spin-down electrons, which are treated as two parallel circuits in a FM-NM-FM junction. Based on the relative orientation of the two FMs, the total resistance of the junction changes. If the resistance of the NM is much larger than the resistance of the FM, the spin current inside the NM vanishes. Adapted from [45].

2.2 Spin Current and Diffusion

Before adressing spin injection from a FM into a NM by electrial means, basic concepts of spin transport have to be introduced. Here, the notation used by Fabian [48] will be adapted. In contrast to the electron density n, the spin density s is not preserved with

$$\begin{aligned} n &= n_\uparrow + n_\downarrow \\ s &= n_\uparrow - n_\downarrow, \end{aligned} \tag{2.4}$$

where $n_\uparrow$ and $n_\downarrow$ are the densities for spin-up and spin-down electrons, respectively. From the random walk theory, the drift-diffusion equation for s reads

$$\frac{\partial s}{\partial t} + \frac{\partial}{\partial x}\left(-\mu_\mathrm{e} E s - D\frac{\partial s}{\partial x}\right) = \frac{\partial s}{\partial t} + \frac{\partial}{\partial x} J_s = -\frac{s}{\tau_s}, \tag{2.5}$$

with μ_e and E being the mobility and electric field, respectively. D is the diffusion constant, τ_s the spin relaxation time and J_s the spin current.

Suppose a steady state spin current at $x = 0$ and zero electric field, i.e., $J_s(0) = -D\,\partial s/\partial x|_{x=0} = J_{s0}$. In this case, the solution to the diffusion equation is

$$s(x) = J_{s0}\frac{L_s}{D} e^{-x/L_s} = s_0\, e^{-x/L_s}. \tag{2.6}$$

The *spin diffusion length* L_s, which is related to the diffusion constant and spin relaxation time by

$$L_s = \sqrt{D\tau_s} \tag{2.7}$$

gives a characteristic lengthscale over which spins decay exponentially in space.

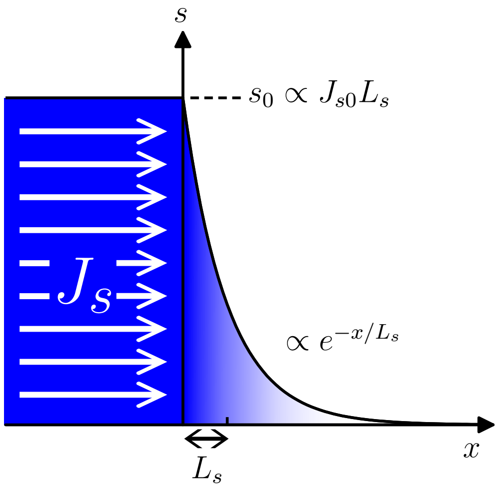

Figure 2.2: By means of a spin current J_s, spin is accumulated at $x = 0$. The spin accumulation is proportional to the spin current as well as the spin diffusion length and decays exponentially. While the spin current can be generated by any source, this figure suggests a flow of spins from a ferromagnetic region into a nonmagnet. Adapted from [48].

Instead of focusing directly on the spin density s, one can also get insights into spin dynamics by considering the *quasichemical potential* $\mu(x)$, which emerges away from equilibrium. For degenerate semiconductors, one can assume local charge neutrality, i.e., no charge accumulation inside the semiconductor. As a consequence, the quasichemical potential fully balances the electrostatic potential: $\mu(x) = -\phi(x)$. In a FM, the condition reads $\mathcal{D}(\mu + \phi) + \mathcal{D}_s \mu_s = 0$. The quasichemical potential can be different for spin-up and spin-down electrons and the total quasichemical potential μ and the spin-quasichemical potential μ_s are defined as

$$\begin{aligned} \mu &= \frac{1}{2}(\mu_\uparrow + \mu_\downarrow) \\ \mu_s &= \frac{1}{2}(\mu_\uparrow - \mu_\downarrow). \end{aligned} \tag{2.8}$$

In general, one can define any spin-resolved variable as $\mathcal{X}_s = \mathcal{X}_\uparrow - \mathcal{X}_\downarrow$, including the conductivity σ or density of states $\mathcal{D}$. The current of a corresponding spin species is related to a gradient of the quasichemical potential by

$$j_{\uparrow/\downarrow} = \sigma_{\uparrow/\downarrow} \nabla \mu_{\uparrow/\downarrow} \tag{2.9}$$

with the respective conductivites $\sigma_{\uparrow/\downarrow}$. Using equation 2.9, one finds

$$j = j_\uparrow + j_\downarrow = \sigma \nabla \mu + \sigma_s \nabla \mu_s \tag{2.10a}$$

$$j_s = j_\uparrow - j_\downarrow = \sigma_s \nabla \mu + \sigma \nabla \mu_s. \tag{2.10b}$$

Equation 2.10b describes spin-to-charge coupling in a FM, where $\sigma_s \neq 0$: an applied voltage leads to a spin current, while $\nabla \mu_s \neq 0$ leads to a charge current (see equation 2.10a). In a NM, the conductivities for spin-up and spin-down electrons are equal, $\sigma_\uparrow = \sigma_\downarrow$. In this case, a spin current is driven by a gradient in the spin quasichemical potential.

Using local charge neutrality, one obtains an expression for the nonequilibrium spin accumulation δs

$$\delta s = s - s_0 = 4 \mathrm{e} \mu_s \frac{\mathcal{D}_\uparrow \mathcal{D}_\downarrow}{\mathcal{D}}, \tag{2.11}$$

where $\mathcal{D}_{\uparrow/\downarrow}$ is the density of states for a given spin species and e is the electron charge. Due to the linear relation with δs, the spin quasichemical potential is also called *spin accumulation*.

Solving equation 2.10a for $\nabla \mu$, inserting into equation 2.10b and using equation 2.11, the spin current becomes

$$j_s = P_\sigma j + 4 \nabla \mu_s \frac{\sigma_\uparrow \sigma_\downarrow}{\sigma} \tag{2.12}$$

with the conductivity spin polarization $P_\sigma = \sigma_s / \sigma$. Using the steady state drift-diffusion equation 2.5 ($\partial J_s / \partial x = -\delta s / \tau_s$) gives a diffusion equation for μ_s:

$$\nabla^2 \mu_s = \frac{\mu_s}{L_s^2} \tag{2.13}$$

with the generalized diffusion length

$$L_s = \sqrt{\overline{D}\tau_s} \tag{2.14}$$

and the generalized diffusion constant

$$\overline{D} = \frac{\mathcal{D}}{\mathcal{D}_\uparrow/D_\downarrow + \mathcal{D}_\downarrow/D_\uparrow}. \tag{2.15}$$

2.3 Spin Injection and Detection

After Aronov proposed coupling between spin and charge in 1976 [49], Johnson and Silsbee developed the thermodynamics of magnetization transport across a FM-NM junction [50, 51]. The theory of spin injection was then treated by van Son *et al.* [52], Valet and Fert [53], Fert and Jaffres [54] and by various other authors [46, 47, 55–59].

Before adressing spin detection, spin injection through a FM-TB-NM junction will be discussed using the *standard model of spin injection.* In this section, the notation used by Fabian [48] and Žutić [60] will be adapted.

Spin Injection

Under the assumption of a continuous spin current j_s, an expression for the spin current polarization $P_j = j_s/j$ can be derived.

Considering a FM-TB-NM junction at x=0, with the FM located on the left (i.e., x<0) and the NM on the right (i.e., x>0) side of the TB, and solving equation 2.13 for the NM/FM region gives

$$\begin{aligned} \mu_{s\mathrm{N}} &= \mu_{s\mathrm{N}}(0)e^{-x/L_{s\mathrm{N}}} \qquad &&\text{(NM region)} \\ \mu_{s\mathrm{F}} &= \mu_{s\mathrm{F}}(0)e^{x/L_{s\mathrm{F}}} \qquad &&\text{(FM region)}, \end{aligned} \tag{2.16}$$

where $L_{s\mathrm{N}/s\mathrm{F}}$ is the spin diffusion length for the NM and the FM, respectively. Inserting the gradient of this result into equation 2.12 gives the spin current polarization at the junction

$$\begin{aligned} P_{j\mathrm{N}}(0) &= -\frac{1}{j}\frac{\mu_{s\mathrm{N}}(0)}{R_\mathrm{N}} \\ P_{j\mathrm{F}}(0) &= P_{\sigma\mathrm{F}} + \frac{1}{j}\frac{\mu_{s\mathrm{F}}(0)}{R_\mathrm{F}}, \end{aligned} \tag{2.17}$$

where the effective spin resistances have been introduced as

$$\begin{aligned} R_{\mathrm{N}} &= \frac{L_{s\mathrm{N}}}{\sigma_{\mathrm{N}}} \\ R_{\mathrm{F}} &= \frac{\sigma_{\mathrm{F}}}{4\sigma_{\mathrm{F},\uparrow}\sigma_{\mathrm{F},\downarrow}} L_{s\mathrm{F}}. \end{aligned} \tag{2.18}$$

In a similar way, the current spin polarization at the TB (denoted "c" for contact) can be obtained as

$$P_{j\mathrm{c}} = P_{\Sigma} + \frac{1}{j}\frac{\Delta\mu_s(0)}{R_{\mathrm{c}}}. \tag{2.19}$$

Here, P_{Σ} is the conductance spin polarization of the contact and $R_{\mathrm{c}} = \Sigma/4\Sigma_{\uparrow}\Sigma_{\downarrow}$ is the effective spin resistance of the contact. While the spin current through the interface is continuous, the spin accumulation is not. The drop in quasi-chemical potential through the TB follows from equation 2.19 as

$$\Delta\mu_s = jR_{\mathrm{c}}(P_j - P_{\Sigma}). \tag{2.20}$$

Figure 2.3 shows the spin current and spin accumulation for the case of spin injection, i.e., electrons flowing from the FM into the NM ($j < 0$). Both the spin current as well as the spin accumulation decay exponentially away from the contact region with their characteristic spin diffusion length. For $j > 0$, one speaks of spin extraction.

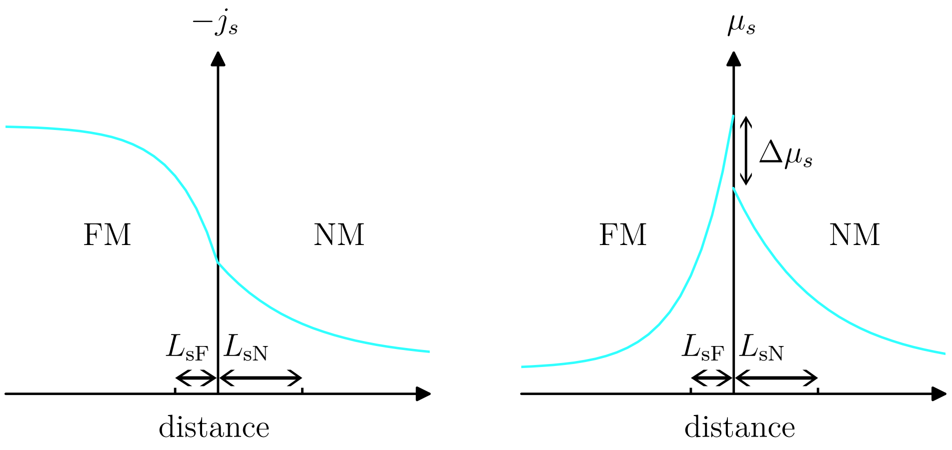

Figure 2.3: Upon spin injection from a FM into a NM, the spin current over the junction is continuous (left side). The profile of the spin accumulation μ_s is discontinuous at the FM-NM junction (right side). μ_s decays exponentially away from the injection point with the spin diffusion length $L_{s\mathrm{N}}$ and $L_{s\mathrm{F}}$ for the NM and FM, respectively. Adapted from [48]

The main result of the standard model of spin injection can be derived by equating the results from equations 2.17 and 2.19 to be

$$P_j = P_{j\mathrm{F}}(0) = P_{j\mathrm{N}}(0) = P_{jc}, \tag{2.21}$$

which yields the spin injection efficiency

$$P_j = \frac{R_\mathrm{F} P_{\sigma\mathrm{F}} + R_\mathrm{c} P_\Sigma}{R_\mathrm{F} + R_\mathrm{c} + R_\mathrm{N}}. \tag{2.22}$$

If the resistance of the NM is much greater than the resistance of the FM and no TB is present, then $P_j \to 0$, which describes the conductivity mismatch problem discussed at the end of section 2.1.

The spin-to-charge coupling equation 2.10a states that in a FM, a gradient in the spin accumulation leads to a charge current. The right side of figure 2.3 (where $j < 0$) shows that $\nabla\mu_s > 0$, which implies a current counterpropagating to the applied bias. From a physical point of view, the nonequilibrium spin accumulation diffuses away from the contact into the FM, where spin currents also cause a charge current. As a consequence, an additional resistance, called the *spin bottleneck effect*, [61] emerges, which can be derived by solving equation 2.10a for $\nabla\mu$ and integrating the result for both the FM and the NM regions separately. This gives the total quasichemical potential drop over the FM-TB-NM area. From the presence of a spin accumulation in the FM, a correction δR to the total serial resistance $\tilde{R}_\mathrm{N} + \tilde{R}_\mathrm{F} + 1/\Sigma$ arises as

$$\mu_\mathrm{N}(\infty) - \mu_\mathrm{F}(-\infty) = (\tilde{R}_\mathrm{N} + \tilde{R}_\mathrm{F} + \frac{1}{\Sigma} + \delta R)j. \tag{2.23}$$

The expression for the spin bottleneck effect (also called spin-coupled resistance) can finally be expressed as

$$\delta R = \frac{R_\mathrm{N}(P_\Sigma^2 R_\mathrm{c} + P_{\sigma\mathrm{F}}^2 R_\mathrm{F}) + R_\mathrm{F} R_\mathrm{c}(P_{\sigma\mathrm{F}} + P_\Sigma)^2}{R_\mathrm{F} + R_\mathrm{c} + R_\mathrm{N}}. \tag{2.24}$$

The correction to the serial resistance from the spin bottleneck effect is always positive: $\delta R > 0$

Spin Detection

When injecting spins from a FM into a NM, a voltage is applied and a spin accumulation inside the NM builds up. The inverse effect can be used for spin detection: if a spin accumulation is generated in a NM in proximity to a FM, an electromotive force (emf) appears in an open circuit. This emf can then be measured as a voltage drop, which was proposed in 1980 by Silsbee [62] and experimentally realized in 1985 by Johnson and Silsbee [63].

The spin detection scheme is shown in figure 2.4. A spin accumulation is injected into a NM channel, which then diffuses towards all directions, i.e., towards the right and left side of the injection point in this case. As a consequence, a spin current ($j_s \neq 0$), yet no charge current ($j = 0$), flows to the right side of the channel, where an emf builds up at a second FM-NM interface. This emf can be measured as a non-local voltage drop.

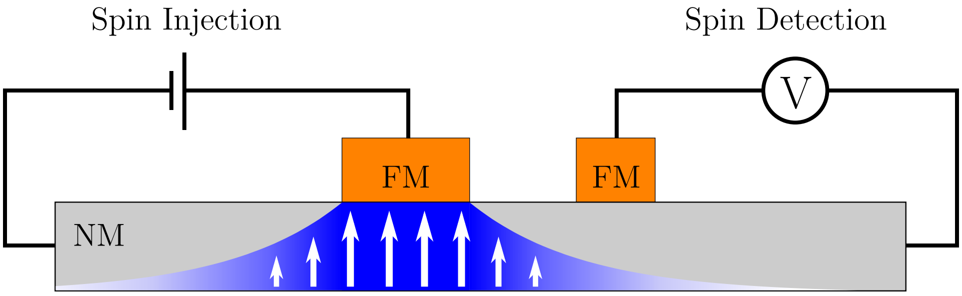

Figure 2.4: Typical non-local spin detection scheme using Silsbee-Johnson spin charge coupling [63]. Spins are injected from the left FM into the NM channel and diffuse towards all directions (blue color gradient). Using a second FM-NM interface, the spin accumulation can be measured as a non-local voltage drop. Adapted from [48]

Considering a FM-NM interface at $x = 0$ and a spin accumulation inside the NM, far away from the interface $\mu_{s\mathrm{N}}(\infty) \neq 0$ and using the charge neutrality condition, the emf can be expressed as

$$\mathrm{emf} = \Delta\mu - P_{\sigma\mathrm{F}}\mu_{s\mathrm{F}}(0). \tag{2.25}$$

Equations 2.10a and 2.10b can also be formulated for the contact region between the FM and the NM. Using $j = 0$, the quasichemical potential drop across the interface reads

$$\Delta\mu = -R_{\mathrm{c}}P_{\Sigma}j_s(0). \tag{2.26}$$

There are two contributions to the emf: the first one is a drop in quasichemical potential aross the contact, which arises from $P_\sigma \neq 0$ - the contact acts a spin filter. The second part is contributed by the spin polarization in the ferromagnet.

Assuming that the spin current j_s is continuous across the interface, the emf can be calculated as

$$\mathrm{emf} = -\frac{R_{\mathrm{F}}P_{\sigma\mathrm{F}} + R_{\mathrm{c}}P_{\Sigma}}{R_{\mathrm{F}} + R_{\mathrm{c}} + R_{\mathrm{N}}}\mu_{s\mathrm{N}}(\infty) = -P_j\mu_{s\mathrm{N}}(\infty). \tag{2.27}$$

By changing either the sign of $\mu_{s\mathrm{N}}(\infty)$ or P_j, i.e., changing the magnetization direction of the injector or the detector, respectively, the emf switches in sign. This way, the spin valve method can be employed, which gives experimental access to measuring a spin accumulation and determining spin transport parameters. The spin valve method is covered in section 5.1.

Chapter 3

Theoretical Background of 2D and 1D transport

3.1 The two-dimensional Electron Gas (2DEG)

When two materials with different bandgaps are brought into contact, an electron transfer occurs at the heterojunction, where electrons can move freely in the plane of the heterojunction and have quantized energy levels in a direction perpendicular to the plane [64]. The alignment of the respective bands is given by Anderson's rule [65].

In the case of a heterojunction between n-doped AlGaAs and undoped GaAs, a *triangular quantum well* emerges, where the potential landscape close to the heterojunction is linear. The solution to the Schrödinger equation is given by the Airy function [66], which has to be calculated numerically [67]. If only the ground state in the quantum well is occupied, one refers to the system as a *two dimensional electron gas* (2DEG).

The conduction band profile and the wave function of the aforementioned hetreostructure is schematically shown in figure 3.1. Electrons from the n-doped AlGaAs diffuse into the GaAs layer, where they get trapped and cannot diffuse back. At the interface a 2DEG emerges. Due to the spatial separation between the 2DEG and the ionized donors, the impact of ionized-impurity scattering is greatly reduced [66]. This method of modulation doping is often used to achieve high mobilities in a 2DEG.

3.1.1 2D Density of States

In a 2DEG, the energy dispersion is parabolic and reads [64]

$$E = E_0 + \frac{\hbar^2 k_{||}^2}{2m^*}, \tag{3.1}$$

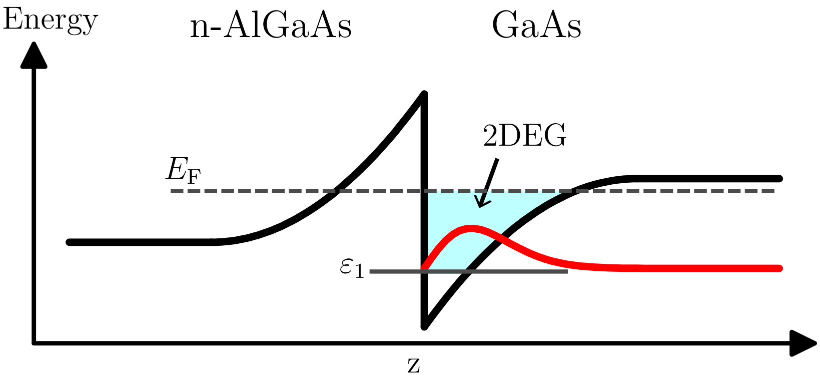

Figure 3.1: Conduction band profile (black) and wave function (red) of a heterojunction between n-AlGaAs and undoped GaAs. Electrons from the AlGaAs diffuse into the GaAs layer, where they get trapped and form a 2DEG. Adapted from [66].

where $k_{||} = \sqrt{k_x^2 + k_y^2}$ is the in-plane wave vector, m^* is the effective mass and $\hbar$ the reduced Planck constant. E_0 is the energy of the first subband.

The perodicity in a crystal of length L demands that the wave vector of an electron can only take certain values [26]. As a consequence, the number of possible states per unit of k-space volume in two dimensions is $Z = L^2/(2\pi)^2$. The number of possible states can also be examined in the energy space. Here, the *density of states* $\mathcal{D}(E)$ refers to the number of states per unit energy and unit area. The total number of states in k-space and energy-space has to be the same, thus

$$\int_{k(E)}^{k(E+\Delta E)} Z(k)d^2k = 2\frac{L^2}{(2\pi)^2}2\pi k\,dk = \mathcal{D}'(E)dE, \tag{3.2}$$

where the factor 2 in the second term comes from the spin degeneracy. From this, the density of states in 2 dimensions

$$\mathcal{D}(E) = 2\frac{2\pi k}{(2\pi)^2}\frac{dk}{dE} = \frac{m^*}{\pi\hbar^2} \tag{3.3}$$

is constant and does not depend on unit energy.

At low temperatues the sheet carrier density then reads

$$n_{2\mathrm{D}} = \int_0^\infty \mathcal{D}(E)f(E)dE = \frac{m^*}{\pi\hbar^2}\cdot E_\mathrm{F}, \tag{3.4}$$

where $f(E)$ is the Fermi-Dirac distribution and E_F the Fermi energy, which separates occupied states from unoccupied states.

The Fermi wave vector k_F and Fermi wavelength λ_F are given by

$$\begin{aligned} k_\mathrm{F} &= \sqrt{\frac{2m^* E_\mathrm{F}}{\hbar^2}} = \sqrt{2\pi n_\mathrm{2D}} \\ \lambda_\mathrm{F} &= \frac{2\pi}{k_\mathrm{F}} = \sqrt{\frac{2\pi}{n_\mathrm{2D}}}. \end{aligned} \tag{3.5}$$

For a 2DEG investigated in this work, $\lambda_\mathrm{F} \approx 40\,\mathrm{nm}$.

3.1.2 Transport Properties of a 2DEG

The diffusive transport properties of a 2DEG can be described by the Drude model [68], where the electron's movement in a conductor is governed by classical mechanics. In an applied electric field E_x electrons are accelerated until after a certain time interval, called the scattering time τ, a scattering event takes place and the electron's motion is changed to a random trajectory. The average drift velocity v_d and the carrier density n_s in the conductor determine the local current density $j(r)$:

$$\vec{j}(r) = \sigma \vec{E} = \frac{n_s e^2 \tau}{m} \vec{E} = -e n_s \vec{v}_\mathrm{D} \tag{3.6}$$

where σ is the conductivity, e and m the electron's charge and mass, respectively. The conductivity and the mobility μ_e are related via the expression $\sigma = n_s e \mu_\mathrm{e}$.

Ballistic and Diffusive Transport

An important lengthscale is the mean free path $l_\mathrm{MFP} = v_\mathrm{F}\tau$, with v_F the Fermi velocity. If the sample extends lengthscales $L > l_\mathrm{MFP}$, diffusive motion occurs in the sample and the Drude model can be applied, while the ballistic regime occurs for for $L < l_\mathrm{MFP}$, where the Drude model is inapplicable. Figure 3.2 shows the difference between diffusive and ballistic transport: in the former, the main contribution to the transport properties is from scattering of electrons at impurities, while for the latter, scattering at the sample boundaries determines the current.

When applying a voltage V to a ballistic channel, the current I through the channel is independent of the channel length L. As a consequence, the *conductance* $G = I/V$ is a global property of a ballistic sample.

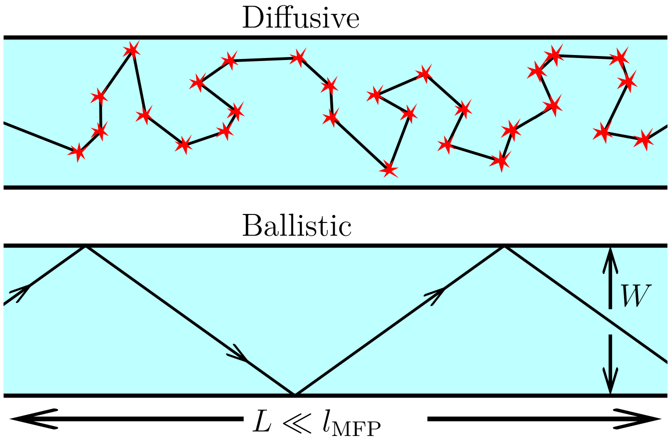

Figure 3.2: Schematic representation of diffusive (top) and ballistic (bottom) electron transport. For diffusive transport, scattering in the channel dominates the trajectory, while in the ballistic regime, only scattering at the sample boundary plays a role. Adapted from [69]

3.2 One-dimensional System: the Quantum Point Contact (QPC)

A quantum point contact (QPC) is a system with clear ballistic transport properties. A QPC is obtained when a 2DEG approaches its one-dimensional limit by a further constriction of the order of the Fermi wavelength. Experimentally, this constriction can be achieved using split-gates.

For a pair of split-gates expanding in y-direction, perpendicular to the movement of electrons in x-direction, a saddle point potential emerges as $V = V_0 - \frac{1}{2}m^*\omega_x^2x^2 + \frac{1}{2}m^*\omega_y^2y^2$. In the saddle point potential only V_0 has a linear relation with the applied gate voltage, whereas the other parameters remain constant [70]. ω_x and ω_y are the curvatures of the potential in x- and y-direction, respectively.

The energy dispersion [68]

$$E_{\mathrm{n}}(k_x) = E_{\mathrm{n}} + \frac{\hbar^2 k_x^2}{2m^*} \tag{3.7}$$

is parabolic, where n is a quantum number representing a *one-dimensional mode* in the channel. A mode is occupied if its energy E_{n} lies below the Fermi energy.

At low temperatues, the total conductance of the channel becomes

$$G = 2\,\frac{e^2}{h} \cdot N, \tag{3.8}$$

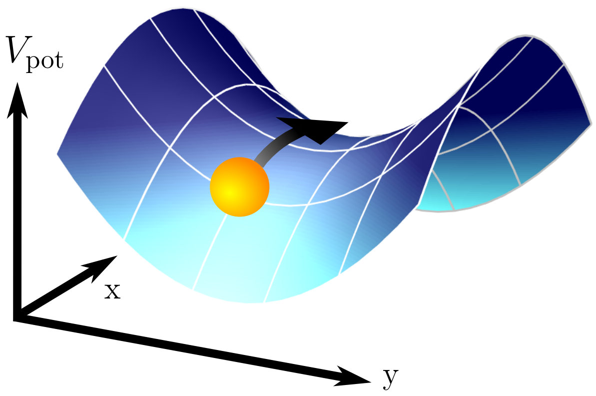

Figure 3.3: Representation of an electron passing through a saddle point potential V, which confines a 2DEG in y-direction to approach its one-dimensional limit. The potential originates from applying a negative gate voltage to a split-gate.

where N is the number of occupied modes, e^2/h is the conductance of a one-dimensional channel and the factor 2 comes from spin degeneracy. As the gate voltage is decreased, modes become depopulated and the conductance decreases as a step function from $G(\mathrm{N}) \rightarrow G(\mathrm{N}-1)$.

Quantized conductance was first observed in 1988 independently by van Wees *et al.* [71] and Wharam *et al.* [72].

Conductance expressed through Transmission: the adiabatic Approximation

In a QPC electrons are forced to ballistically travel through a narrow constriction with lengthscales shorter than the mean free path. As a consequence, the Drude model for conduction cannot be applied. A suitable model is the Landauer approach [73–75] [1] as shown in figure 3.4, where two-dimensional electron reservoirs are connected to a one-dimensional channel. The conductance is then expressed in terms of transmission and backscattering at the transition from the reservoir to the wire. If the change from the two-dimensional to the one-dimensional region happens gradually, one speaks of a adiabatic transition, where intersubband scattering is absent [76].

The adiabatic approximation was investigated by Glazman *et al.* [77] and by Yacoby and Imry [78]. Here, the notation from reference [68] will be used.

---

[1] The Landauer approach considers two-terminal geometries and was extended by Büttiker to describe multi-terminal setups, which is referred to as the *Landauer-Büttiker formalism.*

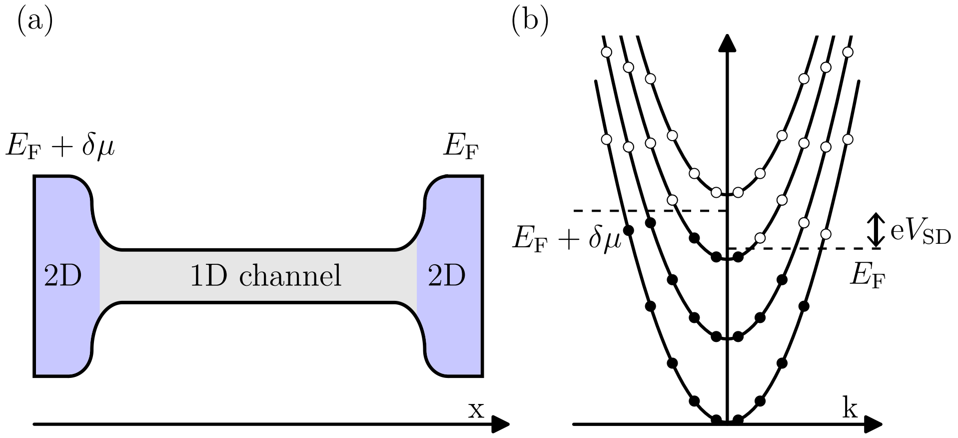

Figure 3.4: (a) In the Landauer approach, a one-dimensional channel is connected to two-dimensional electron reservoirs. If a voltage is applied, the chemical potential of the left reservoir is shifted. (b) Dispersion relation of the one-dimensional channel. For $k < 0$, states are occupied up to $E_F + \delta\mu$ (filled dots) and unoccupied for greater energies (empty dots). For $k > 0$, electron states are filled up to E_F. Adapted from [76].

When the hamiltonian is separated into two parts

$$\begin{aligned} \mathcal{H}_x &= -\frac{\hbar^2}{2m^*}\frac{\partial^2}{\partial x^2} \\ \mathcal{H}_{yz}(x) &= -\frac{\hbar^2}{2m^*}\left(\frac{\partial^2}{\partial y^2}+\frac{\partial^2}{\partial z^2}\right)+V(x,y,z), \end{aligned} \tag{3.9}$$

the solution of the Schrödinger equation for the total hamiltonian $\mathcal{H} = \mathcal{H}_x + \mathcal{H}_{yz}$ can be written as

$$\psi(x,y,z) = \sum_{\mathrm{n}} \xi_{\mathrm{n}}(x)\chi_{\mathrm{n}}(y,z;x), \tag{3.10}$$

where $\chi_{\mathrm{n}}(y,z;x)$ is the solution of the eigenvalue problem for $\mathcal{H}_{yz}$. Projecting ψ on a mode m and using $\partial_x\chi_{\mathrm{n}} \approx 0$ and $\partial_x^2\chi_{\mathrm{n}} \approx 0$ leads to a 1D energy barrier problem:

$$-\frac{\hbar^2}{2m^*}\frac{\partial^2\xi_{\mathrm{m}}(x)}{\partial x^2} + V_{\mathrm{m}}^{\mathrm{eff}}(x)\xi_{\mathrm{m}}(x) = E\xi_{\mathrm{m}}(x), \tag{3.11}$$

where $V_{\mathrm{m}}^{\mathrm{eff}}$ is the effective potential an electron experiences. Using the expression for the quantum mechanical current, the total current through the constriction is

$$I_{\mathrm{tot}} = \frac{2e}{h}\sum_{\mathrm{n}}\int_{-\infty}^{+\infty} dE\ \mathcal{T}_{\mathrm{n}}(E)\left[f_{\mathrm{R}}(E) - f_{\mathrm{L}}(E)\right] \tag{3.12}$$

with $f_{\mathrm{L/R}}$ the Fermi-Dirac distribution at the left/right side of the constriction and $\mathcal{T}_{\mathrm{n}}(E)$ the energy dependent transmission coefficient. For low temperatures and low applied source-drain voltage, the conductance of the QPC becomes

$$G = \frac{2e^2}{h}\sum_{\mathrm{n}}\mathcal{T}_{\mathrm{n}}(E). \tag{3.13}$$

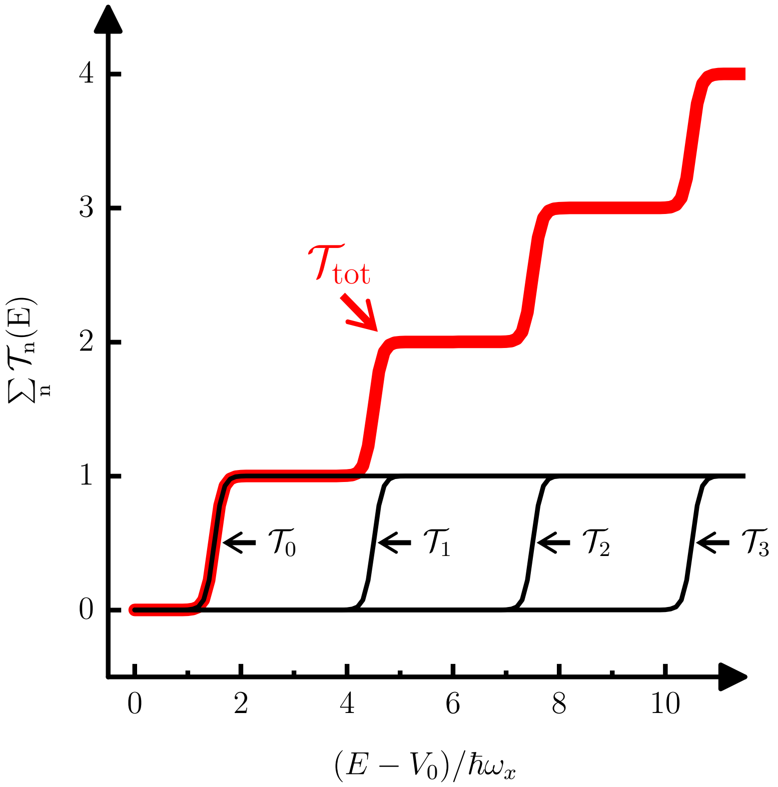

Figure 3.5: Transmission coefficients $\mathcal{T}_{\mathrm{n}}$ vor individual modes n (black) in a QPC for $\omega_y/\omega_x = 3$ and the total transmission coefficient (red). As $(E - V_0)/\hbar\omega_x$ increases, $\mathcal{T}_{\mathrm{tot}}$ increases as a step function. Adapted from [70].

For a saddle point potential (figure 3.3) the transmission coefficient of a given mode takes the form [70]

$$\mathcal{T}_{\mathrm{n}}(\varepsilon_{\mathrm{n}}) = \frac{1}{1+e^{-\pi\varepsilon_{\mathrm{n}}}} \tag{3.14}$$

which depends on the energy

$$\varepsilon_{\mathrm{n}} = 2\frac{E-\hbar\omega_y(\mathrm{n}+1/2)-V_0}{\hbar\omega_x}. \tag{3.15}$$

The total transmission for the first four modes as well as the transmission probabilities for the respective modes are plotted in figure 3.5 for $\omega_y/\omega_x = 3$. When the barrier height of the constriction is decreased, the transmission changes abruptly and the step-like increase of occupied modes typical for QPCs is observed. Experimentally, the transmission through a QPC can be altered by changing the split-gate voltage, which has a linear relation with E.

In this work, a QPC will be used as an energy barrier.

Chapter 4

Methods

4.1 The Spin Esaki Diode

One obstacle for effective spin injection is the conductivity mismatch problem, as described in section 2. In addition, the ferromagnetic semiconductors which can be used in a heterojunction with III-V semiconductors are of p-doping [79, 80]. As a part of a spin Esaki diode [81], a p-doped ferromagnetic semiconductor can be utilized for efficient electron spin injection while avoiding the conductivity mismatch problem.

Part (a) in figure 4.1 represents the bandstructure of a spin Esaki diode under zero bias. Due to the strong doping of both the ferromagnetic p-doped and nonmagnetic n-doped layers of the p-n junction, the Fermi energy E_{F} is shifted to values below the valence band (VB) edge for the p-region and above the conduction band (CB) edge for the n-region, respectively.

For an applied reverse bias as shown in (b) spin polarized carriers tunnel from the VB of the p-region into the CB of the n-region, where a nonequilibrium spin accumulation emerges. This way, a spin Esaki diode can be utilized for efficient spin injection. Under forward bias, as shown in (c), a spin-polarised current flows from the CB of the nonmagnet into the VB of the ferromagnet. This results in a nonequilibrium spin accumulation due to spin extraction, which is of the opposite sign compared to spin injection.

In this work, the spin Esaki diode is formed between GaAs and (Ga,Mn)As [36, 37], which is a diluted magnetic semiconductor (DMS) [23]. A DMS combines the attributes of both a semiconductor (such as bandstructure engineering via doping) and a ferromagnet [24]. In the case of (Ga,Mn)As, Mn ions replacing the Ga cations introduce holes with a magnetic moment [23], i.e., the ferromagnetism is mediated by charge carriers [82]. The magnetic properties of (Ga,Mn)As can be tuned by various parameters such as Mn concentration [83], illumination [84], electric fields (i.e., gating) [85] or doping [86, 87].

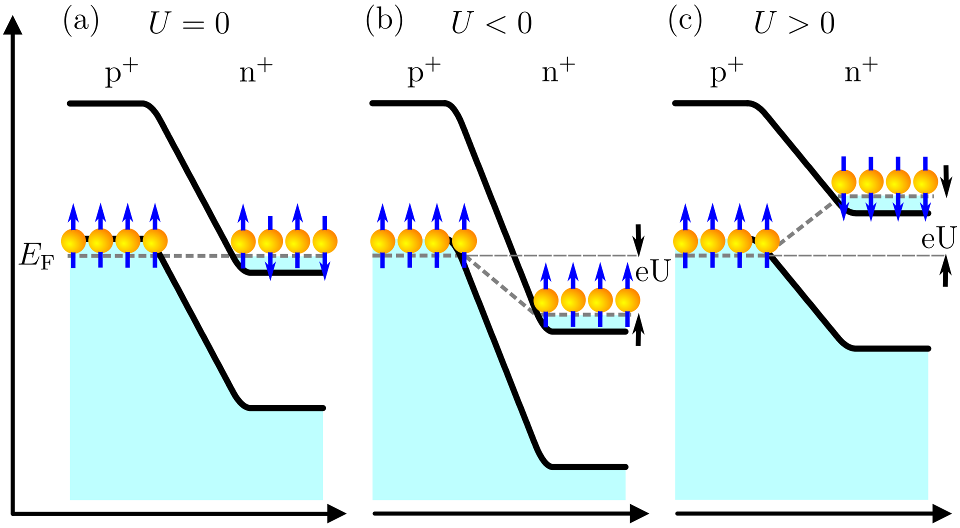

Figure 4.1: Schematic representation of a spin Esaki diode, which is a p-n junction with both the p- and n-region heavily doped so that the Fermi energy E_F lies in the valence band (p-region) and in the conduction band (n-region), respectively. The carriers in the valence band of the p-material are spin polarized. (a) Bandstructure for zero applied voltage. The carriers in the n-side have no spin polarization. (b) Under reverse bias, spin-polarized carriers are injected from the valence band of the p-region into the conduction band of the n-region. (c) Under forward bias, spin-up electrons from the conduction band of the n-region tunnel into the valence band of the p-region. The remaining carriers in the n-region are spin-down polarized and one speaks of spin extraction. The bandstructure of the Esaki diode without (spin-polarized) electrons is adapted from [26].

The devices in this work require two magnets with the same well-defined, strong magnetic anisotropy axis, but different coercive fields. In a DMS, shape anisotropy is weak due to its low magnetization values. As a consequence, magnetocrystalline anisotropy determines the orientation of the easy axis [88], which depends on various parameters such as temperature [89], carrier density [80] and strain [90, 91]. For a Mn content of $3-6\,\%$, temperatures below 4.2 K and compressive strain (as is the case for (Ga,Mn)As grown on GaAs) the easy axis align with the [100] and [010] crystal directions [92, 93]. In addition, the anisotropy can also be defined lithographically by patterning the (Ga,Mn)As into narrow stripes [88, 94–97] to align the easy axis with the orientation of the stripe. Controlling the anisotropy by lithographic means was used for the samples fabricated in this work and will be described in section 4.3.

While (Ga,Mn)As was already used in 1999 to inject spin polarized holes into an (In,Ga)As quantum well [98], a spin Esaki diode was realized in 2001 by Kohda *et al.* [99] and in 2002 by Johnston-Halperin *et al.* [100].

4.2 Wafer Structure

In this work, fabricating a device suitable for efficient all-electrical spin injection is centered around a spin Esaki diode, as described in the previous chapter. For all-electrical spin detection additional requirements have to be met. A spin polarized current must be able to flow from the point of injection into a transport channel from where efficient spin transport towards a detection scheme is possible.

All of the aforementioned criteria are fulfilled by the wafer structure as shown in figure 4.2. The wafers were grown via molecular beam epitaxy (MBE) at the chair of Prof. Dr. Bougeard at the university of Regensburg.

Using (001) GaAs as a substrate, a 1000 nm GaAs/(Al,Ga)As superlattice is grown, which consists of $\sim$ 100 GaAs and (Al,Ga)As layers each. The superlattice reduces crystal strain and screens the effects of disorder, impurities and other electric modulations at the tranport channel (an inverted 2DEG), thus increasing its mobility. Next, 75 nm of $Al_{0.33}Ga_{0.67}As$ is followed by a

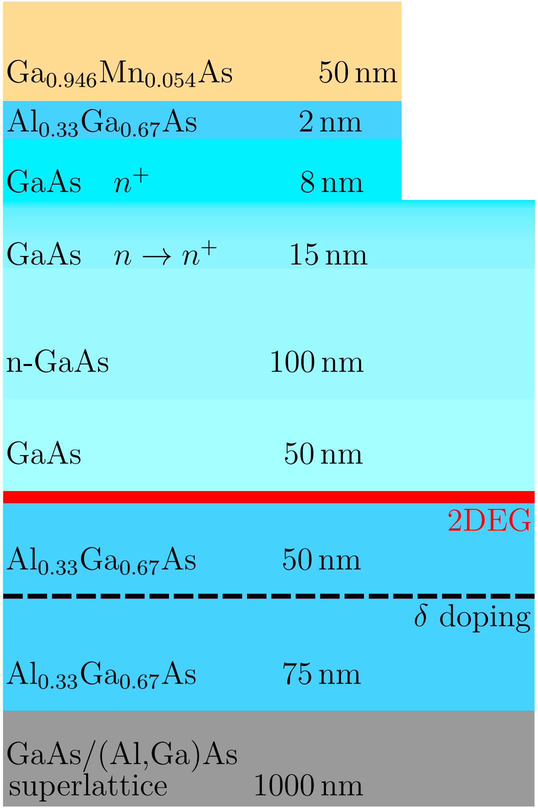

Figure 4.2: Schematic representation of the wafer used for top-down sample fabrication. The wafer, from top to bottom, consists of a GaMnAs - n^+-GaAs heterostructure, which forms a spin Esaki diode as the basis for efficient spin injection. Between the spin Esaki diode and the 2DEG, which emerges in a triangular quantum well formed between GaAs and AlGaAs, the dopant concentration in GaAs is gradually reduced. The AlGaAs, which is modulation doped 50 nm away from the 2DEG, is grown on a GaAs/(Al,Ga)As superlattice.

delta-doping layer with Si as the dopant atoms, with a 50 nm $Al_{0.33}Ga_{0.67}As$ buffer layer on top. While contributing low impurity scattering [101, 102], the delta-doping provides charge carriers for the inverted 2DEG, which forms in a triangular quantum well between the $Al_{0.33}Ga_{0.67}As$ and a 50 nm GaAs layer, thus preserving high mobilities in the 2DEG. Subsequently, 100 nm of lightly doped GaAs with a doping density of $n = 5.7 \cdot 10^{16}\,\mathrm{cm}^{-3}$ is followed by a 15 nm GaAs transition layer, where the doping density is gradually increased ($n \to n^+$) to align with the doping density of the final GaAs layer, which is 8 nm thick with $n^+ = 5 \cdot 10^{18}\,\mathrm{cm}^{-3}$. The wafer is finalized with 50 nm of $Ga_{0.946}Mn_{0.054}As$ which forms a spin Esaki diode with the n^+ GaAs layer. To prevent diffusion of Mn into the wafer, a thin layer (2 nm) of $Al_{0.33}Ga_{0.67}As$ is grown in between the GaAs and the GaMnAs.

The wafer as presented here has a high charge carrier density at the 2DEG and a nonzero charge carrier density between the 2DEG and the spin Esaki diode. This way, carriers injected from the Esaki diode can reach the transport layer. Between the points of spin injection and spin detection, however, spin transport should take place exclusively in the 2DEG, which is achieved by removing the top layers of the heterostructure via etching, where etching within the precise range of $d_{\mathrm{etch}} \sim 55 - 60\,\mathrm{nm}$ is important. This way, other conducting layers away from the 2DEG are removed, while conduction within the 2DEG is still possible. More information on the bandstructure and distribution of carrier density in the wafer is given elsewhere [103].

After cooling the sample down to cryogenic temperatues, the charge carrier density n_{s} of the sample is low. By illuminating the sample with a red LED, n_{s} can be increased due to the *persistent photoeffect*, where electrons occupying DX centers in the Si atoms of the delta-doping layer are optically excited into the 2DEG [104–106].

Experimentally, the quality of a 2DEG can be determined by utilizing magnetotransport measurements. From the slope of Hall measurements (black) and the zero-field magnetoresistance (red) shown in figure 4.3, the carrier density n_{s} and electron mobility μ_{e} were determined to be $n_{\mathrm{s}} = 3.5 \cdot 10^{11}\,\mathrm{cm}^{-2}$ and $\mu_{\mathrm{e}} = 5.9 \cdot 10^{5}\,\mathrm{cm}^2/\mathrm{Vs}$, respectively.

Additionally, the longitudinal resistance ρ_{xx} gives information if the charge carrier transport occurs exclusively in the 2DEG, as intended. If either the etching depth d_{etch} is too low or if the sample was illuminated for too long, a transport channel parallel to the 2DEG is present. In the former case, the parallel channel is in the n-GaAs layer, whereas it emerges in the delta-doping layer in the latter case. A parallel transport channel manifests itself as a component in the longitudinal resistance $\rho_{\mathrm{xx}} \propto B^2$ which is parabolic in the applied magnetic field B [66, 107]. In addition, the Shubnikov-de Haas

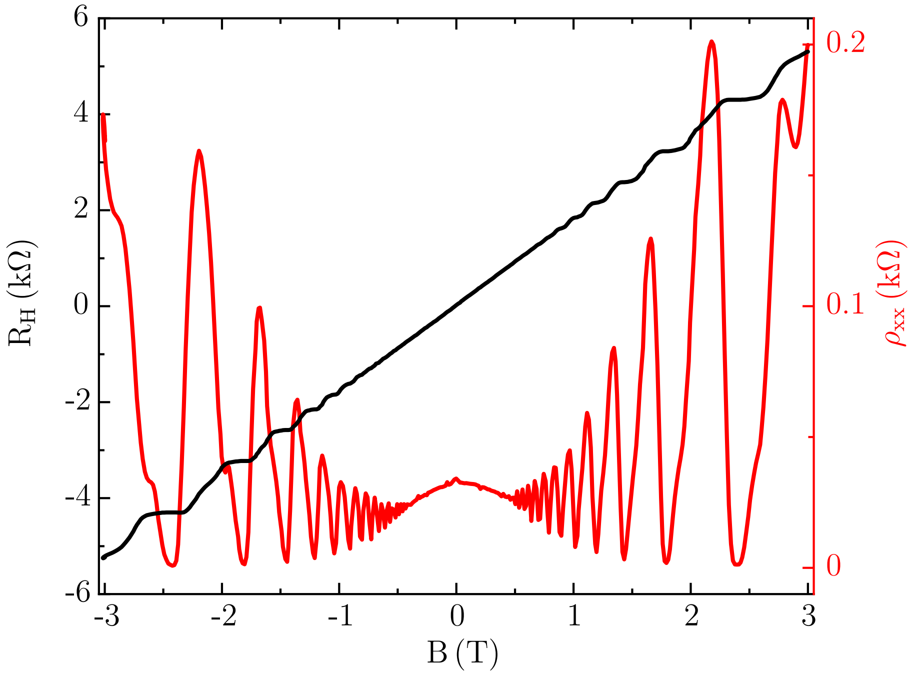

Figure 4.3: Traces of Hall (black, R_H) and magnetoresistance (red, ρ_{xx}) measurements. From R_H, the sheet carrier density n_s can be determined, while ρ_{xx} gives information about the electron mobility μ_e.

oscillations do not reach $\rho_{xx} = 0$ at large magnetic fields.

4.3 Sample Design and Fabrication

In this section, the basic device design well as sample fabrication are described. Unless stated otherwise, all devices in this work were fabricated from the same wafer with a layer structure as described in the previous chapter.

Sample Design

A sketch of a sample is shown schematically in figure 4.4 (a). It consists of a transport channel (also called mesa), which is indicated by the light cyan color. The mesa is connected to reference contacts (dark cyan) as well as contacts for spin injection/detection (yellow), split-gate electrodes (orange) and leads which enable magnetotransport measurements as well as probing the voltage drop in the mesa across the area of the split-gates. Figure 4.4 (b) schematically shows the cross section of a sample with regions including a spin contact, a transport section and a split-gate electrode. In the transport region and for the split gates, parts of the wafer were etched away with an etching depth $d_{\mathrm{etch}} = 55 - 60\,\mathrm{nm}$ to ensure that carrier transport is exclusive to the 2DEG (red). The split gate electrodes were deposited on top of an aluminum oxide (AlOx) layer. For the split-gate, the spin and reference contacts, Au was used as contact material.

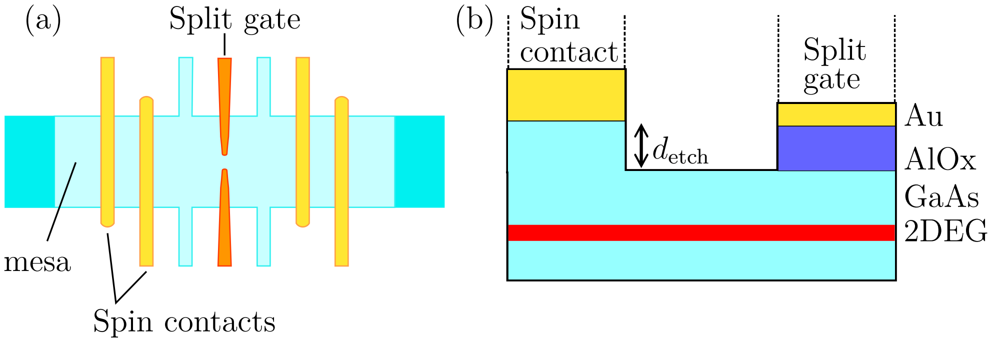

Figure 4.4: (a) Sketch of the sample design used in this work. It consists of a mesa (light cyan), reference contacts (dark cyan), spin injection/detection contacts (yellow) as well as split-gate electrodes (orange). (b) Representation of the cross section of a device. Away from the spin contacts, parts of the heterostructure were etched away. The split-gate electrodes were deposited on an AlOx layer.

In this work, all devices have a mesa width of 20 µm. While usually individual spin contacts are of various widths ($\sim 300 - 700\,\mathrm{nm}$) to ensure different coercive fields, which enables the usage of the spin valve method (see section 5.1), some devices were made with all spin contacts having the same geometry. The distance between individual spin contacts is usually of the order of the spin diffusion length or smaller. The spatial separation between the leads for measuring the voltage drop across the area with split-gate electrodes was kept as small as possible, typically $\sim 6\,\mu\mathrm{m}$. Detailed information on the shape of the split-gates is given in section 5.2.1.

It has to be noted that the reference contacts are of the same structure as the spin contacts, i.e., they also consist of spin-Esaki diodes. However, if the reference contacts are sufficiently far away from a spin accumulation, no emf builds up across the contacts, as the spins dephase on length scales much greater than the spin diffusion length [108]. With a typical distance of 300 µm between the referece contacts and the spin injection contacts, spin detection experiments are feasible.

Sample Fabrication

Sample fabrication was done in the cleanroom at the university of Regensburg using a top-down approach, where standard semiconductor processing techniques were used. In the following, the steps for fabricating a device will be described, whereas detailed information on the physics and optimization of fabrication steps is given in reference [109].

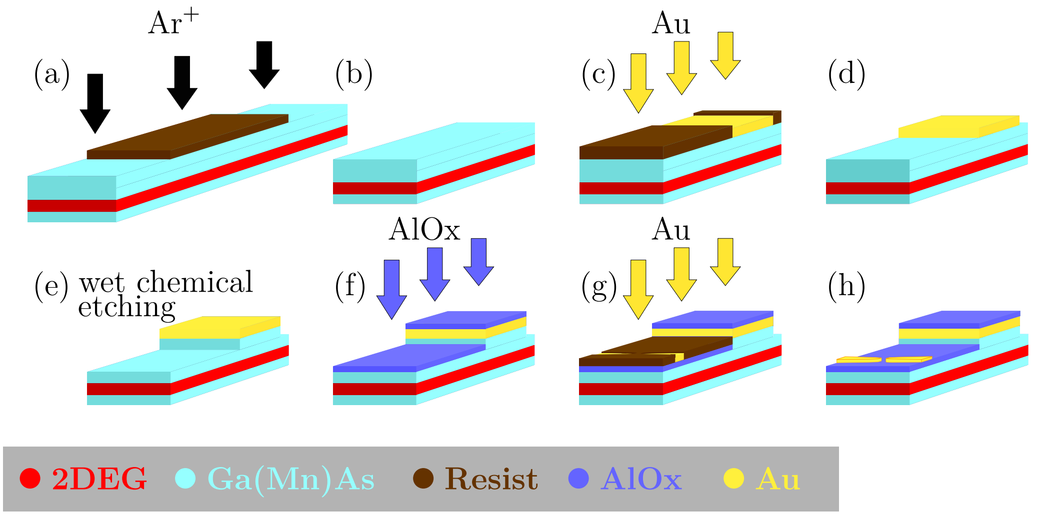

Figure 4.5: Illustration of the various steps during device fabrication. (a) Mesa definition by physical etching. (b) Mesa after removing resist residuals. (c) After development of a positive resist, Au is evaporated on the sample. (d) After lift-off, only the Au which adhered to the sample remains. (e) Wet chemical etching of the sample. The Au acts as an etching mask. (f) Deposition of AlOx. (g) Evaporating split-gate electrodes on the sample. (h) Schematic sketch of the final sample.

The whole sequence of sample fabrication is shown in figure 4.5. In the first step (a), a wafer piece, which is typically 5.5 mm × 5.5 mm large, is coated with a negative e-beam resist (AR-N7500.18). After illumination and development, chemically assisted ion beam etching (CAIBE) with argon is used to define the basic device structure. By removing all conducting layers from the heterostructure, charge transport is now limited to the mesa (b). The precise etching depth $d_{\mathrm{CAIBE}} > 270\,\mathrm{nm}$ is not important. In addition to acetone, an O_2 plasma can be used to carefully eliminate any residual resist from the sample.

In the next electron beam lithography (EBL) step, the positive resist PMMA is used to pattern the spin contacts and reference pads (c). In oder to connect the spin contacts with the substrate, the thickness of the evaporated

Ti/Au must exceed d_{CAIBE}. Directly before evaporating the Ti/Au layers, the sample's native oxide layer is removed by putting it into a HCl:H_2O solution[1]. As the thickness of Ti/Au is large (35/400 nm, respectively, was used), 3 layers of PMMA were spin coated on the sample. This enables a clean lift-off (d). It has to be noted, that during evaporation, Ti and Au adhere to both the sample and to the photoresist. During lift-off, any metal on the resist is washed away. For simplicity, the Ti/Au on the resist is not shown in figure 4.5.

Away from the spin and reference contacts, charge carrier transport exclusive to the 2DEG is desired (see section 4.2). Utilizing wet chemical etching with acetic acid ($10C_2H_4O_2$:$1H_2O_2$:$10O_2$) parts of the heterostructure are removed (e). In this step, the previously evaporated Au acts as an etching mask. The precise etching depth of $d_{\mathrm{etch}} = 55 - 60$ nm has to be reached. If the etching depth is too low, then a parallel transport channel in the mesa exists, which is visible in ρ_{xx} in magnetotransport measurements. If the sample is etched for too long, then all conducting layers in the mesa are removed. For the latter case it has to mentioned, that the sample is still conducting at room temperature and that the missing transport channel only becomes apparent at cryogenic temperatures, where the sample then is no longer conducting. In order to remove the amount of material as demanded, the process of etching can be devided into multiple steps until $d_{\mathrm{etch}} = 55 - 60$ nm is reached. The etching rate depends on multiple factors such as the used acid, temperature of the etching solution or passed time after the solution was mixed [109]. However, if all parameters are kept the same, etching rates and results are reproducible and the etching can be done in one step. Atomic force microscopy (AFM) was used to observe the etched depth.

Using atomic layer deposition (ALD), 50 nm AlOx (Al_2O_3) was grown (f) as an insulator for the gate electrodes at a temperature of 150 °C. Before mounting the sample in the ALD chamber, the sample was again immersed in an HCl:H_2O solution after which a 10 nm SiO_2 seed layer was grown using plama enhanced chemical vapor deposition (PECVD).

In the final steps, the split-gate electrodes are defined using PMMA as photoresist (g). Here, immersing the sample in HCl:H_2O before evaporation of Ti/Au was omitted. The split-gate electrodes must be thin enough to allow transmission of light. The metal thicknesses of 2/20 nm for Ti and Au, respectively, are not enough to electrically contact the gate to the substate. Consequently, the contacts for the gate were defined in a separate EBL

---

[1] After the dip in HCl:H_2O, it is important to rinse the sample with H_2O, otherwise the Ti/Au does not adhere well. This was one of the many things that were learned the hard way.

step, where again 35/400 nm of Ti/Au were evaporated, connecting the gate electrodes at the edge of the mesa with the substrate. A scanning electron microscope (SEM) image of the contact between a split-gate electrode and the substrate is shown in figure 4.6 (c). The final sample is schematically depicted in figure 4.5 (h).

Utilizing standard wire bonding, the sample is electrically connected to a chip carrier. While any large contact pads (~ 150 µm × 150 µm) on the mesa can be bonded directly, the spin contacts and split-gates were connected through larger contact pads on the substrate.

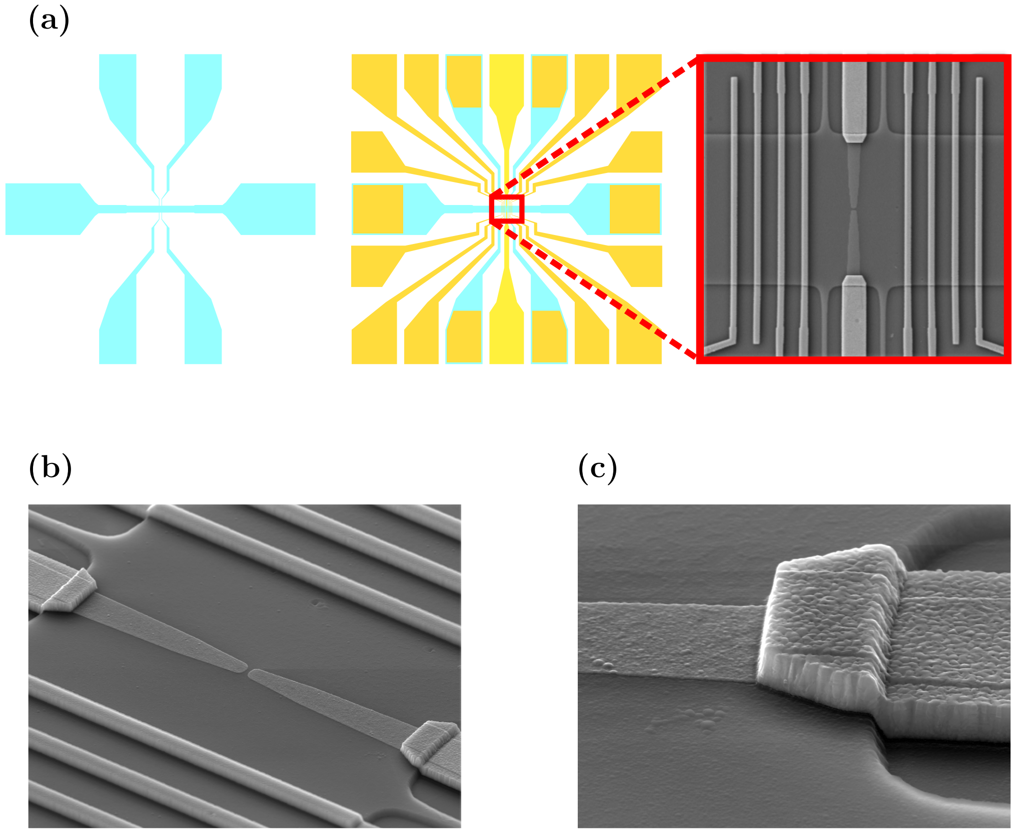

Figure 4.6: (a) Drawing of the mesa layout (left) and the final sample (right). The inset shows a scanning electron microscope (SEM) picture of the device. (b) SEM picture of a pair of split-gate electrodes. (c) SEM image of the contact between a split-gate electrode and the substrate.

The layout of the mesa is shown on the left side of figure 4.6 (a), while the drawing in the middle represents the final sample. As the Au of the spin contacts and reference pads is covered in AlOx, it appears darker than the metal of the split-gate and its contacts. The inset shows a SEM picture of the area around the split-gates. It consists of four spin contacts to the left and to the right of the split-gates each, leads for measuring a potential drop and a pair of split-gate electrodes in the middle. Figure 4.6 (b) shows a SEM image of a pair of split-gates from a close distance.

Sample fabrication was one of the main challenges in this work, partly due to the sheer number of process steps needed and the necessity for accurate alignment. More detailed information on the challenges of obtaining a finished device is given elsewhere [110].

4.4 Measurement Setup

To utilize the magnetic properties of a material, it must be maintained at a temperature below its Curie temperature. In this work, the heterostructure of the utilized wafer includes (Ga,Mn)As, a ferromagnetic semiconductor, which has a Curie temperature $\sim 60\,\mathrm{K}$. Unless otherwise specified, measurements were done in a cryostat at temperatures of 1.4 K, which is significantly below the Curie temperature.

By employing superconducting coils, which are immersed in liquid helium, external magnetic fields up to $\pm 14\,\mathrm{T}$ can be applied. Furthermore, the sample

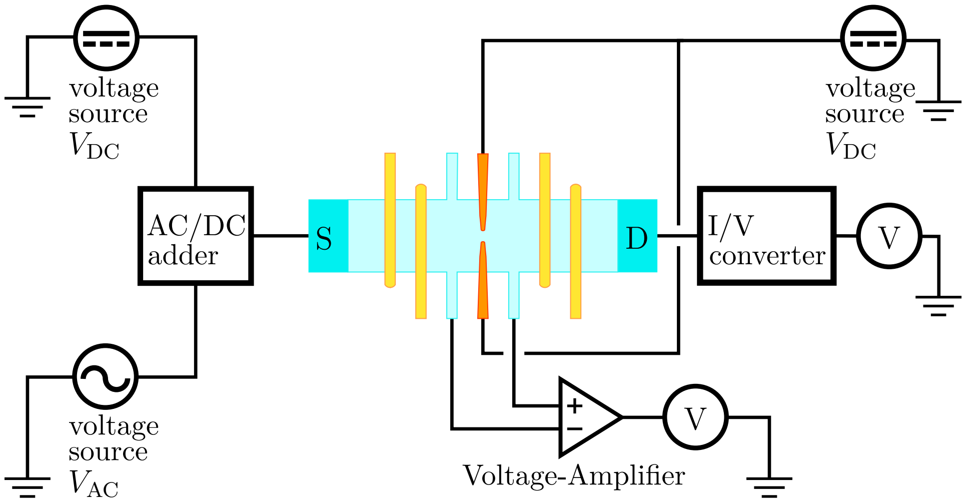

Figure 4.7: Measurement setup which enables the observation of quantized conductance. At the source of the mesa (denoted S), an AC/DC adder is used to superimpose an applied alternating voltage with a constant voltage. At the drain of the mesa (denoted D), an I/V converter is connected to a multimeter to detect the current flow through the mesa. During measurement, the applied voltage to the split-gates (orange) is swept by a DC voltage source. The longitudinal voltage drop in the mesa across the region adjacent to the split-gates is connected to a voltage amplifier and read out by a multimeter. When measuring quantized conductance, no device is connected to any spin-contacts (yellow).

can be rotated within the cryostat, allowing for a transition between an in-plane and out-of-plane orientation of the applied magnetic field.

In general, standard lock-in measurement techniques were used and measurements were done at an excitation frequency of 19 Hz unless stated otherwise. The setup to measure quantized conductance and characterize a QPC is shown in figure 4.7. Between the source and drain of the mesa, an AC voltage V_{AC} is supperimposed with a DC voltage V_{DC} using an AC/DC adding device, which was developed at the chair of Prof. Dr. Bougeard [111]. At the drain, an I/V converter is connected to a multimeter which allows to measure the current flow through the device. A second DC voltage source is used to apply and sweep the voltage at the split-gates of the QPC. By utilizing a voltage amplifier, which is connected to a multimeter, the four-terminal voltage drop across the area of the split-gates can be measured.

Chapter 5

Experimental Results: Spin Valve and Quantized Conductance

The scope of this work is to use a QPC to detect a spin accumulation. Therefore, two conditions must be met. First, a spin accumulation must be injected and travel to a point of detection. The second condition is that quantized conductance must be achieved.

5.1 Spin Valve

To detect a spin accumulation in a material by all-electrical means, the spin valve method can be employed. Here, two different geometries are available. One possibility is to utilize a local, two-terminal setup, where a fixed current is applied between two ferromagnetic (FM) electrodes, which are separated by a nonmagnetic (NM) transport channel. If sweeping an external magnetic field and measuring the voltage drop between the pair of ferromagnets gives rise to a spin valve pattern, a spin accumulation is present. In this type of measurement setup, however, measurement components unrelated to spin transport can influence the obtained signal. An additional voltage drop may be caused by contact resistances and other effects [112], such as anisotropic magnetoresistance [113].

These challenges can be avoided by utilizing a non-local measurement configuration. In this four-terminal setup, as shown in figure 5.1, a bias is applied between a FM and a reference contact, i.e., spins are injected, while a voltage drop V_{NL} is measured between a second FM-reference contact pair. It is important to note that a spin current, but no charge current flows between the ferromagnetic contacts. This spin current arises due to spin diffusion from

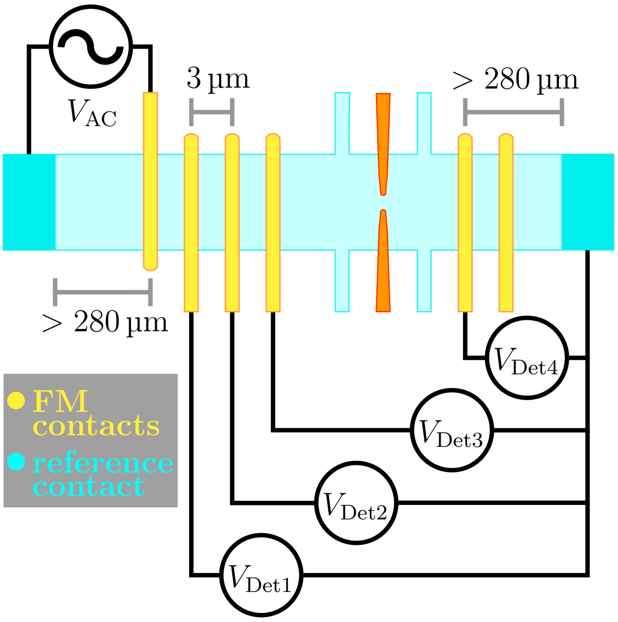

Figure 5.1: Non-local spin valve measurement setup. Spins are injected into the left side of the mesa by applying a current between a given FM contact and a reference contact. The spin accumulation then diffuses in all directions. At any point in the channel, the spin accumulation can be detected by measuring a non-local voltage drop between a corresponding FM contact and a second reference contact. Between the various FMs no charge curernt flows.

the point of spin injection towards the second FM, where the aforementioned non-local voltage drop can be measured due to Silsbee-Johnson spin charge coupling [63].

Since the spin transport is based on diffusion and spin detection is facilitated by tunnel contacts, the spin accumulation μ_s in the NM transport channel follows an exponential decay away from the injection contact (see chapter 2) with

$$\mu_s(x) = \mu_s(0)e^{-x/L_s}, \tag{5.1}$$

where $\mu_s(0)$ is the initial spin accumulation and L_s the spin diffusion length. To measure a voltage drop due to Silsbee-Johnson spin charge coupling an electromotive force (emf) needs to be present in the detecting FM, yet absent in the reference contact. As a consequence, the distance between the injector and detector must be in the order of L_s, while the reference contacts must be sufficiently distant from the initial spin accumulation. As shown in figure 5.1, multiple detection contacts can be used in a single measurement.

To obtain the spin valve pattern, i.e., the characteristic switching in V_{NL}, two magnetic electrodes with the same well-defined magnetic anisotropy axis but different coercive fields are utilized. This allows to switch the magnetizations of the FMs between mutual parallel and antiparallel configurations by sweeping an external magnetic field along this anisotropy axis. Figure 5.2 illustrates the landscape of the quasichemical potential μ (black), spin accumulation μ_s (dashed grey) and the quasichemical potentials for the individual spin species $\mu_{\uparrow,\downarrow}$ (red) in a non-local spin valve measurement at various mag-

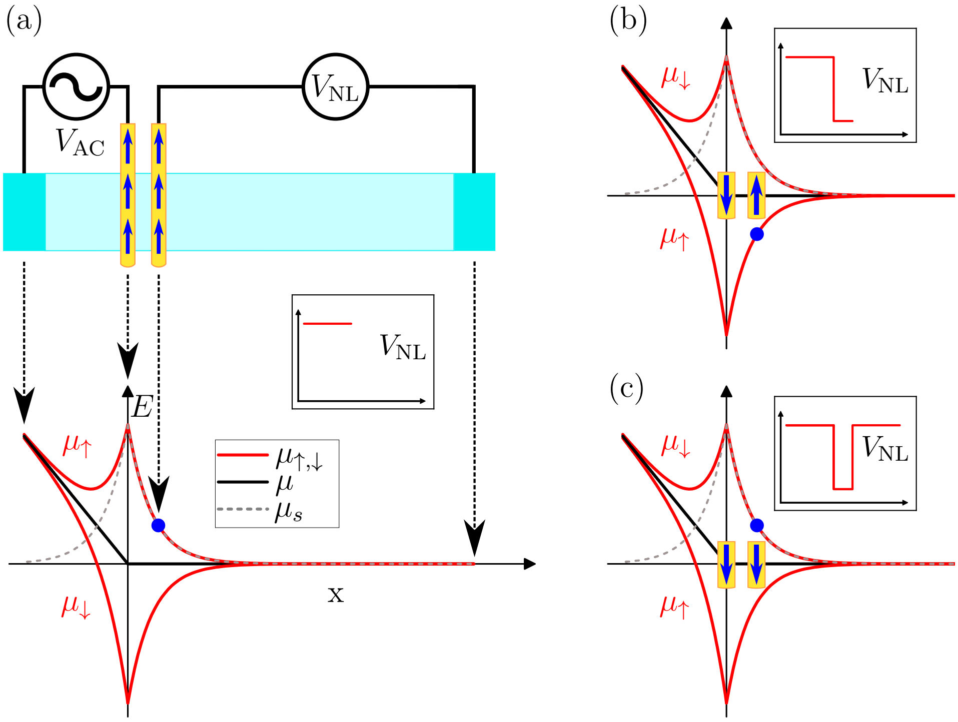

Figure 5.2: Potential landscape of the quasichemical potential μ (black), spin accumulation μ_s (dashed grey) and the quasichemical potentials for the individual spin species $\mu_{\uparrow,\downarrow}$ (red) for non-local spin injection at various magnetic field strengths. Between the leads of the left side of the sample a current is applied, resulting in a spin accumulation. The exponential decay of the spin accumulation indicates its diffusion into all directions. The magnetization configuration switches from parallel (a) to antipallel (b) and then restores a parallel configuration (c). In a second FM used for spin detection an emf develops (blue dot) due to the spin accumulation, which can be measured as a non-local voltage drop V_{NL}. V_{NL} plotted vs. B is shown in the insets and displays the slope typical for spin valve measurements. Adapted from [28]

netic field strengths. Between the left reference contact and the left FM, μ displays a linear slope due to an applied bias. This is in contrast to the rest of the sample, where $\mu = 0$. The spin accumulation μ_s, which is injected at $x = 0$, decays exponentially into all directions. An emf develops in the FM used for spin detection, as indicated by the blue dot. Since both FMs are in the parallel configuration (a), the emf, and hence the measured signal V_{NL}, are positive. The schematic plot of V_{NL} vs. magnetic field B is shown in the insets of the figure. When the magnetization of the injecting contact switches (b), leading to an antiparallel configuration, the sign of μ_s changes. Consequently, V_{NL} switches sign. A parallel configuration is restored once the detecting FM also switches its magnetization orientation (c). From a mathematical point of view, this corresponds to a change in sign of P_j in equation 2.27, which results in a positive V_{NL}. This way, the standard spin valve signals are obtained.

The non-local spin valve measurements presented in figure 5.3, which exhibit the expected switching in V_{NL}, were obtained from devices which were fabricated using the wafer layout described in chapter 4. During measurement, an external magnetic field $\mathrm{B}_y = \mathrm{B}$ was swept, where $y||[1\bar{1}0]$ is parallel to the spin contacts, while a bias of $I_{\mathrm{AC}} = 2\,\mu\mathrm{A}$ was applied. The non-local voltage drop is displayed for various distances between the spin injection electrode and the detection contact, with curves shown for disances of 3, 6, 9 and 19 µm, respectively. The clear spin valve pattern demonstrates the presence of a spin accumulation in our devices up to large spatial separations between the injector-detector pair. In addition, the clear switching of all the traces in the figure has further implications. The abruptness of the spin valve also suggests that the FMs are uniformly magnetized in a single magnetic domain. This is in contrast to magnets with multiple domains, where the injected spin accumulation may be cancelled out in part. This shows that using lithographic means to pattern narrow stripes, which defines a magnetic easy axis through induced strain realaxation, is an approrIate approach for

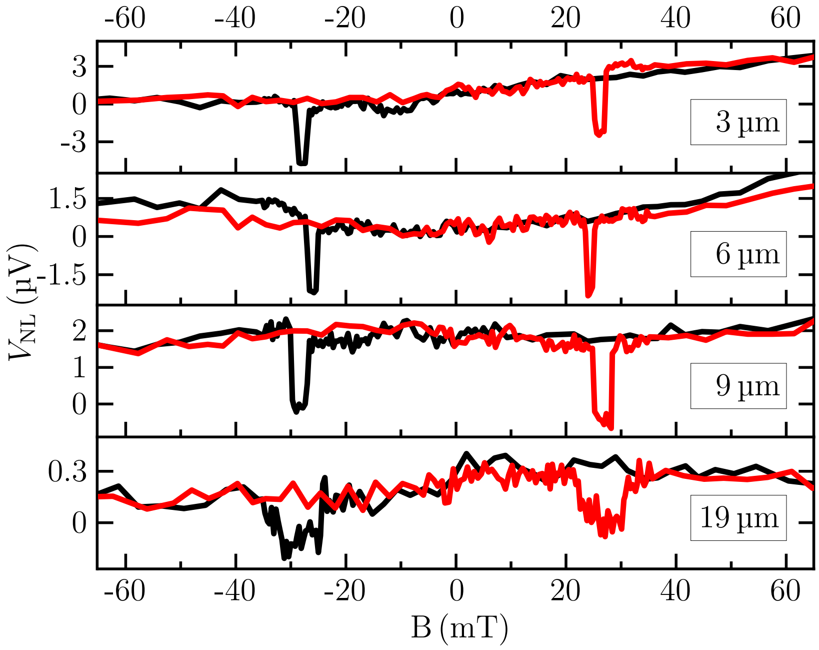

Figure 5.3: Non-local spin valve measurements for various distances with an injection current of $I_{\mathrm{AC}} = 2\,\mu\mathrm{A}$. The presence of a spin accumulation in our device is confirmed by the clear switching in V_{NL}.

the devices used in this work. It has to be noted that the measured data of V_{NL} around the switching event is shifted by a finite voltage offset. Origins of a finite baseline include Peltier and Seebeck effects [114], a nonuniform tunnel barrier thickness or pinholes in the tunnel barrier [115]. In this work, pinholes are not considered relevant. Effects like interface spin scattering are relevant at elevated temperatues [116].

As mentioned before, various conditions must be met to enable an all-electrical spin injection/detection scheme. The traces shown in figure 5.3 demonstrate that the aforementioned criteria are met and that a GaMnAs spin Esaki diode and an inverted GaAs/GaAlAs 2DEG are suitable for spin injection and for spin transport, respectively.

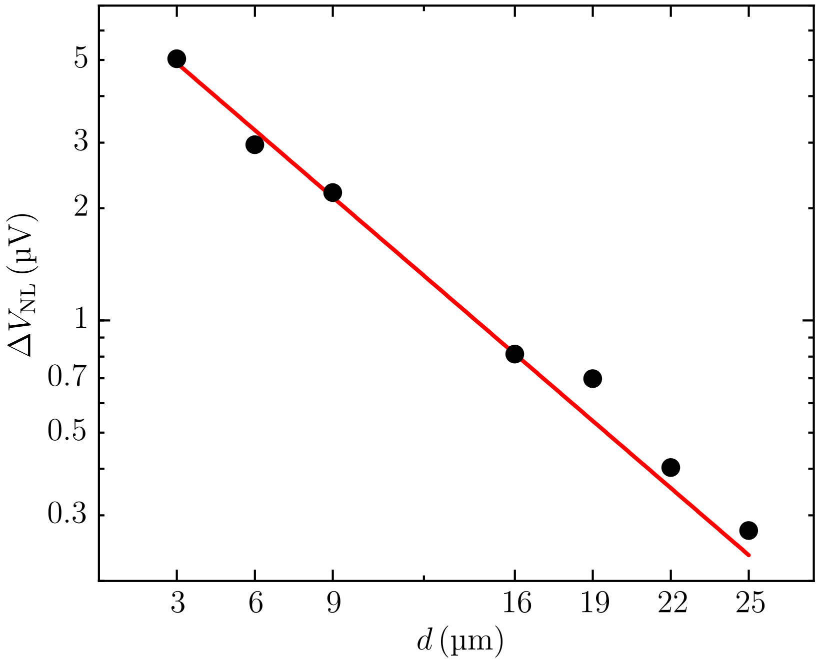

Figure 5.4: Semi-logarithmic plot of the amplitude of a spin valve signal ΔV_{NL} over injector-detector distance d. From a linear fit, the spin injection efficiency $P = 56\,\%$ and spin diffusion length $L_s = 7.2\,\mu\mathrm{m}$ can be extracted. The data was obtained from spin valve signals with a current $I_{\mathrm{AC}} = 2\,\mu\mathrm{A}$.

The data shown in figure 5.3 contains more information on the spin accumulation. More precisely, it is the distance-resolved amplitude of the spin valve signal ΔV_{NL} that enables additional insight. Since spin transport is mediated by diffusion, ΔV_{NL} is expected to decay exponentially with a distance

d between the spin injection and spin detection contacts [38]:

$$\Delta V_{\mathrm{NL}} = \frac{P^2 I R_s L_s}{2w_c} \exp\left(-\frac{d}{L_s}\right), \tag{5.2}$$

where the spin injection efficiency P is assumed to be equal for the injection and detection contacts, I is the applied current, R_s and L_s the sheet resistance and spin diffusion length, respectively, and w_c the width of the contact, which equals the width of the mesa. The exponential decay of ΔV_{NL} with a distance d is demonstrated in figure 5.4, where ΔV_{NL}, which is plotted over d on a semi-logarithmic scale, does show a linear slope. Utilizing a linear fit, the spin injection efficiency and spin diffusion length were calculated as $P = 56\,\%$ and $L_s = 7.2\,\mu\mathrm{m}$. With P being in the range of previous results [37, 110], a highly spin polarized curernt can be injected into a 2DEG. L_s provides a length scale for the feasible distance between spin injection and spin detection in any all-electrical spin detection method.

Further insight on the properties of spin transport can be gained with Hanle measurements [48], where an out-of-plane magnetic field B_z is used to dephase a spin accumulation. More detailed information on Hanle measurements can be found in reference [117]. The trace of the Hanle measurement shown in figure 5.5, which was conducted at an excitation curernt of $I = 1\,\mu\mathrm{A}$, does exhibit the expected shape, which demonstrates a successful Hanle measurement. The inset shows the measurement data over the full magnetic field range from $[-1\,\mathrm{T}, 1\,\mathrm{T}]$.

In this work, however, the importance of figure 5.5 does not lie in the extraction of spin transport parameters but rather in the field strength re-

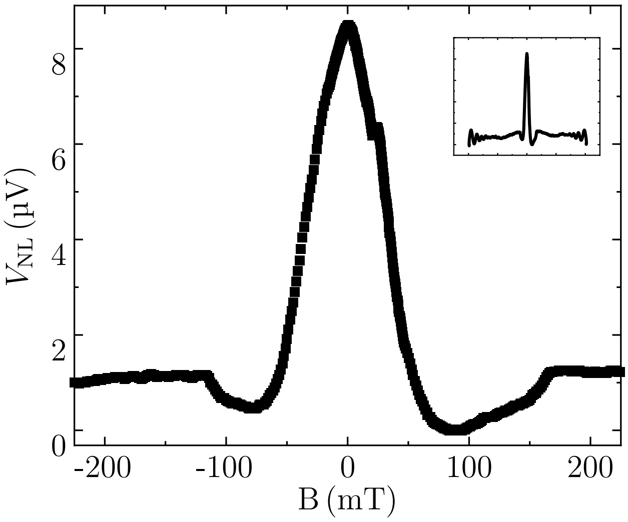

Figure 5.5: Trace of a Hanle measurement at an excitation current of $I = 1\,\mu\mathrm{A}$. To dephase a spin accumulation, an out-of-plane magnetic field of $\mathrm{B}_z \sim 150\,\mathrm{mT}$ is required. At around $\mathrm{B}_z \sim 60\,\mathrm{mT}$, however, the amplitude of a spin accumulation is significantly reduced. The inset shows the data over the full magnetic field range $\mathrm{B} \in [-1\,\mathrm{T}, 1\,\mathrm{T}]$

quired to suppress the spin-related signal. An out-of-plane magnetic field of $\mathrm{B}_z = 150\,\mathrm{mT}$ is required to fully dephase the spin accumulation. As will be discussed in the next section, however, low magnetic fields are advantageous in this work. Although an out-of-plane magnetic field of $\mathrm{B}_z \sim 60\,\mathrm{mT}$ is not enough to completely dephase the spin accumulation, it does significantly reduce its amplitude, suppressing large parts of the spin-related signal.

5.2 Quantized Conductance

This section presents a discussion of the realization of quantized conductance by means of the split-gate technique. First, the determination of a suitable split-gate layout is covered, followed by a characterization of the quantum point contact (QPC).

Using a split-gate to form a constriction, which creates a narrow channel, has been pioneered by Thornton [118] and Zheng [119]. At the constriction, electrons travel through a saddle point potential $V = V_0 - \frac{1}{2}m^*\omega_x^2 x^2 + \frac{1}{2}m^*\omega_y^2 y^2$ and have a transmission probability given by equations 3.14 and 3.15, where x represents the direction of the electron flow. Important quantities are the curvatures ω_x and ω_y of the saddle point potential. It is, in fact, the ratio of ω_y/ω_x that determines the sharpness of the conductance steps [70], where $\omega_y/\omega_x > 2$ is preferable. In addition, the length of the constriction should not exceed the mean free path l_{MFP} of the sample as quantinzed conductance is a ballistic phenomenon.

5.2.1 Split-Gate design

A number of factors can result in a deviation from the ideal quantized conductance, including the presence of impurity sites in the constriction [120], backscattering, or a nonideal split-gate design. To eliminate effects unrelated to the latter, the split-gate design was developed on a different wafer.

This wafer, also based on GaAs, has a 2DEG which resides 90 nm below the surface. The sample fabrication process was analogous to the steps described in section 4.3 with a few exceptions. The most significant alteration was the absence of a GaMnAs layer, which resulted in the omission of the wet chemical etching procedure to remove portions of the heterostructure. This results in a very smooth surface on which the split-gates can be deposited. Furthermore, the split-gates were deposited directly on the wafer, eliminating the need for an insulating material such as aluminum oxide. Thus, the electric field constricting the 2DEG should not be smeared out. More imporantly, however, this wafer has a very mobility. With a mobility of $\mu_{\mathrm{e}} = 2.3 \cdot 10^6\,\mathrm{cm}^2/\mathrm{Vs}$, the mobility is almost four times that of the wafer used in this work for spin injection.

The split-gates were lithographically defined with a parabolic shape in the vincity of the constriction. At first, the layout as shown in the SEM image of figure 5.8 (a) was used. The resulting conductance measurements are represented by the red curve in figure 5.8 (c). Plateaus around integer values of $2e^2/h$ are not well defined and the transitions between the plateaus are smeared out.

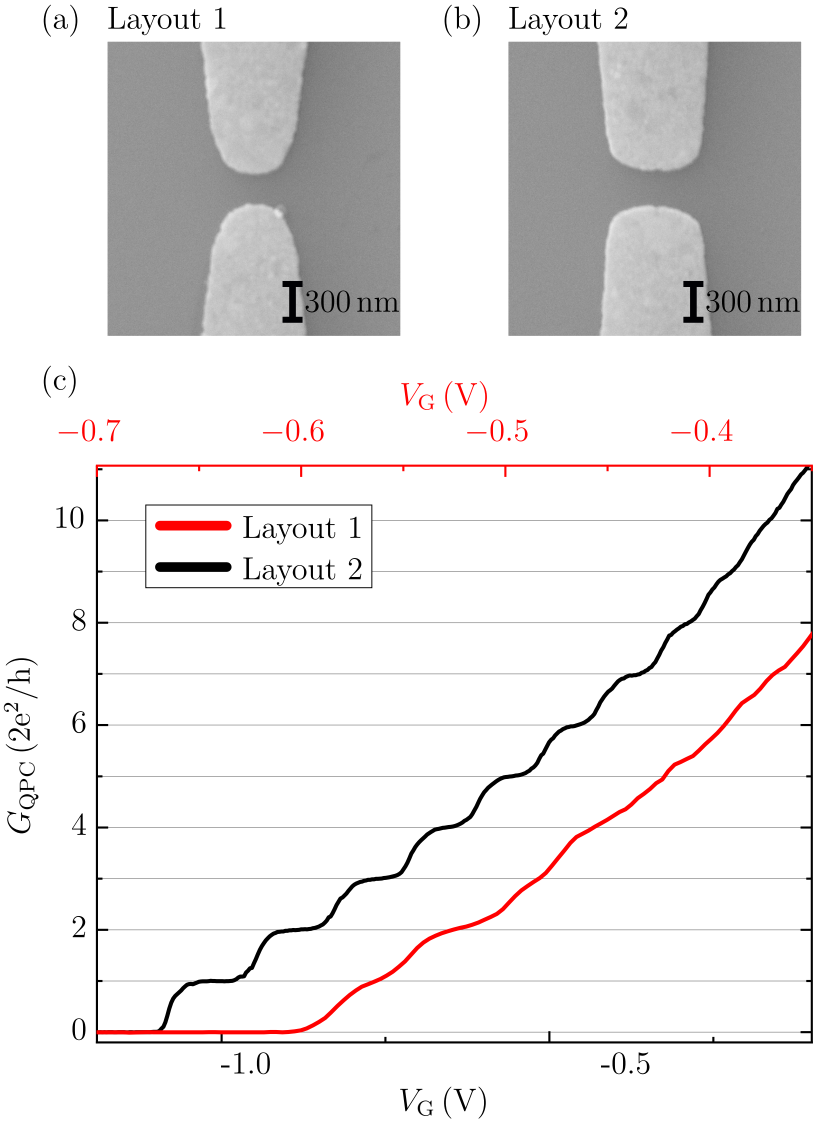

Figure 5.6: The pair of split-gate electrodes in (a) has a higher curvature than the one dipicted in the SEM image in (b). (c) Measurement of quantized conductance. The sample with the low curvature of the split-gates exhibits clear quantized conductance with well definded, sharp steps.

To enhance the quality of the steps, the ratio of ω_y/ω_x has to be increased. This is achieved by reducing the curvature of the split-gate, resulting in a reduction of ω_x. An SEM image of the layout with reduced curvature is shown in figure 5.8 (b). The curvature exhibits $y = x^2$ for $x \in [-0.32\,\mu\text{m}, 0.32\,\mu\text{m}]$ and is greatly increased away from the constriction to keep it sufficiently short. The resulting conductance curve (black) in figure 5.8 (c) shows 9 well defined plateaus and sharp steps, whereas the 10th mode is only visible as a small shoulder.

With a split-gate distance of 270 nm and a Fermi wave length of $\lambda_F \approx$ 50 nm, it is expected that $\approx 10 - 11$ modes are visible in a measurement [71]. The small deviation between the expected and measured number of steps suggests a small depletion length [121], i.e., a small lateral electric field component. The clear visibility of the plateaus as well as the abruptness of the transition between modes suggests that the shape of the split-gates is suitable for QPC experiments in this work.

5.2.2 QPC Characterization

The split-gate design, as shown in figure 5.6 (b), was then replicated on a device fabricated from the wafer structure described in Section 4.2. As previously stated, the sample has to be illuminated with a red LED after cooling it cryogenic temperatures to enhance the mobility and sheet carrier density.

The impact of the illumination on the characteristics of the QPC can be observed in figure 5.7 (a), which depicts the conductance curves of the device following illumination for varying durations. The blue curve was measured after the shortest time under light exposure, followed by the red, black, and dashed curves, respectively, after successive illumination. The inset shows the black curve over the entire measurement range of $V_\text{G} \in [-1.92\,\text{V}, 0\,\text{V}]$. The trace can be devided into two parts. For higher gate voltages the conductivity changes at a rapid rate as the 2DEG under the gate is depleted. Once the gate voltage is sufficiently small, the channel's width is reduced laterally until G reaches zero, where the channel is "pinched-off". While the traces shown were moved laterally to enable better comparability, it can be observed that with increasing light exposure, the pinch-off point is moved towards lower gate voltages. Furthermore, it can be seen that increasing the carrier density and mobility enhances the quality of the measured plateaus. For the black curve, four modes are visible, in contrast to the red and blue traces, where three and zero modes are observed, respectively. However, if the sample has been illuminated for an excessive duration, the quality of the measured plateaus will deteriorate. Prolonged exposure to light will no longer alter the carrier

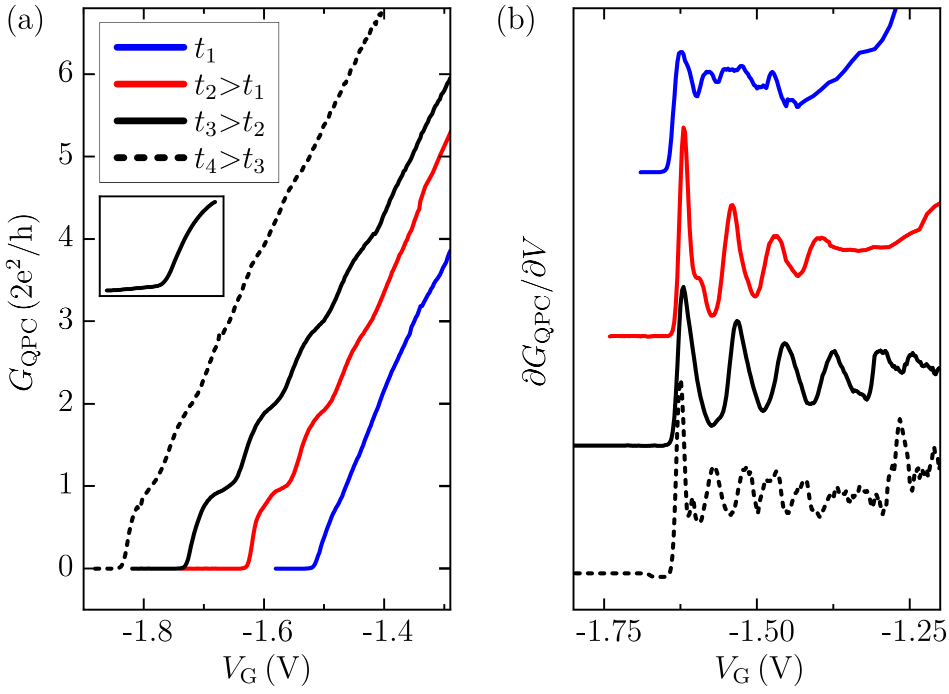

Figure 5.7: (a) Conductance measurements of the same sample for various illumination times t_i. For better visibility, the curves have been shifted in V_G. The inset shows the black curve over the full measurement range $V_\mathrm{G} \in [-1.92\,\mathrm{V}, 0\,\mathrm{V}]$. Illumination increases the quality of steps. However, when the sample is illuminated for too long, the step quality decreases again. The transconductances $\partial G_{\mathrm{QPC}}/\partial V_\mathrm{G}$ displayed in (b) show that especially higher order modes can be better observed for longer illumination times.

density, yet will result in a reduction in mobility. The influence of illumunation is also reflected in the derivative $\partial G_{\mathrm{QPC}}/\partial V_\mathrm{G}$ of the conductance (also called transconductance) traces with respect to split-gate voltage, which is shown in figure 5.7 (b). The blue curve shows no peaks, while the red and black curves have 3 and 4 peaks, respectively. The curves were offset vertially for better visibility.

The enhacement of quantized conductance after illumination is caused by the increased mobility and sheet carrier density n_s. Deviations from ideal quantized conductance arise due to backscattering at the constriction [68]. Reasons for backscattering include potential fluctuations from ionized impurities, which cause random disorder in the electrostatic potential landscape [122–125]. The effect of disorder can be reduced by enhanced screening if n_s is increased.

Following illumination, the conductance steps are well-defined, yet only a few steps are observed. With a Fermi wave length of $\lambda_F = 40\,\text{nm}$ it is expected that $\approx 13 - 14$ steps can be observed, which is in contrast to 4 measured modes. This suggests a lateral depletion of 95 nm due to the electric field and a channel width of $\sim 80\,\text{nm}$.

The fact that only 4 steps are visible in figure 5.7 is in contrast to the conductance curves shown in figure 5.6, which display 9 well defined plateaus. Furthermore, it is evident that the steps in the black curve presented in figure 5.7 are less distinct than those in figure 5.6. As the split-gate layout is identical, the discrepancy can be attributed to the utilized wafers. The observed difference in step quality can be explained by a difference in mobility, which is approximately four times greater in the case of the wafer used in the previous section. The discrepancy in the number of observed steps may be attributed to the spatial separation between the 2DEG and the split-gates. With the inclusion of the AlOx insulating layer, the 2DEG is situated at a depth of approximately 215 nm below the gate, which is $\approx 2.2\times$ the depth of the wafer used in the previous section. This may result in additional lateral contrictions due to in-plane components of the electric field of the split-gates. However, this increase is $3.6\times$, which suggests that structures with deep 2DEGs may exhibit different electrostatics, as has been pointed out before [126]. It is, however, likely that the deciding factor is the mobility of the wafer. While projecting small patterns from a surface gate onto deeper 2DEGs becomes increasingly difficult, it has to be pointed out that clear quantized conductance has been measured before in a GaAs/$\text{Al}_{0.33}\text{Ga}_{0.67}\text{As}$ 2DEG formed 277 nm beneath the surface [126]. In the aforementioned work, the mobility was $\mu_\text{e} = 3 \cdot 10^6 \text{cm}^2/\text{Vs}$.

Further insight into the properties of a QPC can be gained by finite-bias measurements. Superimposing[1] a DC voltage V_DC, which alters the energetic separation of the source μ_S and drain μ_D chemical potentials, with an applied AC bias serves as an energy reference, allowing the determination of the individual subband energy spacings [126–128]. This is illustrated by the band diagram in figure 5.8, which shows parabolic subbands separated by the subband spacing Δ_SB. In the case of a small applied DC bias (a) the chemical potentials μ_S and μ_D on both sides of the QPC are in the same subband. In a conductance measurement, integer values of $2\text{e}^2/\text{h}$ can be observed. If the difference between the chemical potentials due to an increase in V_DC is sufficiently large (b), μ_S and μ_D are separated by one subband. As the subband in between the chemical potentials contributes half to the total conductance, $G = (2\text{e}^2/\text{h})(\text{n} - \frac{1}{2})$ is expected and so called half-plateaus form. Once two subband bottoms are separating μ_S and μ_D, integer values of $2\text{e}^2/\text{h}$ are re-

---

[1] The measurement setup and the AC/DC adder are described in section 4.4.

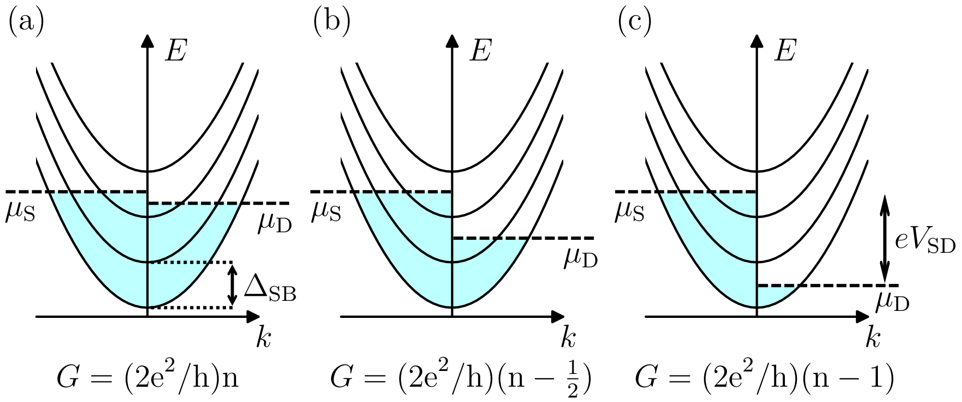

Figure 5.8: (a) For a low applied source-drain bias V_{DC} the chemical potential μ_S and μ_D on both sides of a split-gate reside in the same subband and the conductance reaches integer values of $2e^2/h$. (b) Upon a sufficient increase of V_{DC}, one subband separates μ_S and μ_D and half-plateaus form with $G = (2e^2/h)(n - \frac{1}{2})$. (c) Once the chemical potentials are separated by two subbands, integer values of $2e^2/h$ are restored. Adapted from [129].

stored.

In the top part of figure 5.9 (a) conductance measurements for $V_{DC} = 0\,\text{mV}$ (black) and $V_{DC} = 4\,\text{mV}$ (red) are shown. In the case of a finite source-drain bias, multiple half-plateaus are observed, indicating a clean sample [129]. Higher order integer plateaus are obscured by noise and cannot be clearly resolved, which is a usual phenomenon [129, 130] (curves not shown). The bottom part of figure 5.9 (a) shows the derivative of the respective curves. In both cases, clear maxima are visible which appear shifted by half a period between the curves. In the color plot shown in figure 5.9 (b) a diamond like pattern emerges. Color-coded is the transconductance $\partial G_{QPC}/\partial V_G$ over applied split-gate voltage V_G and source-drain bias V_{DC}. Blue areas, indicating low $\partial G_{QPC}/\partial V_G$ represent plateaus in conductance, whereas red areas occur at the transition between modes, where $\partial G_{QPC}/\partial V_G$ is high.

The values of V_G where a maximum in $\partial G_{QPC}/\partial V_G$ occurs are plotted for every value of V_{DC} in figure 5.10. Upon applying a finite V_{DC}, the single peaks in transconductance at a given subband split into two peaks. This splitting increases with higher V_{DC}. For the n^{th} subband, the peak is split into n^+ and n^-, where the +(-) indicates that the peak shifts towards higher (lower) gate voltages. The points in the evolution of maximum values of $\partial G_{QPC}/\partial V_G$, where the n^+ and $(n+1)^-$ peaks merge are highlighted in red. As mentioned before, V_{DC} can be used as an energy reference. The red points in figure 5.10 mark the energy values where μ_S and μ_D are one subband spacing apart $\Delta_{SB,n} = eV_{DC}$ (see figure 5.8). The extracted values are $\Delta_{SB,1} = 4.8\,\text{meV}$, $\Delta_{SB,2} = 3.4\,\text{meV}$

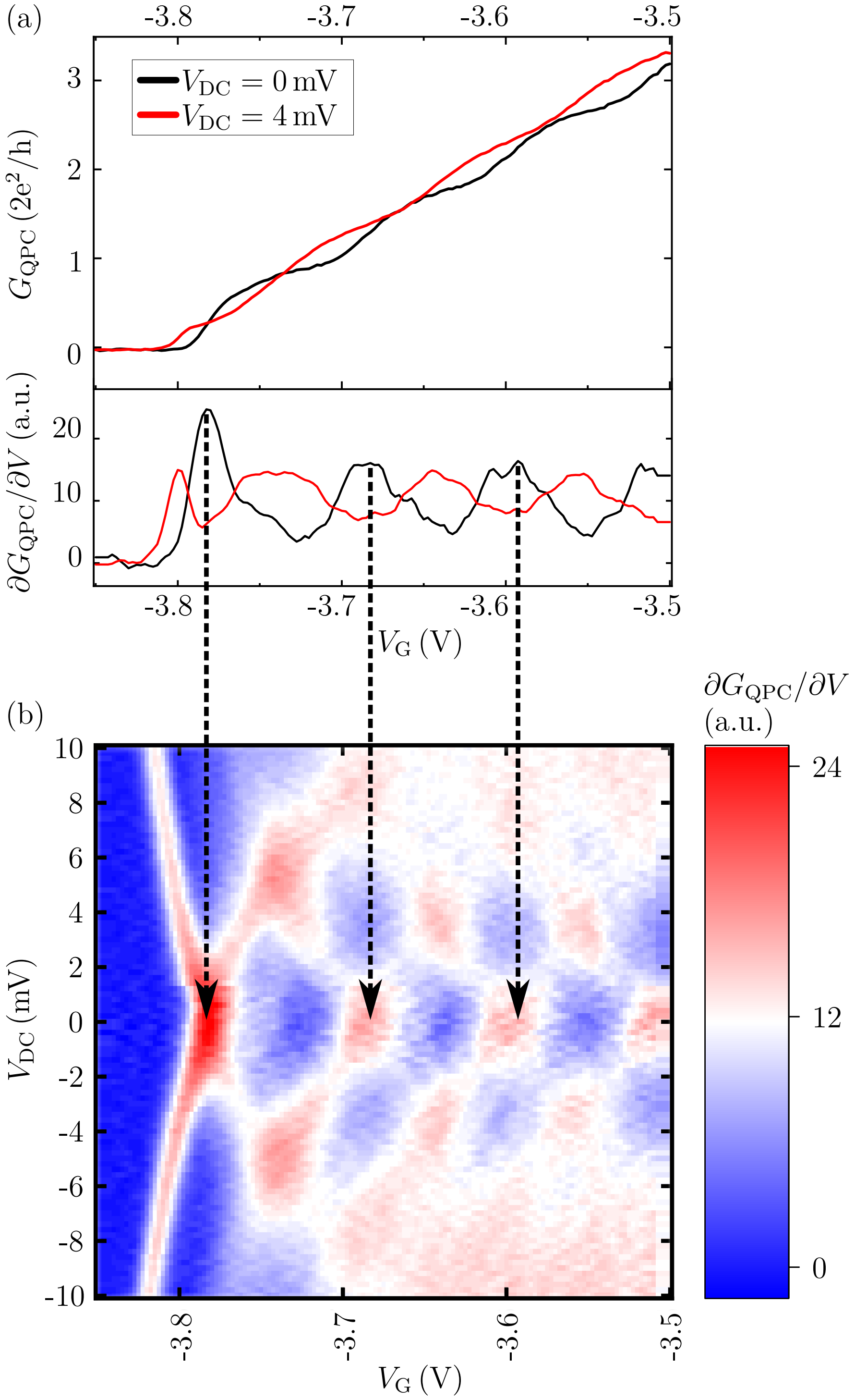

Figure 5.9: (a) Conductance curves (top) and the transconductance $\partial G_{\mathrm{QPC}}/\partial V_{\mathrm{G}}$ (bottom) of the measured signals at a source-drain voltage of $V_{\mathrm{DC}} = 0\,\mathrm{mV}$ (black) and $V_{\mathrm{DC}} = 4\,\mathrm{mV}$ (red). In the latter case, clear half-plateaus emerge. (b) Color plot of $\partial G_{\mathrm{QPC}}/\partial V_{\mathrm{G}}$ over V_{G} and V_{DC}. Blue areas, indicating low $\partial G_{\mathrm{QPC}}/\partial V_{\mathrm{G}}$, represent plateaus in conductance, whereas red areas occur at the transition between modes, where $\partial G_{\mathrm{QPC}}/\partial V_{\mathrm{G}}$ is high.

and $\Delta_{\mathrm{SB},3} = 2.8\,\mathrm{meV}$ for the first three modes, respectively. It is commonly observed that subband spacing increases with decreasing number of modes [126, 128, 129].

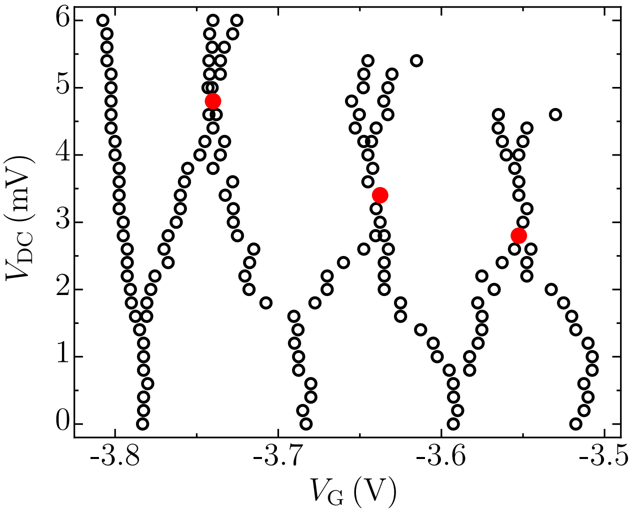

Figure 5.10: Evolution of the maxima in transconductance over applied split-gate voltage V_{G} for various values of V_{DC}. The values where the split peaks of two subbands merge is equal to the subband spacing $\Delta_{\mathrm{SB}} = \mathrm{e}V_{\mathrm{DC}}$ and are marked by the red dots.

As a next step, the curvature ω_x of the saddle point potential will be determined, which then allows to calculate the aforementioned ratio of ω_y/ω_x. To determine ω_x, the transmission probability is fitted to the measured conductance curve obtained at $V_{\mathrm{DC}} = 0\,\mathrm{V}$. The transmission probability through a QPC of a given mode n is given by equations 3.14 and 3.15 as

$$\begin{aligned} \mathcal{T}_{\mathrm{n}}(\varepsilon_{\mathrm{n}}) &= \frac{1}{1+e^{-\pi\varepsilon_{\mathrm{n}}}} \\ \varepsilon_{\mathrm{n}} &= 2\frac{E - \hbar\omega_{y,\mathrm{n}}(\mathrm{n}+1/2) - V_0}{\hbar\omega_x}, \end{aligned} \tag{5.3}$$

where $\hbar\omega_{y,\mathrm{n}} = \Delta_{\mathrm{SB,n}}$ is the subband spacing. To be able to fit the transmission probability to the measured conductance curve, the relation between the energy E and applied split-gate voltage V_{G} must be known. E and V_{G} are connected through the lever arm α, with $E = \alpha V_{\mathrm{G}}$ [129]. At the transition between modes, i.e., $\mathrm{n}+1 \to \mathrm{n}$ and $\mathrm{n} \to \mathrm{n}-1$ modes, the transmission probability of the given mode is given by $\mathcal{T}_{\mathrm{n}}(\varepsilon_{\mathrm{n}}) = 1/2$ and $\mathcal{T}_{\text{n-1}}(\varepsilon_{\text{n-1}}) = 1/2$, respectively[2].

To obtain $\mathcal{T}_{\mathrm{n}}(\varepsilon_{\mathrm{n}}) = \mathcal{T}_{\text{n-1}}(\varepsilon_{\text{n-1}}) = 1/2$ in equation 5.3 for a given mode, the conditions

$$\begin{aligned} \hbar\omega_{y,\mathrm{n+1}}(\mathrm{n}+1/2) + \alpha V_{\mathrm{G,n}} - V_0 = 0 \\ \hbar\omega_{y,\mathrm{n}}(\mathrm{n}-1+1/2) + \alpha V_{\text{G,n-1}} - V_0 = 0 \end{aligned} \tag{5.4}$$

---

[2] One has to be careful here. The transmission probability for the first subband is given by $\mathcal{T}_0(\varepsilon_0)$ while the energy spacing of the first subband is denoted by $\hbar\omega_{y,1}$

have to be fulfilled (i.e., $\varepsilon_{\mathrm{n}} = \varepsilon_{\mathrm{n\text{-}1}} = 0$). Here, $V_{\mathrm{G,n}}$ is the split-gate voltage at the transition between modes. From this, the lever arm can be calculated by subtracting the terms in equation 5.4 and one obtains

$$\alpha = \frac{\omega_{y,\mathrm{n}+1}(\mathrm{n}+1/2) - \omega_{y,\mathrm{n}}(\mathrm{n}-1/2)}{\Delta V_{\mathrm{G}}}. \tag{5.5}$$

With the lever arm known, equation 5.3 can be fitted to the measured conductance curve with two unknown variables, $\hbar\omega_x$ and V_0. For future experiments, the point of interest is the transition between 0 and 1 modes. Before the fit can be done, a series resistance of $R_s = 1.6\,\mathrm{k\Omega}$ has to be subtracted from the measured conductance signal. Figure 5.11 shows the measured data (black) as well as the fit for the lowest subband (red). The curvature of the QPC is calculated as $\hbar\omega_x = 1.84\,\mathrm{meV}$, which gives a ratio of $\omega_y/\omega_x = 2.6$. These experiments suggest that the shape of the split-gate and the resulting parabolic potential is suitable for QPC measurements and that the deviation from ideal quantized conductance comes from the wafer properties rather than the split-gate design.

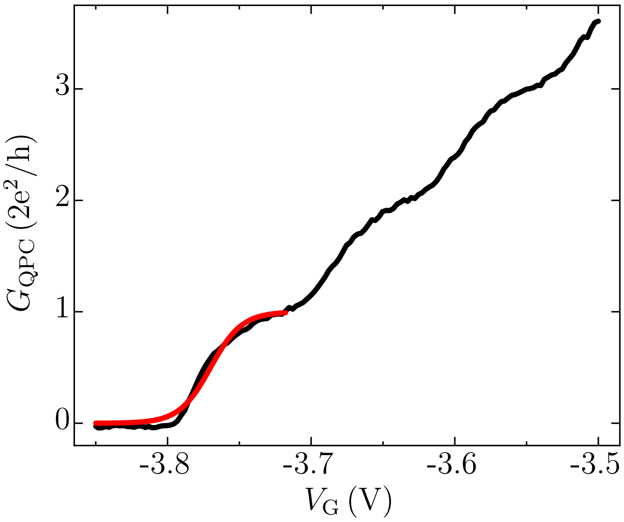

Figure 5.11: Fit of the transmission probability for the first mode (red) and the measured data (black). Using $\hbar\omega_y = 4.8\,\mathrm{meV}$ one obtains $\hbar\omega_x = 1.84\,\mathrm{meV}$ from the fit. The high ratio of ω_y/ω_x suggests that the parabolic potential originating from the split-gates is suitable for QPC measurements.

Finally, the influence of a perpendicular magnetic field on the properties of the QPC is analysed. A field may exert an influence at the entrance and exit of the constriction imposed by the split-gates, where electrons may be backscattered and therefore cannot pass through the constriction. This backscattering is the origin of a nonzero resistance of a QPC [70, 72, 76, 120]. By applying an out-of-plane magnetic field[3] the impact of geometric backscattering can be

---

[3] High perpendicular magnetic fields are the reason why the quantization can be measured very accurately using the quantum Hall effect, opposed to QPC measurements [131].

reduced while the energy barrier of the QPC is unaffected.

In figure 5.12 a conductance measurement is shown for a perpendicular magnetic field of B = 0 mT (black) and B = 50 mT (red). No strong visible difference between the measured traces appears. The transconductances for B = 0 mT (blue) and B = 50 mT (cyan) also show marginal difference in the peak signal.

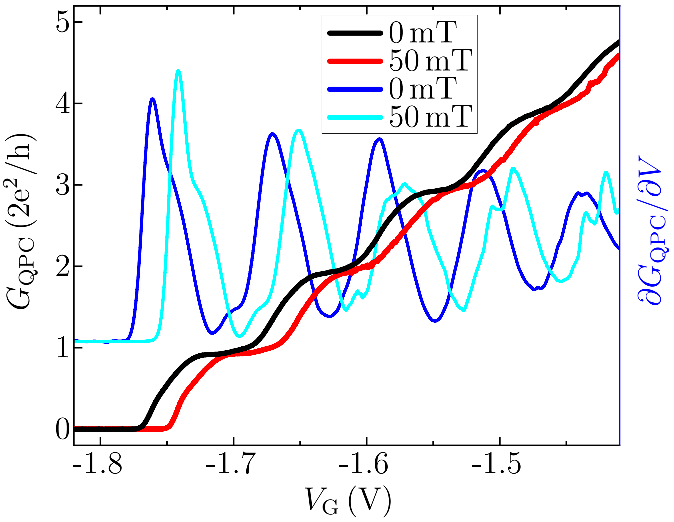

Figure 5.12: Conductance (black, red) and transconductance (blue, cyan) in an out-of-plane magnetic field of B = 0 mT and B = 50 mT, respectively. For the small magnetic field used here, the signal does not change significantly.

In the next chapter, a signal which is linear in the transconductance will be measured in a small out-of-plane magnetic field. As shown in figure 5.12, the transconductance does not significantly change in the field range used here and the basic properties of the QPC are unaffected.

5.3 Conclusion

The basic properties of spin injection and quantized conductance for the heterostructure used in this work were analysed.

Utilizing spin valve measurements with a varying distance between the injector and detectors, a spin diffusion length of $L_s = 7.2\,\mu\mathrm{m}$ and spin injection efficiency of $P = 56\,\%$ were determinded. This confirms efficient spin injection and spin transport of the heterostructure and also gives a lengthscale for electrical spin detection. Spin valve signals could be obtained up to a distance of 25 µm using an excitation current of $I = 2\,\mu\mathrm{A}$. Hanle measurements confirmed that a perpendicular magnetic field of 60 mT significantly suppresses a spin accumulation due to dephasing.

For achieving quantized conductance, the saddle point potentials should have a ratio of $\omega_y/\omega_x > 2$ [70]. Defining a split-gate electrode with a low curvature ($x = y^2$ for $x \in [-3.2\,\mu\mathrm{m}, 3.2\,\mu\mathrm{m}]$) yields 4 well resolved plateaus for a split-gate separation of 270 nm. By illuminating the sample the quality and number of visible plateaus can be increased.

Further insights into the properties of a QPC were gained from source-drain biasing measurements. Clear half-plateaus were seen, which indicates a high cleanliness of the sample. Utilizing the source-drain bias as an energy reference, the subband spacing was determined. For the first subband $\hbar\omega_y = 4.8\,\mathrm{meV}$ was extracted. When the transmission probability of a QPC was fitted to the measured conductance data, the curvature of the saddle point potential was determined as $\hbar\omega_x = 1.84\,\mathrm{meV}$. This yields a ratio of $\omega_y/\omega_x = 2.6$ which shows that the chosen split-gate design is suitable for achieving quantized conductance and that deviations from nonideal quantization arise from factors unrelated to the split-gate design.

The goal of this work is to utilize a QPC as an energy barrier to measure a spin accumulation. All prerequisites, namely efficient spin injection and spin transport as well as quantized conductance, are met.

Chapter 6

Measuring Spin Accumulation using a QPC

In this chapter the experimental results for the main objective of this work are discussed: using a QPC as an energy barrier to detect a spin accumulation.

In section 6.1, a brief overview of the theory of linear and nonlinear spin-to-charge conversion is given, while the experimental results are shown in section 6.2.

6.1 Theory of linear and nonlinear Spin-to-Charge conversion

The theory of nonlinear spin-to-charge conversion was developed by Stano *et al.* [132, 133]. The basic idea originates in the fact that in a quantum point contact the transmission $\mathcal{T}(E)$ depends on the energy E of a particle (see equations 3.14 and 3.15).

Assuming that the spin orientation of a carrier is conserved at the transmission, the transmission probability reads

$$\mathcal{T}_{12}^{\sigma\sigma}(E) = \mathcal{T}(E) + \sigma\,\delta\mathcal{T}(E), \tag{6.1}$$

where 12 denotes transmission from the left to the right side of the QPC, σ is the spin species and $\delta\mathcal{T}(E)$ represents an adjustment to the transmission coefficient that is reliant on the spin orientation.

With respect to the Fermi energy, the electrochemical potential of a spin subband is given by $\mu_{\mathrm{i}}^{\sigma} = eV_{\mathrm{i}} + \sigma\,\delta\mu_{s\mathrm{i}}$ where i=1(2) represents the left (right) side of the QPC, V_{i} is the applied voltage and $\delta\mu_{s\mathrm{i}}$ is the spin accumulation on either side of the contriction.

Utilizing a Landauer-Büttiker formalism, the current through the constriction can be calculated as

$$I = G_1 e\delta V + G_2(\delta\mu_{s1}^2 - \delta\mu_{s2}^2) + G_3(\delta\mu_{s1} - \delta\mu_{s2}) + G_4(\delta\mu_{s1} + \delta\mu_{s2})e\delta V \quad (6.2)$$

with the conductances

$$G_1 = \frac{2e}{h}\int dE(-\partial_E f)T(E) \quad (6.3a)$$

$$G_2 = \frac{e}{h}\int dE(-\partial_E f)[\partial_E T(E)] \quad (6.3b)$$

$$G_3 = \frac{2e}{h}\int dE(-\partial_E f)\delta T(E) \quad (6.3c)$$

$$G_4 = \frac{e}{h}\int dE(-\partial_E f)[\partial_E \delta T(E)], \quad (6.3d)$$

where G_1 is the standard conductance of a QPC. If a spin accumulation $\mu_{s1/2}$ is present on either side of the constriction, additional contributions to the current through the QPC emerge. The second term in equation 6.2 represents nonlinear spin-to-charge conversion, which does not depend on the sign of a spin accumulation. As represented in figure 6.1 (a), the quadratic relation between current and spin accumulation originates in the energy dependence of both the Fermi energy $f_\mathrm{i}^\sigma = f(E - \mu_\mathrm{i}^\sigma)$ and the transmission coefficient $T(E)$. The third and fourth terms are conversion terms that describe the linear relationship between spin and charge which originates in the Zeeman energy from an external magnetic field, as shown in figure 6.1 (b). G_3 and G_4 are, respectively, linked to the difference between and average of spin accumulation on both sides of the QPC. Close to the pinch-off, one can set $\delta\mu_{s1} = \delta\mu_s$ and $\delta\mu_{s2} = 0$. If the constriction is not sensitive to spin, as is the case for zero external magnetic field, one finds $\delta\mathcal{T}(E) = 0$ and the conductances $G_3 = G_4 = 0$ vanish.

Generally, there are two methods to measure nonlinear spin-to-charge conversion. One approach is to keep both sides of the QPC at the same potential ($\delta V = 0$) and measure the current $I = G_2\delta\mu_s^2$. Alternatively, one side of the QPC can be set as a floating probe. A voltage that ensures no charge current flows through the constriction can be accessed as

$$e\delta V(2\omega) = -\frac{1}{2}\frac{G_2}{G_1}\delta\mu_s^2 \quad (6.4)$$

by measuring the second harmonic voltage drop. In this work, the latter approach is used. Consequently, the measured signal $\delta V(2\omega)$ is related to the transconductance of the QPC, which is due to $G_2 \propto \partial_E G_1$. The peak sig-

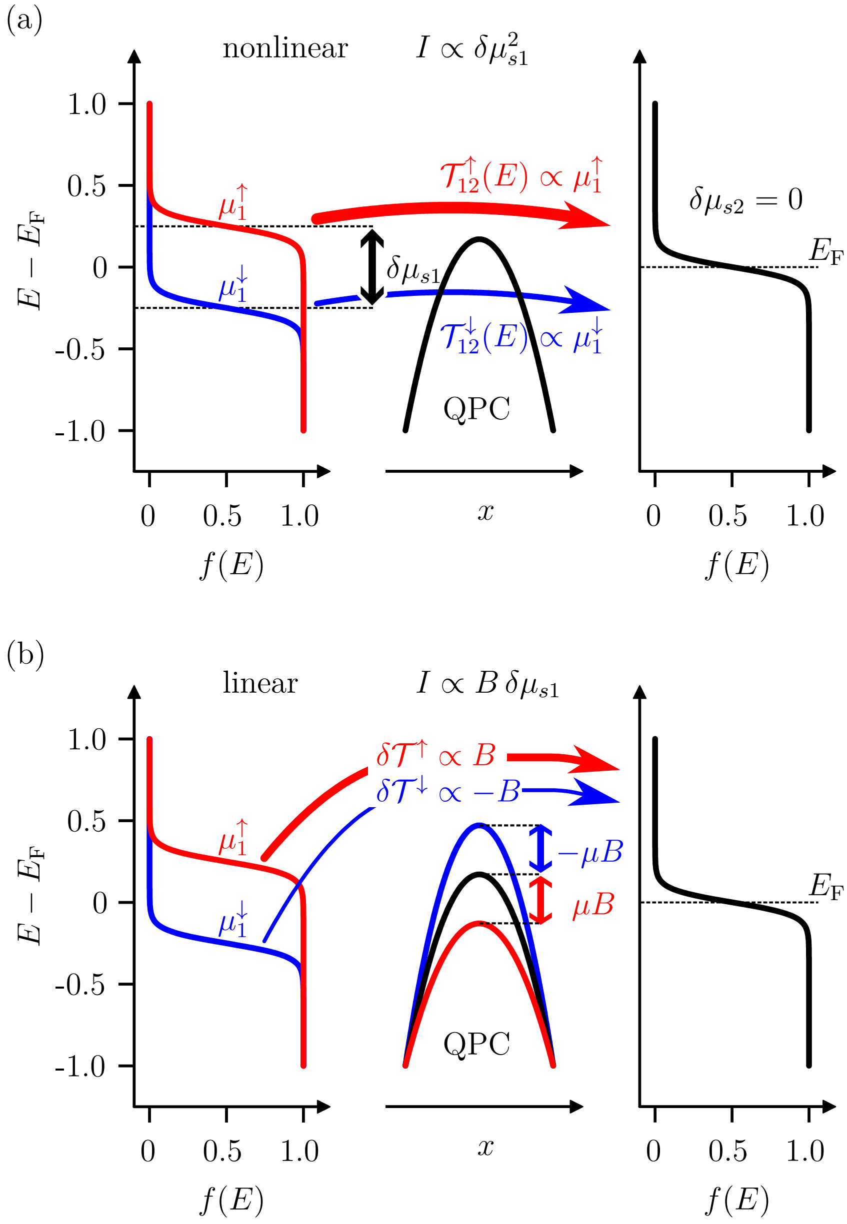

Figure 6.1: (a) Nonlinear spin-to-charge conversion. If a spin accumulation $\delta\mu_{s1}$ is injected at the left side of a QPC, a current flows through the constriction even in the absence of applied bias. As the transmission probability $\mathcal{T}(E) \propto \delta\mu_{s1}$, the net current $I \propto \delta\mu_{s1}^2$ is nonlinear. (b) In a magnetic field B (anti)parallel to spin-up(down) electrons, the energy barrier imposed by a QPC decreases (increases). As a consequence, the transmission coefficients for the spin subbands differs by $2\delta\mathcal{T}$. The additional current I is linear in B and $\delta\mu_{s1}$.

nal is then observed between plateaus at $G_1 = (\mathrm{N} + 1/2)\, 2\mathrm{e}^2/\mathrm{h}$. In addition, $\delta V_{\mathrm{peak}}(2\omega) \propto 1/(\mathrm{N}+1/2)$ increases with fewer transport modes N and is maximal when the QPC is half open. It has to be noted that from a mathematical perspective, $\delta V(2\omega) \to \infty$ for $G_1 \to 0$ which can be solved by adding a small constant to G_1.

By applying an in-plane magnetic field, the constriction becomes spin sensitive. Due to the Zeeman energy, the transmission probability changes as $E \to E - \sigma\mu B$ in equation 5.3. The difference in transmission for the spin subbands then reads

$$\delta\mathcal{T} = -\mu B \partial_E \mathcal{T}(E), \tag{6.5}$$

where $\mu = (g/2)\mu_\mathrm{B}$ is the magnetic moment, with g the g-factor and μ_B the Bohr magneton. G_3 is linear in both transconductance and the applied magnetic field, whereas G_4 depends on the slope of the transconductance with respect to the applied gate voltage.

For a floating probe (i.e., $I = 0$), equation 6.2 becomes

$$-G_1 \mathrm{e}\delta V(\omega) = (G_3 + G_4 \mathrm{e}\delta V(\omega))\delta\mu_s \tag{6.6}$$

when measuring at the excitation frequency ω. At maximum transconductance close to the pinch-off, i.e., at $G_1 = \mathrm{e}^2/h$ one finds $G_4 = 0$. In this case, for $B \to 0$, the slope of $V(\omega)$ with respect to the applied magnetic field gives information on the spin accumulation as [134, 135]

$$\left.\frac{\partial(\delta V(\omega))}{\partial B}\right|_{B=0} = \frac{g\mu_\mathrm{B}\pi}{2\mathrm{e}\hbar\omega_x}\delta\mu_s. \tag{6.7}$$

Due to the difference in chemical potentials of the spin subbands, different transmission probabilities arise. If a magnetic field is applied antiparallel to the spin accumulation, the Zeeman energy penalty compensates the difference in transmission. The net current becomes compensated if

$$\delta\mu_s = g\mu_\mathrm{B} B_c. \tag{6.8}$$

The compensation field B_c gives information on both the sign and magnitude of the spin accumulation.

Linear spin-to-charge conversion was measured by Nichele *et al.* [134] in a 2-dimensional hole gas, in which the spin accumulation was generated using the mesoscopic spin Hall effect (SHE) [136]. In contrast to the device used in this work, not relying on ferromagnetic electrodes to generate the spin accumulation allowed the investigators to apply large magnetic fields antiparallel to the spin accumulation. The theory from reference [133] was extended and showed that $\partial_B V(\omega) \propto \partial_E G_1/G_1$. In a tree-terminal setup, reminiscent of the letter 'T', a current was driven between terminals 1 and 2 and the tree-terminal voltage drop between terminals 1 and 3 is antisymmetric in a magnetic field. In addition to proving $\partial_B V(\omega) \propto \partial_E G_1/G_1$, changing the setup to have zero g factor yielded $\partial_B V(\omega) = 0$.

Nonlinear spin-to-charge conversion was measured by Marcellina *et al.* [135], also in a 2-dimensional hole gas with the intrinsic SHE [137] as the origin of the spin accumulation. The sample was structured as the letter 'H' [138, 139] which allowed to measure the inverse SHE at the same time. The measured three-terminal voltage $V(2\omega) \propto I_{\text{sd}}^2$ showed the expected dependence on the source-drain voltage and decreased once the spin accumulation was suppressed by a magnetic field.

In our devices used in this work, the magnitude of the spin accumulation at the QPC could be manipulated by varying both the applied bias I_{sd} as well as the distance between the spin injection electrode and the point of detection. An exponential decay of the measured signal with increasing spatial separation on the scale consistent with the spin diffusion length would be a clear sign that the measured signal is of spin origin.

Thermopower

In addition to nonlinear spin-to-charge conversion, the second harmonic voltage drop $\delta V(2\omega)$ across the constriction may also in part arise from thermopower. This is due to the fact that the underlying physics of nonlinear spin-to-charge conversion and thermopower, which will be derived in the following, have a similar origin. Using a Landauer-Büttiker formalism, a relation between the current flow I, heat flow Q and the difference in both the chemical potential $\Delta\mu$ and the temperature difference ΔT can be derived.

The current I and heat flow Q through a QPC are [140]

$$\begin{pmatrix} I \\ Q \end{pmatrix} = \begin{pmatrix} G & L \\ M & K \end{pmatrix} \begin{pmatrix} \Delta\mu/e \\ \Delta T \end{pmatrix} \tag{6.9}$$

where G and K are the electric and heat conductivity of a QPC, respectively, and L, M are thermo-electric coefficients. Similar to the previous section, the condition for a nonzero thermo-electric coefficient is that the conductance varies with energy [141].

Even in the absence of an applied bias, a temperature gradient across a QPC results in a voltage drop. For $I = 0$, the *thermopower* S is defined as

$$S = \left(\frac{\Delta\mu/\mathrm{e}}{\Delta T}\right)_{I=0} = -\frac{L}{G} \tag{6.10}$$

and relates a voltage drop $\Delta\mu/e = \Delta V$ across the QPC with the temperature difference. It is important to note that the thermopower $S \propto 1/(\mathrm{N}+1/2)$ increases with decreasing number of transport modes N.

In the samples used in this work, a current flows on one side of the device which is separated from the other side by means of a QPC. Due to Joule heating, a temperature gradient $T_\mathrm{e} - T_\mathrm{l}$ across the QPC emerges as the difference between the electron T_e and lattice temperatures T_l. For both diffusive [142] and ballistic [141] transport, the thermopower is linear in transconductance

$$S = \frac{\Delta V}{T_\mathrm{e} - T_\mathrm{l}}\bigg|_{I=0} = -\frac{\pi^2 k_\mathrm{B}^2}{3\mathrm{e}}(T_\mathrm{e} + T_\mathrm{l})\frac{\partial_E G}{G} \tag{6.11}$$

where k_B is the Boltzmann constant. Thus, maximum thermopower is expected between modes when the transconductance is maximal [143, 144] with [145, 146]

$$\Delta V_\mathrm{peak}^\mathrm{N} = -\frac{C(T_\mathrm{e}^2 - T_\mathrm{l}^2)}{\mathrm{N}+1/2} \tag{6.12}$$

which depends on the curvature of the saddle point potential $\hbar\omega_x$ as $C = \sqrt{2}\pi^3 k_\mathrm{B}^2/24\mathrm{e}\hbar\omega_x$.

The heat loss per electron $P = I^2 R_\mathrm{H}/n_\mathrm{s}A$ depends on the current I, the resistance of the heating channel R_H, sheet carrier density n_s and channel area A. In the linear response regime, the measured signal due to thermopower is $\Delta V_\mathrm{max}^\mathrm{N} \propto P$ [140, 146]. Consequently, the voltage drop across the QPC which corresponds to thermopower will appear as the second harmonic voltage drop: $S \propto \Delta V(2\omega)$.

Comparing equation 6.11 with equations 6.4 and 6.3b reveals that nonlinear spin-to-charge conversion and thermopower have the same slope. This is due to the fact that both contributions are $\propto I_\mathrm{sd}^2$ and have the origin in the energy dependence of $\mathcal{T}(E)$. Thus, when measuring $\Delta V(2\omega)$ it is important to verify wether the signal originates from a spin accumulation or thermopower.

6.2 Experimental Results

In this section the measurement results for both nonlinear and linear spin-to-charge conversion are presented. First, the results of nonlinear spin-to-charge conversion experiments are shown, followed by the discussion of the measurements on linear spin-to-charge conversion. In addition, experiments in a local configuration were conducted and the results are shown in the appendix C.

The presence of a QPC in non-local spin-to-charge conversion devices implies a slightly different measurement setup compared to the one used in the non-local spin valve measurements, described in the previous chapter (see section 5.1). Therefore, the measurement setup will be shown, after which measurements regarding nonlinear spin-to-charge conversion and linear spin-to-charge conversion will be discussed.

6.2.1 Measurement Setup

In a standard QPC measurement, a voltage source is connected to both sides of the constriction. This is in contrast to non-local measurements, for which the regions of applied bias and voltage measurement are spatially separated. In figure 6.2 the measurement setup for measuring spin-to-charge conversion in a non-local manner is shown. Similar to the spin valve measurements (see figure 5.1 and 5.2), an applied bias between a spin injection contact (yellow) and a reference contact (cyan), which is sufficiently far away from the spin contact, leads to a spin accumulation $\delta\mu_s(0)$ beneath the spin concact. The spin accumulation diffuses into all directions and decays exponentially with distance x from the spin contact as $\delta\mu_s = \delta\mu_s(0)\, exp(-x/L_s)$. If an energy barrier in form of a QPC (orange) is sufficiently close to the spin injection contact, a spin accumulation $\delta_{s1} \neq \delta_{s2}$ could be expected on both sides of the QPC. This spin accumulation should be detectable as a voltage drop across the QPC.

As mentioned in the previous section, the side of the QPC that is far away from the spin injection contact is maintained as a floating probe. This presents two challenges as the split-gate voltage V_G decreases and the constriction becomes narrower.

If V_G is decreased to values below pinch-off, the left and right side of the constriction become electrically separated. Consequently, the measured voltage drop across the QPC is no longer clearly defined, which manifests itself in an arbitrary voltage drop and a low signal-to-noise ratio.

If the QPC is half open, the resistance of the channel $R_\mathrm{QPC} = h/e^2 \approx 26\,\mathrm{k}\Omega$ is large. To avoid the influence of capacitive conversion, a voltage-amplifier with high impedance is used to measure the voltage drop across the QPC. In addition, the excitation frequency is reduced to $f_\mathrm{AC} = 1.07\,\mathrm{Hz}$ to eliminate the influence of capacitive effects. Measuring at low frequencies, however, introduces additional challenges in the form of increased noise and other parasitic effects[1]. In addition, measurements take a longer time as the

---

[1] At low frequencies, e.g., turning on the light in the lab can be seen in electric measurements.

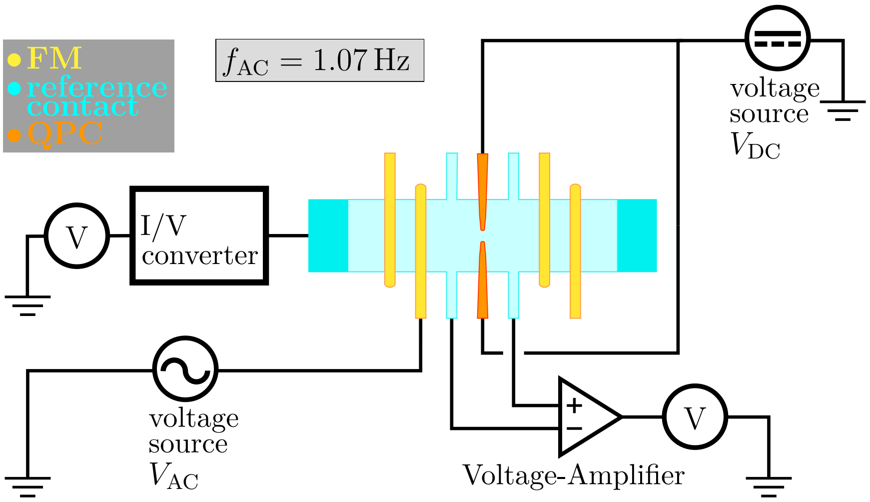

Figure 6.2: Setup for measuring spin-to-charge conversion in a non-local manner. A spin accumulation is injected into the mesa by applying a bias between a spin contact (yellow) and a reference contact (cyan). The spin accumulation then diffuses toward a QPC (orange), where it can be detected as a voltage drop across the constriction. When the QPC is close to pinch-off, the resistance of the sample increases. Therefore, a high-impedance voltage-amplifier is used to measure the voltage drop across the QPC. To avoid capacitive conversion, the excitation frequency $f_{\mathrm{AC}} = 1.07\,\mathrm{Hz}$ is low.

sweeping rate has to be decreased to allow for longer integration times of the lock-in amplifiers.

6.2.2 Nonlinear Spin-to-Charge Conversion

The black dotted curve in figure 6.3 shows the results of the conductance measurement on one of the samples. Details on the split-gate design and QPC characterization are given in section 5.2. Clear plateaus and sharp transitions can be seen, which is reflected in the high peaks in transconductance $\partial G_{\mathrm{QPC}}/\partial V$ of the QPC, represented by the black curve. The 'kink' in the last transconductance peak, which is marked by the black arrow, occurs at $G = 0.6\,(2\mathrm{e}^2/\mathrm{h})$ and hints at the 0.7 anomaly, which is still elusive in its origin [147–153].

Shown in various shades of red is the measured signal $V(2\omega)/I_{\mathrm{sd}}^2$, i.e., the second harmonic of the measured non-local voltage normalized by the square of the excitation current. The measurement was performed for $I_{\mathrm{sd}} \in [100, 200, ..., 1000\,\mathrm{nA}]$. There are two notable features in the plot. The shape of the measured signal correlates well with the transconductance, which includes features such as the 'kink' at the point before the QPC is half open, which is marked by the dark red arrow for the curve corresponding to $I_{\mathrm{sd}} = 200\,\mathrm{nA}$. Over the selected measurement range, which includes five subbands, $V(2\omega)/I_{\mathrm{sd}}^2$ shows the expected slope, with peaks reminiscent of a δ-function. The second important feature is that for the full range of selected excitation currents the curves collapse on a similar trace when normalized by I_{sd}^2. It has to be noted that for $I_{\mathrm{sd}} \in [100, 200, ..., 1000\,\mathrm{nA}]$ the normalized signal decreases for increased I_{sd}, while from the theory one expects a constant $V(2\omega)/I_{\mathrm{sd}}^2$, assuming a linear relation between the spin accumulation and I_{sd}. There are two possible reasons for the decrease of the normalized signal with increasing current. A first possible reason could be a nonlinear relation between the spin accumulatin and a current. For the current ranges used here, the spin accumulation is typically linear in I_{sd} [154]. A second reason for the decrease in $V(2\omega)/I_{\mathrm{sd}}^2$ with increased source drain bias may be that the theory for nonlinear spin-to-charge conversion is valid only for small variations in chemical potential. For increased currents, higher order terms in a Taylor expansion have to be taken into account and deviations from linear behavior are expected.

Figure 6.4 shows $V(2\omega)/I_{\mathrm{sd}}^2$ for $I_{\mathrm{sd}} = 200\,\mathrm{nA}$ (blue) and $I_{\mathrm{sd}} = 1\,\mu\mathrm{A}$ (cyan). The ratio of the two curves, $V(2\omega)(200\,\mathrm{nA})/V(2\omega)(1\,\mu\mathrm{A}) \cdot (1000/200)^2$, represented in red, shows similar values for all five transitions between the subbands. For higher order peaks, a moving average of the data, displayed in black, is shown to guide the eye due to the low signal-to-noise ratio. The fact that the ratio remains the same over the whole measurement range suggests that the linear response model is valid for many modes and for the currents used here.

The data presented in figure 6.5 extends the measurements shown in figure 6.3 to lower excitation currents. Contrary to the high excitation currents, the data collapses well onto a single trace for the range of currents shown here, $I_{\mathrm{sd}} \in [20, 30, ..., 100\,\mathrm{nA}]$, as expected. Shown in black is the transconductance of the QPC weighted by the conductance $\partial_V G_{\mathrm{QPC}}/G_{\mathrm{QPC}}$. The weighted transconductance and the measured data exhibit a similar slope over the entire measurement range. This shows that the voltage drop across the QPC follows not only the transconductance and its features (such as the 'kink'), but also the conductance of the QPC, as predicted from equation 6.4. Experiments with lower currents $I_{\mathrm{sd}} = 2,\ 5,\ 10\,\mathrm{nA}$ show the same slope. They are, however, not included in figure 6.5 due to excessive noise.

In this non-local experiment setup, the right side of the QPC is kept floating. Therefore, the total current passing through the QPC must be zero. Prior to the application of an excitation current, both sides of the constriction are at equal potential. When a non-local bias is generated, a current flows through

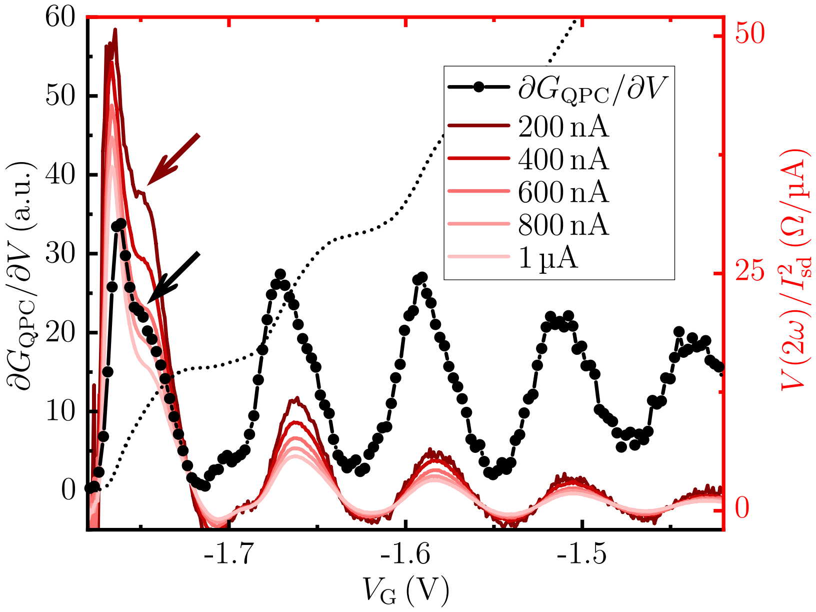

Figure 6.3: Results of a non-local spin-to-charge conversion experiment. The line with small dots shows the measured conductance of the QPC, while the black line with large dots displays the transconductance $\partial G_{\mathrm{QPC}}/\partial V$. Sharp peaks in the transconductance are observed due to the clearly quantized conductance. Shown in different shades of red is the measured non-local voltage drop across the QPC $V(2\omega)/I_{\mathrm{sd}}^2$ normalized by the square of the excitation current. For the currents used here, $I_{\mathrm{sd}} \in [100, 200, ..., 1000\,\mathrm{nA}]$, the measured curves collapse on a similar trace and follow the transconductance well.

the constriction due to the energy dependence of the QPC's transmission coefficient. A voltage drop, which is measured during experiment, maintains a restoring current to keep the total current at zero. At lower conductance, the voltage required to maintain the restoring current increases. The fact that the experiment follows the behavior expected from theory shows that the model used in the previous section is appropriate. A QPC can be used as an energy barrier.

Distance-Resolved Measurements

The curves shown in figures 6.3 and 6.5 display the slope as predicted from theory. At the moment, however, it unclear whether the voltage drop across the QPC is spin-related or due to other effects. To demonstrate that $V(2\omega)$ originates in spin, one approach is to conduct experiments with varying distances d between the spin injection contact and the constriction. From the

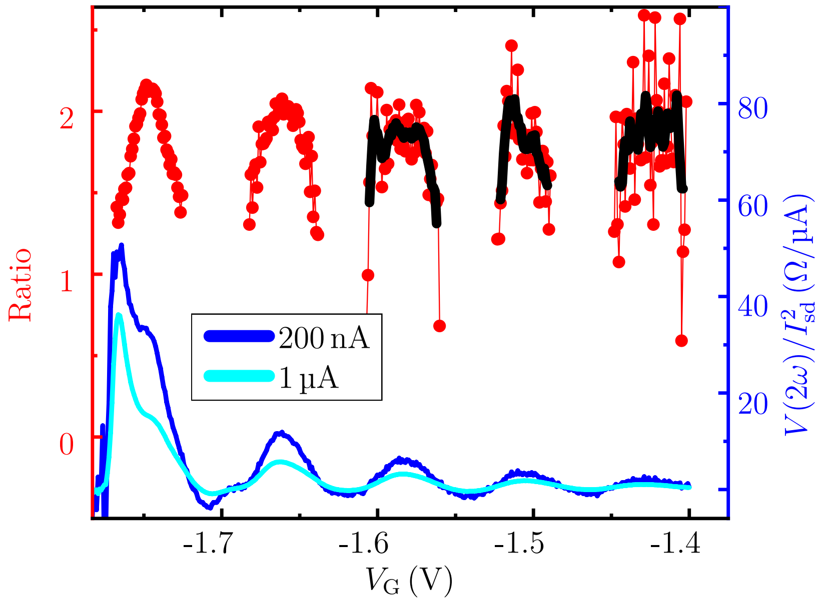

Figure 6.4: Non-local spin-to-charge signal $V(2\omega)/I_{\mathrm{sd}}^2$ for 200 nA (blue) and 1 µA (cyan) as well as the ratio of the blue and cyan curve (red). Between all five subband transitions, the ratio of the measured signal does not change. The black curves are a moving average of the data to guide the eye.

standard model of spin injection, the spin accumulation generated at a given spin injection contact diffuses into all directions and decays exponentially with a distance. Assuming the validity of the model in our devices, $V(2\omega)$, measured using various spin injecting contacts, is expected to decay exponentially with a distance, $V(2\omega) \propto exp(-d/L_s)$, where L_s is the spin diffusion length.

Figure 6.6 shows the peak values of $V(2\omega)/I_{\mathrm{sd}}^2$ at the transitions between subbands. The measurements were done for various distances d between the spin injection contacts and the constriction. During the experiment, the split-gate voltage V_{G} was swept and $V(2\omega)$ was measured non-locally. This procedure was repeated for various excitation currents $I_{\mathrm{sd}} \in [200, 300, ..., 900\,\mathrm{nA}]$. The graph shows the average of the peak values in $V(2\omega)/I_{\mathrm{sd}}^2$, observed at the transitions between subbands. Distances between the spin injection region and the QPC include 10 µm (black), 13 µm (red) and 16 µm (blue). In contrast to the expected exponential decay, $V(2\omega)/I_{\mathrm{sd}}^2$ increases as d is increased.

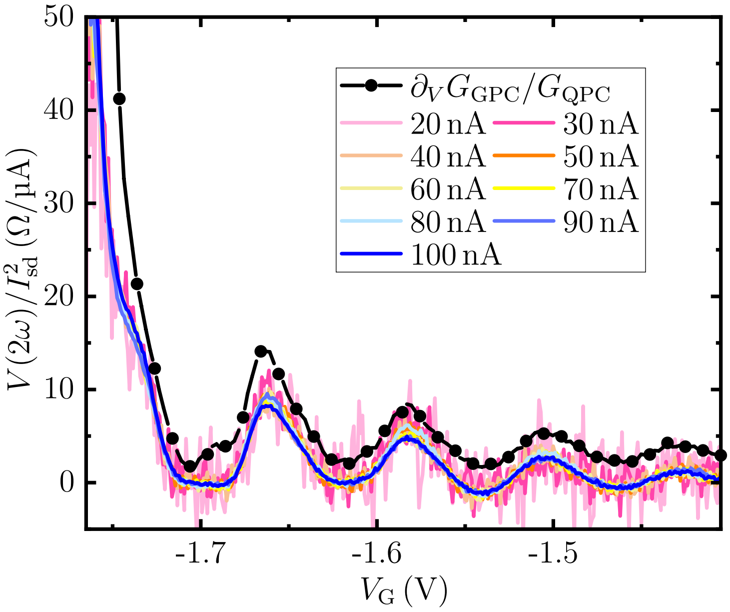

Figure 6.5: Continuation of the non-local spin-to-charge conversion experiment. The black line represents the transconductance weighted by the conductance of the QPC $\partial_V G_{QPC}/G_{QPC}$. The colored curves show the voltage drop across the QPC $V(2\omega)/I_{sd}^2$ weighted by the square of excitation currents for various I_{sd}. For all currents used here, the data collapse onto a single curve and follow the weighted transconductance well.

The measured signal[2] appears to be correlated with the geometry of the spin contacts. More precisely, it appears that $V(2\omega)/I_{sd}^2$ increases as the width of a spin contact is decreased as the curve with the lowest peak heights was measured using a spin contact, which is $w = 1\,\mu m$ wide (black curve) and the red curve corresponds to $w = 700\,nm$ and blue curve, which exhibits the largest peak signal heights, corresponds to $w = 500\,nm$. The spin contacts in a spin-injection device are commonly fabricated with various widths to facilitate unambiguous magnetic switching, required for spin valve measurements. The difference in the induced strain relaxation results in different coercive fields

---

[2] From a chronological perspective, these measurements presented here were the first non-local spin-to-charge conversion measurements conducted for this thesis. It also has to be mentioned that the measurements shown in figure 6.6 were conducted on a different wafer than all other samples in this work, however with the same heterostructure layout. Although spin valve measurements showed similar results, indicating proper spin transport features, it has to be noted that the mobility of this wafer was lower compared to the wafer used for the remaining experiments. The consequence was not in spin transport, but rather in the results of QPC measurements. The decreased mobility led to less clear plateaus and blurred transitions, resulting in lower transconductance values.

[96], which in turn leads to a clear spin valve pattern. However, changing the width of a spin contact seems to affect more than just the coercive field, which complicates the demonstration of a spin origin of $V(2\omega)$.

By fabricating a device for which all spin contacts have identical geometry, it may be possible to bypass this complication. Consequently, such a device was prepared. In figure 6.7 the corresponding sample is shown schematically on the left side, while on the right side of the figure a SEM picture of the sample is shown. The mesa is 20 µm wide and all spin contacts have the same width of $w = 1$ µm, while the distance between individual spin contacts is 3 µm. The geometric parameters have been chosen in order to maximize the spin accumulation at the constriction, which is achieved by keeping the distance between the spin contacts and the QPC to a minimum while still allowing for the fabrication of clean samples with well-defined structures. The lowest spatial separation between a spin contact and the QPC is 6.5 µm.

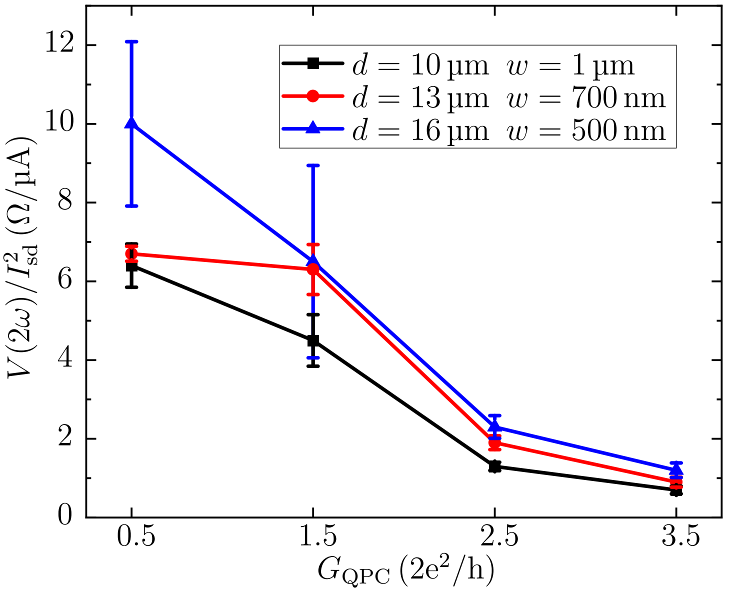

Figure 6.6: Results of distance-resolved non-local spin-to-charge conversion measurements. The gate voltage was swept and $V(2\omega)$ measured for various excitation currents $I_{\mathrm{sd}} \in [200, 300, ..., 900\,\mathrm{nA}]$. Shown here are the average values of $V(2\omega)/I_{\mathrm{sd}}^2$ at maximum transconductance between subbands. The measurement was conducted for three different spin contacts. Opposed to the expectation that the measured signal decreases with increased distance d between the spin contact and the QPC, it is observed that the measured signal scales with the with w of the spin contact. The error bars indicate the standard deviation.

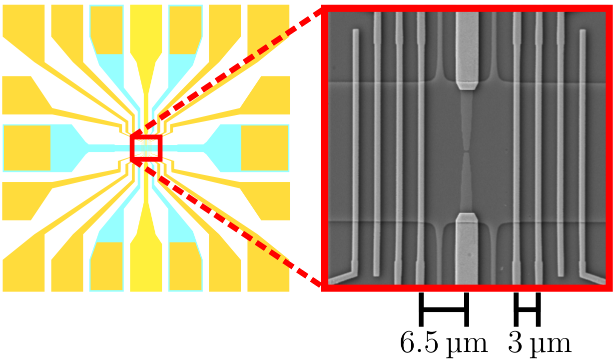

Figure 6.7: Schematic representation of the sample (left) and a SEM picture of the sample (right). All spin contacts have the same width $w = 1\,\mu\text{m}$. In the center of the sample is a QPC. The smallest distance between the QPC and a spin contact is 6.5 µm.

The results of the non-local spin-to-charge conversion measurements shown in figure 6.8 were conducted on a device with the geometry presented in figure 6.7. The measurements were performed on various spin contacts with a distance of 6.5 µm (orange), 9.5 µm (red), 12.5 µm (dark red) and 15.5 µm (light red) from the QPC, using an excitation current of $I_{\text{sd}} = 600\,\text{nA}$. For all distances, the data follows both the transconductace and the inverse conductance of the constriction. For the last subband transition, i.e., at $G_1 \to G_0$, the volt-

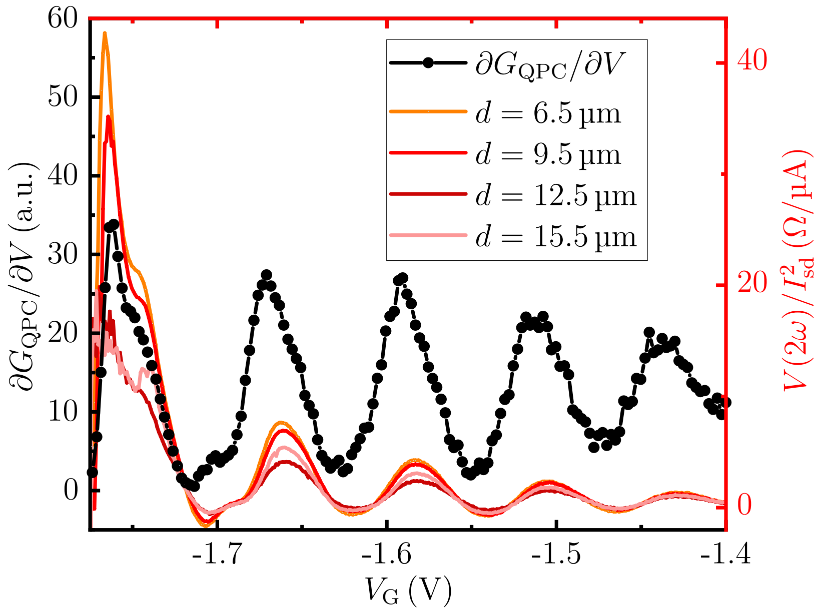

Figure 6.8: Transconductance (black) of a QPC and the non-local voltage drop across a QPC, $V(2\omega)/I_{\text{sd}}^2$, normalized by the square of excitation current (various shades of red). The measurements were conducted at $I_{\text{sd}} = 600\,\text{nA}$ for various spin contacts. While all spin contacts are of the same geometry, they differ in the distance d from the QPC.

age drops measured for spin contacts located at $d = 12.5\,\mu\mathrm{m}$ and $d = 15.5\,\mu\mathrm{m}$ show lower values than expected from the $1/G_{\mathrm{QPC}}$ dependence. In addition, one finds that the measured voltage $V(2\omega)$ is greater for $d = 15.5\,\mu\mathrm{m}$ compared to $d = 12.5\,\mu\mathrm{m}$. This suggests that although all spin contacts are nominally the same, small deviations among individual spin contacts may influence the measurements. Aside from this anomally, one finds that $V(2\omega)/I_{\mathrm{sd}}^2$ is largest for the spin contact with the lowest spatial separation from the QPC with $d = 6.5\,\mu\mathrm{m}$. In general, $V(2\omega)/I_{\mathrm{sd}}^2$ decreases as d is increased.

As previously stated, a spin accumulation decays exponentially with a distance d from the spin contact. The characteristic length scale for this exponential decay is the spin diffusion length L_s. If $V(2\omega)$ is spin-related, one expects that the measured voltage drop across the constriction

$$V(2\omega, d)_{\mathrm{spin}} = V_{\mathrm{spin},0}\, e^{(-2d/L_s)} \tag{6.13}$$

also decays exponentially with a distance, where $V_{\mathrm{spin},0}$ is the signal one would obtain for $d = 0$. The factor 2 in the exponent comes from the fact that for nonlinear spin-to-charge conversion, the signal is quadratic in the spin accumulation.

To study the distance dependence for many subbands, $V(2\omega)$ must be corrected by the transconductance, see equation 6.4. Figure 6.9 shows the value of the non-local voltage drop at the transition between subbands, $V(2\omega)\cdot G/\partial_V G$, normalized by the weighted transconductance as a function of distance d. The data is presented for five conductance risers, i.e., at the first five subband transitions, $G_{\mathrm{N}} \rightarrow G_{\mathrm{N}+1}$, including $\mathrm{N} \in [0, 1, ..., 4]$. The data for $d = 12.5\,\mu\mathrm{m}$ from figure 6.8 was omitted for figure 6.9. It has to be noted that $\partial_V G_{\mathrm{QPC}}/G_{\mathrm{QPC}}$ is different for each subband. Consequently, each subband has to be evaluated seperately. Instead of an exponential decay, all five curves seem to exhibit a linear slope. For a spatial separation of $\Delta d = 3\,\mu\mathrm{m}$ between individual spin contacts, the spin accumulation should exhibit sufficient variation to display an exponential decay, see figure 5.4. This is due to the fact that for the wafers used in this work, the spin diffusion length is $L_s = 7.2\,\mu\mathrm{m}$. From distance resolved measurements it is therefore not possible to prove whether the second harmonic of the voltage drop across the QPC originates in spin.

Suppressing the Spin Accumulation with a Perpendicular Magnetic Field

In another try of checking whether $V(2\omega)$ arises from the presence of a spin accumulation, measurements in a magnetic field $B_z = B$ perpendicular to the spin accumulation were performed. When a perpendicular magnetic field is ap-

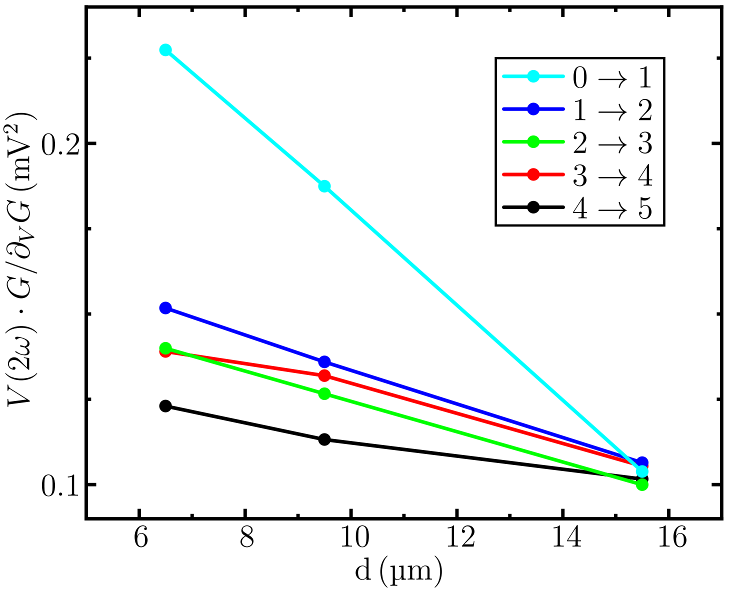

Figure 6.9: Non-local voltage drop $V(2\omega)$ measured across a QPC at various subband transitions, normalized by the weighted transconductance $\partial_V G_{\mathrm{QPC}}/G_{\mathrm{QPC}}$ as a function of distance. $\partial_V G_{\mathrm{QPC}}/G_{\mathrm{QPC}}$ has to be evaluated separately for each subband. Shown are the first five risers in the conductance. All curves exhibit a linear slope.

plied, it dephases the in-plane spin accumulation, suppressing the spin-related signal. The procedure is reminiscent of the Hanle measurements, mentioned in section 5.1. The utilization of a large perpendicular magnetic field to suppress the spin-related signal in a QPC has been demonstrated in reference [135]. Compared to the samples used in our work, however, the generation of the spin accumulation did not rely on ferromagnetic spin contacts but rather on the spin Hall effect. In addition, the strong spin-orbit coupling in their GaAs hole gas demanded large magnetic fields to suppress the spin accumulation. In our samples, however, large magnetic fields can cause an undesired change in the magnetization configuration of the spin contacts. A second problem that may arise from employing large out-of-plane magnetic fields is a modification of the QPC properties. Specifically, the step quality may be enhanced, resulting in higher peak transconductance values. This could complicate the evaluation of the data, as $V(2\omega)$ is linear in the transconductance. Consequently, low perpendicular magnetic fields are advantageous for the devices used in this work. In section 5.1, the Hanle measurement presented in figure 5.5 shows that for the heterostructure used in this work $B = 150\,\mathrm{mT}$

is required to fully dephase the spin accumulation. At $B = 50\,\mathrm{mT}$, however, most of the spin signal was suppressed, while the QPC characteristics remain unaltered, see figure 5.12. Consequently, $B = 50\,\mathrm{mT}$ is the perpendicular magnetic field strength chosen for the following experiments.

Before applying an out-of-plane magnetic field, the magnets of the spin Esaki diode were magnetized by a strong in-plane magnetic field $B = 1\,\mathrm{T}$ aligned with the easy axis of the spin contacts. Before rotating the sample into an out-of-plane configuration, the magnetic field was swept to zero with a low sweeping rate. Approaching $B = 0$ with a large sweeping rate could cause the magnetic field to pass through zero field, potentially affecting the magnetic orientation of the spin contacts. One approach for the measurements in a magnetic field, which has been used succesfully before [134, 135], is to apply a fixed split-gate voltage V_G and sweep the field. This method, however, resulted in measurements with a low signal-to-noise ratio for our samples. A different possibility is to fix the magnetic field and sweep V_G, which is the approach chosen in this work.

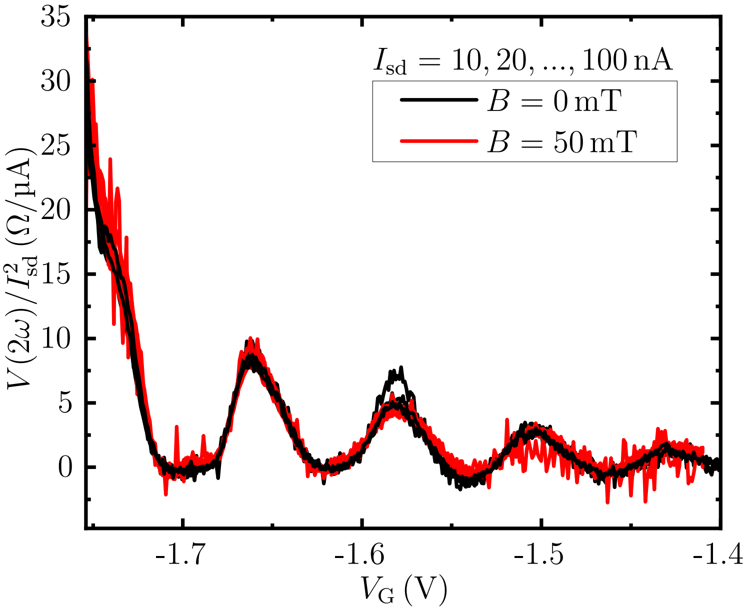

Figure 6.10: Results of non-local spin-to-charge conversion experiments in zero applied magnetic field (black) and in an out-of-plane magnetic field of $B = 50\,\mathrm{mT}$ (red). The measurement was repeated for different currents $I_\mathrm{sd} \in [10, 20, ..., 100\,\mathrm{nA}]$. The out-of-plane magnetic field is used to dephase a spin accumulation $\delta\mu_s \rightarrow 0$ at the QPC. There is, however, no visible difference between the red and black curves. Before the measurement was started, the spin contacts were magnetized by a strong in-plane magnetic field.

The non-local voltage drop $V(2\omega)/I_{\mathrm{sd}}^2$, normalized by the excitation current, is shown in figure 6.10 for zero applied magnetic field (black curves) and for $B = 50\,\mathrm{mT}$ (red). Measurements were conducted for different currents $I_{\mathrm{sd}} \in [10, 20, ..., 100\,\mathrm{nA}]$. Unfortunately, there is no clear difference between $B = 0$ and $B = 50\,\mathrm{mT}$. For certain current densities in figure 6.10 the red curve falls below the black curve. These results, however, cannot be reproduced. When the measurements were repeated, the curves showed no difference or showed even the opposite behavior, with $B = 50\,\mathrm{mT}$ producing higher peak values in $V(2\omega)$. These results suggest that any differences between zero magnetic field and $B = 50\,\mathrm{mT}$ are due to fluctuations in the measurement rather than being spin related.

Discussion

The absence of any influence of an out-of-plane magnetic field on $V(2\omega)$ suggests that we cannot verify the existence of a spin accumulation in our devices via nonlinear spin-to-charge conversion. Based on the data presented in figure 6.10, it may even be inferred that no spin accumulation is present in our samples. Section 5.1, however, demonstrated the presence of a spin accumulation in our devices using the non-local spin valve method, which exhibited clear switching behavior. Distance-resolved spin valve measurements revealed a high spin injection efficiency and spin diffusion length. Additionally, Hanle measurements were conducted, demonstrating that an out-of-plane magnetic field of $50\,\mathrm{mT}$ can effectively suppress a significant portion of the spin signal. This highlights the importance of being able to confirm the presence of spin accumulation through well-established alternative methods. However, if $V(2\omega)$ is not spin-related, the question of the origin of $V(2\omega)$ arises.

It is possible that thermopower, which is also measured as the second harmonic voltage drop across a QPC [140], has a major contribution to $V(2\omega)$. This may provide an explanation for the unexpected increase of $V(2\omega)$ with a distance d between the spin contact and the QPC in figure 6.6, where it was observed that $V(2\omega)$ increases as the width of the spin contacts decreases. The width of the spin contacts affects the voltage drop across the spin contacts, which is larger for smaller width w due to the decrease in surface area. A consequence of the large voltage drop, which is required to drive an excitation current through a spin contact (or reference contact), is local heating of electrons in the transport channel. Heat is then conducted efficiently in the high mobility 2DEG, which results in a temperature gradient across the QPC as $T_1 - T_2 = \Delta T$. This temperature gradient results in a thermopower signal, which is measured as the second harmonic voltage drop $V(2\omega)$ across the QPC. The I-V curves of spin contacts with $w = 300\,\mathrm{nm}$ (light blue) and

$w = 700\,\text{nm}$ (blue) displayed in figure 6.11 show that the three-terminal voltage $V_{3\text{T}}$, which drops across the spin Esaki diode, indeed changes significantly with the contact width. The inset shows the measured data in the range of $I \in [-25\,\mu\text{A}, 25\,\mu\text{A}]$. These results suggest that thermopower (TP) may play a significant role in the samples used in this work. The non-local voltage drop across the QPC may be a supperposition $V(2\omega) = V(2\omega)_{\text{spin}} + V(2\omega)_{\text{TP}}$ of a signal originating in spin and in thermopower. If the width of a spin contact is altered, the voltage drop over the spin Esaki diode changes, which in turn affects the dissipated power at a given current. As a consequence, a wide spin contact located close to the QPC may exhibit a large $V(2\omega)_{\text{spin}}$ and a small $V(2\omega)_{\text{TP}}$. In contrast, a narrow spin contact located further away from the constriction may show a decreased $V(2\omega)_{\text{spin}}$ and an increased $V(2\omega)_{\text{TP}}$ compared to the close contact. The fact that $V(2\omega)$ in figure 6.6 increases as the distance between the spin contacts is increased may be attributed to a larger increase in thermopower compared to the decrease in spin-related signal.

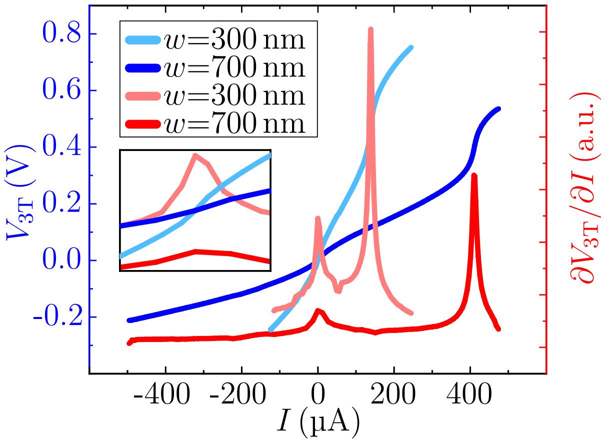

Figure 6.11: I-V curve of two spin contacs, displaying the voltage drop over the spin Esaki diode $V_{3\text{T}}$ (blue) and the differential conductance $\partial V_{3\text{T}}/\partial I$ (red) as a funktion of applied current I. The contacts are 700 nm (dark blue, dark red) and 300 nm (light blue, light red) wide, respectively. The inset shows the measurement over the range of $I \in [-25\,\mu\text{A}, 25\,\mu\text{A}]$

There is an additional factor which may indicate that $V(2\omega)$ originates in thermopower. This additional factor is an observed linear relation between $V(2\omega)$ and d in figure 6.9, which may result from the heat transport properties in our 2DEG, where heat is also expected to decay exponentially with a distance from the QPC, where the characteristic length scale is called the thermal decay length. In our samples, the thermal decay length should exceed the spin diffusion length by about one order of magnitude [146], i.e., the thermal decay length is much larger than the distances in figure 6.9. Consequently, one can approximate

$$V(2\omega) \approx V^0_{\text{TP}}(1 - \frac{d}{L_{\text{TP}}}) \tag{6.14}$$

a linear relation between the voltage drop accross the QPC and the distance

d, in the case that d is small compared to the thermal decay length. The linearity between d and $V(2\omega)$ is, in fact, observed in figure 6.9 for all measured subband transitions, which may be attributed to a large contribution of thermopower for $V(2\omega)$.

Figure 6.9 may provide additional information about the origin of $V(2\omega)$, as the cyan curve, which shows the data for the first subband transition $G_0 \rightarrow G_1$, exhibits distinct behavior from the other curves. A QPC can be used as a thermometer[3], to measure thermopower or to measure heat transport [140]. This is achieved by measuring $V(2\omega)$ at the transition between subbands. Due to unknown reasons, this procedure cannot be applied for quantitative analysis at the first subband transition, where $V(2\omega)_{\mathrm{TP}}$ exhibits abnormal values, which changes the exact evaluation of thermopower. The curves shown in figure 6.9 fall onto a similar trace for $1 \rightarrow 2$, $2 \rightarrow 3$, $3 \rightarrow 4$. While the slope of the curve for the transition from $4 \rightarrow 5$ is similar to the one for the aforementioned curves, the slope for the normalized voltage drop $V(2\omega) \cdot G/\partial_V G$ for the first subband exhibits different behavior from the rest. A quantitative difference in behavior for the first subband is consistent with literature on thermopower [140].

Decreasing the Influence of Thermopower

One way to conduct further investigation would be to repeat the measurement series using a device that has more spin contacts to generate additional data points. However, the fabrication of these devices is subject to certain limitations. Decreasing the distance between individual spin contacts is challenging due to lithographic limitations. Additionally, the distance d between a spin contact and the QPC cannot be chosen arbitrarily large due to the decay of the spin accumulation with increasing d.

A second approach to conduct further investigation is to decrease the generated thermopower by fabricating a sample with wider spin contacts. This way, the voltage drop across the spin injection contact's tunnel barrier, which is a prerequisite for efficient spin injection [47], is reduced. The consequence is decreased heating of the transport channel and, thus, decreased thermopower. Upon widening the ferromagnetic spin contacts, however, one needs to be careful that the magnetic properties are unaffected as it is important to maintain a well-defined magnetic anisotropy axis to enable magnetic switching. This anisotropy axis, which results from induced strain relaxation, can be talored by lithographic means (see chapter 4). The change in magnetic anisotropy

---

[3] If a QPC is to be used as a thermometer, a second QPC has to be utilized as a reference point for measurements.

from induced strain relaxation, however, is only present at the edge of a spin contact [96]. For this reason, spin contacts must be fabricated with a large aspect ratio and cannot be arbitrarily large. For a spin contact with $w = 2\,\mu\text{m}$, however, spin valve measurements showed well-defined magnetic switching. Consequently, devices with $w = 2\,\mu\text{m}$ wide spin contacts were fabricated. Figure 6.12 displays a SEM of such a device. In the center of the device is a spin contact with $w = 2\,\mu\text{m}$. With a spatial separation of $6.5\,\mu\text{m}$ a QPC is placed on either side of the spin contact. Further away from the center are additional spin contacts with standard geometry, enabling spin valve measurements.

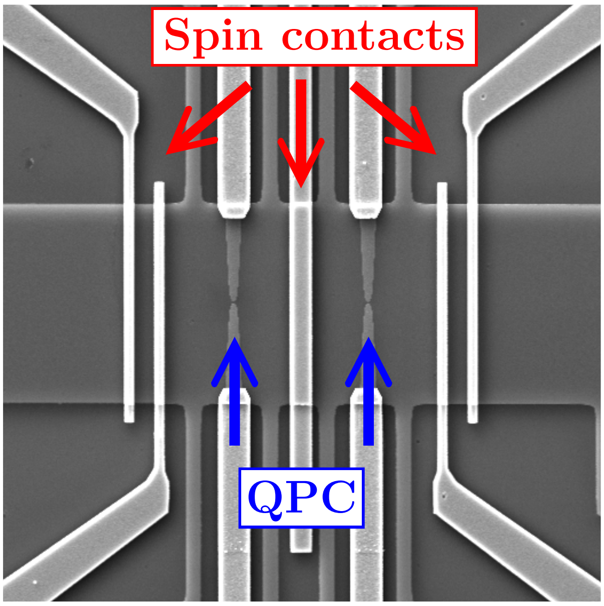

Figure 6.12: Device with a large spin contact of width $w = 2\,\mu\text{m}$ in the center. The widening of the contact area reduces contact resistance, thereby limiting heat generation. $6.5\,\mu\text{m}$ to the left and to the right of the spin contact, a QPC is placed. Additional spin contacts enable spin valve measurements.

Non-local spin-to-charge conversion measurements of a sample containing a spin contact with $w = 2\,\mu\text{m}$ are shown in figure 6.13. The left axis shows the measured raw data in units of µV while the right axis shows the data normalized by the square of applied source drain current $V(2\omega)/I_{\text{sd}}^2$. An excitation current of $I_{\text{sd}} = 2\,\mu\text{A}$ was chosen. Similar to previous samples, an out-of-plane magnetic field was used to suppress a spin accumulation. Prior to the measurement, the spin contacts were magnetized with a strong in-plane magnetic field. At fixed magnetic fields $B \in [0, 2.5, ..., 75\,\text{mT}]$, the split-gate voltage V_{G} was swept. Figure 6.13 (a) shows the data over the full measurement range whereas 6.13 (b) displays the inset, zooming in on the last transconductance step. The curves are color coded with respect to the applied magnetic field. For $B = 0$, the measurement data is displayed in red. At increasing magnetic fields, the color changes from red to purple to blue.

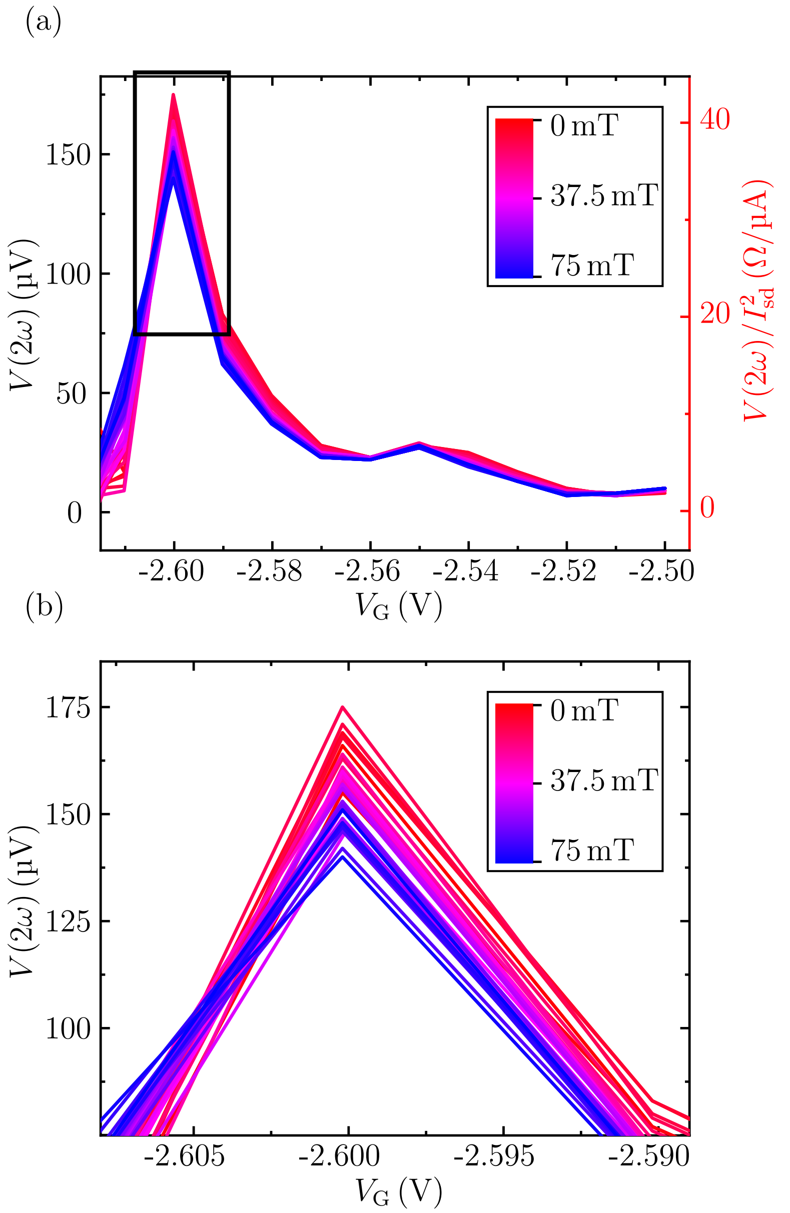

Figure 6.13: (a) Non-local spin-to-charge conversion measurements of a spin contact with $w = 2\,\mu\mathrm{m}$ for various out-of-plane magnetic fields. Prior to measurement, the spin contacts were magnetized in-plane. One observes the trend that with increasing magnetic field (red → purple → blue) from $B = 0$ to $B = 75\,\mathrm{mT}$ the measured signal decreases. Part (b) shows the inset from a, zooming in on the graph.

For increasing magnetic fields, $V(2\omega)$ decreases to smaller values. This decrease has to be viewed as a general trend. If the data between individual magnetic fields is compared directly, the measured data may contradict the expected behavior. For $B = 10\,\mathrm{mT}$ the measured voltage drop across the con-

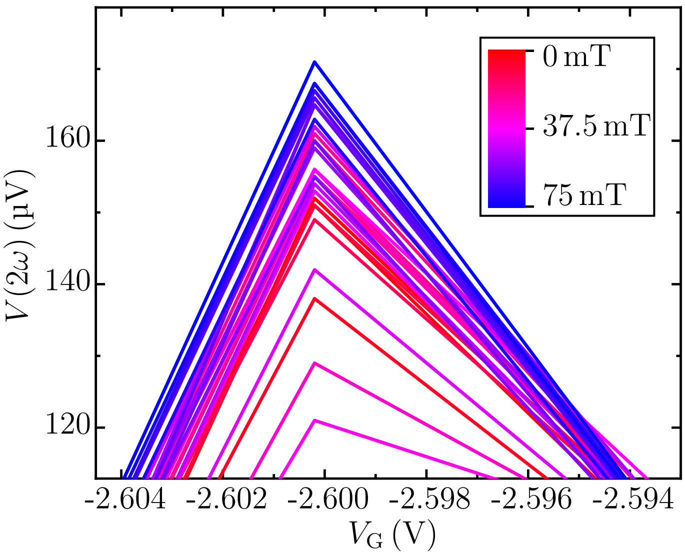

Figure 6.14: Repeat of the measurement as presented in figure 6.13. The results from the previous measurements could not be repeated. Instead, the measurements here suggest that an out-of-plane magnetic field increases $V(2\omega)$. The fact that some curves are scattered to different values suggest that not a magnetic field but fluctuations in the measurement are responsible for variations in the obtained data.

striction is larger than for $B = 0$. Although the magnetic field causes a shift of $V(2\omega)$ towards smaller values, it appears that multiple measurements are necessary to obtain unambiguous results due to the large fluctuation of $V(2\omega)$ at the last conductance riser. For this reason, the measurement procedure was repeated immeadiately after the measurement finished. The result of the reiteration is shown in figure 6.14. For this measurement series, the drop in $V(2\omega)$ with increasing magnetic field cannot be seen. In fact, the curves of the figure would suggest an increase of signal with magnetic field strength, which opposes the results from the previous measurements.

Figures 6.13 and 6.14 show different behavior in $V(2\omega)$ with respect to a perpendicular magnetic field. In the first measurement series, $V(2\omega)$ decreased with B, whereas the second measurement series showed an increase with B. The measurements from figures 6.13 and 6.14, however, share the fact that the obtained data is subject to large fluctuations. This suggests that the reason for the magnetic field dependence observed in figure 6.13 is due to fluctuations in the measurement rather than spin related phenomena. With the geometry presented in figure 6.12, where a spin contact with a large contact with $w = 2\,\mu\text{m}$ was used for spin injection, it is still not possible to prove spin origin of $V(2\omega)$ and it appears that thermopower (or other effects) play a significant role in the generation of $V(2\omega)$. One approach to further reduce any influence of thermopower, which appears to be the result of generated heat from the spin contacts, would be to fabricate a device with very large spin contacts, which have a width of, say, $w = 20\,\mu\text{m}$. Note that in this case, the magnetic anisotropy axis is not perpendicular to the flow of electrons in the mesa[4]. It is, however, possible that even in a device containing an idealized spin Esaki diode, which has very low tunneling resistance, the heat generation by the current flow through the 2DEG is large enough to obscure a spin related signal. This gives rise to the question of whether it is possible to verify the existence of a spin accumulation in our devices with nonlinear spin-charge conversion assuming the spin accumulation behaves according to the standard model of spin injection. As a next step, the spin-related signal across the QPC is calculated.

Calculation of the Spin-Related Voltage Drop across the QPC

One advantage of the devices used in this work is that by means of the spin valve method, an independent path to accessing information on the spin accumulation, $\delta\mu_s$, and spin transport properties is available. If a clear spin-related component of $V(2\omega)$ was observed in the measurement data, then comparing these results to the data obtained from spin valve measurements would enable verification of the obtained values for $\delta\mu_s$. Unfortunately, the standard experimental checks did not confirm the presence of the spin-related signal in the measured voltage. Instead, the reverse approach will now be used, where $\delta\mu_s$ obtained from spin valve measurements is utilized to calculate the expected value of $V(2\omega)_{\text{spin}}$ in a nonlinear spin-to-charge conversion experiment.

The first step is to calculate the value of $\delta\mu_s$ based on spin valve measurements. A spin accumulation is defined as a splitting in the quasichemical potential between spin-up $\mu_\uparrow$ and spin-down $\mu_\downarrow$ electrons (see section 2.2). Therefore, the quasichemical potential profile of a spin valve measurement, which is shown in figure 5.2, is crucial for the calculation of $\delta\mu_s$. When the spin contacts switch from a parallel to an antiparallel configuration, the non-local voltage resulting from the emf changes. The difference in the measured non-local voltage is linear in the spin accumulation at the detector site. In fact, one finds that $\Delta V_{\text{NL}} = V_{\text{NL},\uparrow} - V_{\text{NL},\downarrow} \propto \mu_\uparrow - \mu_\downarrow = 2\delta\mu_s(d)$. To determine the exact value of $\delta\mu_s$, however, it is necessary to use multiple injector-detector pairs to conduct distance-resolved spin valve measurements.

From distance-resolved spin valve experiments, spin transport parame-

---

[4] One could, of course, change the orientation of the mesa.

ters can be extracted. As spin transport has a diffusive character, the spin accumulation decays exponentially with a distance d from spin injection as $\delta\mu_s(d) = \delta\mu_s(0)\exp(-d/L_s)$. Here, L_s is the spin diffusion length and $\delta\mu_s(0)$ is the spin accumulation at the spin injection contact. Figure 5.4 shows ΔV_{NL} on a semi-logarithmic scale over d. One finds that ΔV_{NL} is related to the spin injection efficiency P and source-drain current I by the expression [38]

$$\Delta V_{\mathrm{NL}} = \frac{P^2 I R_s L_s}{2w_c}\exp\left(-\frac{d}{L_s}\right), \tag{6.15}$$

where R_s and w_c are the sheet resistance and width of the spin contacts, respectively. ΔV_{NL} was not measured at $d = 6.5\,\mu\mathrm{m}$. However, the fit shown in figure 5.4 results in $\Delta V_{\mathrm{NL}}(6.5\,\mu\mathrm{m}) = 3.0\,\mu\mathrm{V}$ and $P = 56\,\%$ at $I = 2\,\mu\mathrm{A}$. To obtain equation 6.15 one assumes that P is equal for spin injection and detection. From this, the relation between ΔV_{NL} and $\delta\mu_s$ follows as

$$\delta\mu_s = \frac{\mathrm{e}\,\Delta V_{\mathrm{NL}}}{2P}, \tag{6.16}$$

which results in $\delta\mu_s(6.5\,\mu\mathrm{m}, 2\,\mu\mathrm{A}) = 2.7\,\mu\mathrm{eV}$.

Now the expected voltage drop across a QPC which is caused by a spin accumulation can be calculated. At the last conductance riser, at $G_{\mathrm{QPC}} = \mathrm{e}^2/\mathrm{h}$, equation 6.4 becomes [135]

$$V(2\omega) = -\frac{1}{2}\frac{\pi}{\mathrm{e}\hbar\omega_x}\delta\mu_s^2, \tag{6.17}$$

where $\hbar\omega_x = 1.84\,\mathrm{meV}$ was calculated in section 5.2. Inserting the values into equation 6.17 shows that $V(2\omega) = 6.2\,\mathrm{nV}$ is very low compared to the measured values of $V(2\omega) \sim 150\,\mu\mathrm{V}$ obtained from measurements. Based on the values presented here, it is very difficult to measure nonlinear spin-to-charge conversion in the samples presented in this work.

Now the question arises whether the expected signal could be larger in an idealized sample. This idealized sample considers the maximum value for $\delta\mu_s$ that is possible to obtain in our devices from a theoretical point of view. In this case, it is assumed that the spin accumulation reaches the QPC without any loss in magnitude: $\delta\mu_s = \delta\mu_s(0)$. From a mathematical point of view, this means that the distance between the spin contact and the QPC is zero, which is not possible in a real device. If, however, the spatial separation between the spin contact and the QPC is smaller than the mean free path, electron transport and, thus, spin transport is ballistic. In this case, spin relaxation is suppressed and one can use $\Delta V_{\mathrm{NL}}(d \to 0) = 7.5\,\mu\mathrm{V}$ to calculate $\delta\mu_s$ at the constriction. In addition to loss-free spin transport, a spin injection efficiency of $P = 100\,\%$ is assumed. In this case, one obtains $\Delta V_{\mathrm{NL},100\%} \to \Delta V_{\mathrm{NL}}/(0.56)^2 = 23.8\,\mu\mathrm{V}$ at $I = 2\,\mu\mathrm{A}$ [5]. In this case, the spin accumulation amounts to $\delta\mu_s = 11.9\,\mu\mathrm{eV}$, which is considerably larger than the value obtained from spin valve measurements in this work. Inserting this value into equation 6.17 and using $P = 100\,\%$ results in $V(2\omega) = 120\,\mathrm{nV}$. This leads to a large increase in the spin related signal compared to the values obtained from the previous calculations. As $V(2\omega) \propto \delta\mu_s^2$, increasing the spin accumulation greatly changes the measured signal. However, the gedankenexperiment of using a perfect, idealized device still produces values, which are orders of magnitude below the signals obtained from measurements in this work.

In summary, the spin-related origin of $V(2\omega)$ could not be confirmed. There are, however, some experimental obvervations which point towards thermopower does playing a significant role in the devices used in this work. There are several ways to decrease the amount of generated thermopower beyond those previously discussed. One option is to further increase the width of the mesa. Another approach is to choose a material with a different heat capacity c_v, which is given by [140]

$$c_v = \frac{\pi^2}{3}\frac{k_\mathrm{B}T}{E_\mathrm{F}} n_\mathrm{s}\, k_\mathrm{B} \tag{6.18}$$

where T, n_s, k_B and E_F are the temperature, sheet carrier density, Boltzmann constant and Fermi energy, respectively. The electron density, however, is in the range typical for GaAs/AlGaAs heterostructures. Increasing the temperature by a few Kelvin would most likely destroy the observed quantized conductance of the QPC due to temperature smearing.

Considering the various measurements presented in this section as well as the calculations presented, it appears that measuring a spin accumulation with a QPC by means of nonlinear spin-to-charge conversion is very problematic with the devices used in this work. In order to utilize nonlinear spin-to-charge conversion, it appears necessary to reduce the influence of any components in $V(2\omega)$ which are not spin related. In addition, a larger spin accumulation would be required to increase the spin-related component of $V(2\omega)$, which may be achieved by other means than all-electrical spin injection through a spin Esaki diode.

---

[5] In comparison, Marcellina *et al.*, who measured nonlinear spin-to-charge conversion in a GaAs hole gas obtained $\delta\mu_s = 1\,\mu\mathrm{eV}$ at $I = 5\,\mathrm{nA}$ utilizing the spin Hall effect [135].

6.2.3 Linear Spin-to-Charge Conversion

This section presents the findings of linear spin-to-charge conversion experiments. Here, the voltage drop, $V(\omega)$, measured across the QPC, is linear in the spin accumulation $\delta\mu_s$ and linear in a magnetic field B, which is (anti)parallel to the spin accumulation. In contrast to nonlinear spin-to-charge conversion, the first harmonic of the voltage drop across the QPC is measured, so the measurements should not be affected by thermopower.

While the measurement setup for measuring spin-to-charge conversion in the linear regime also followed the scheme from figure 6.2, the measurements presented in this section were conducted in a dilution fridge at a temperature of 85 mK. The voltage drop $V(\omega)$ across the QPC was measured while applying a non-local excitation current I_{sd} on its left side and leaving the right side as a floating probe. During measurement, the split-gate voltage V_{G} was swept at a given in-plane magnetic field.

If a spin accumulation $\delta\mu_1 = \delta\mu_s$ is present on the left side of the QPC with no spin accumulation on the right side $\delta\mu_2 = 0$, the measured voltage drop over the constriction reads

$$V(\omega) = \frac{G_3 \delta\mu_s}{\mathrm{e}(G_1 + G_4 \delta\mu_s)}, \tag{6.19}$$

with G_1, G_3 and G_4 given by equations 6.3a, 6.3c and 6.3d, respectively. Experimentally, $\delta\mu_2 = 0$ can be achieved by creating a narrow constriction with a QPC conductance of $G \leq 2\mathrm{e}^2/\mathrm{h}$. By inserting equation 6.5 into equation 6.3c, one finds that G_3 follows the transconductance $\partial G_{\mathrm{QPC}}/\partial V_{\mathrm{G}}$ of the QPC, i.e., G_3 is expected to follow the shape of a δ-function with respect to the applied split-gate voltage. At the first conductance step, where the transconductance is at its maximum (i.e., at $G = \mathrm{e}^2/\mathrm{h}$), G_4 equals zero. In this case, equation 6.19 simplifies to $V(\omega) = (G_3\,\mathrm{h}/\mathrm{e}^2) \cdot \delta\mu_s$.

The voltage drop $V(\omega)$ measured over the QPC is expected to be linear in the spin accumulation. Therefore, $V(\omega)$ is also linear in the excitation current I_{sd}. The curves in figure 6.15 show the measured voltage drop $V(\omega)$ at zero magnetic field for various excitation currents. The applied currents are $I_{\mathrm{sd}} = 20\,\mathrm{nA}$ (black curve), $I_{\mathrm{sd}} = 40\,\mathrm{nA}$ (red), $I_{\mathrm{sd}} = 60\,\mathrm{nA}$ (green) and $I_{\mathrm{sd}} = 80\,\mathrm{nA}$ (blue). Even without quantitative analysis it seems that the expected linear relation between $V(\omega)$ and I_{sd} holds. Figure 6.15 also illustrates one technical advantage of linear spin-to-charge conversion opposed to employing nonlinear methods. Even if the excitation current is increased by a factor of four, the measured data can still be plotted in one graph. In the case of nonlinear spin-to-charge conversion, the increase in the measured signal would be 16-fold. However, the challenge is not in visualizing the data but rather in the need

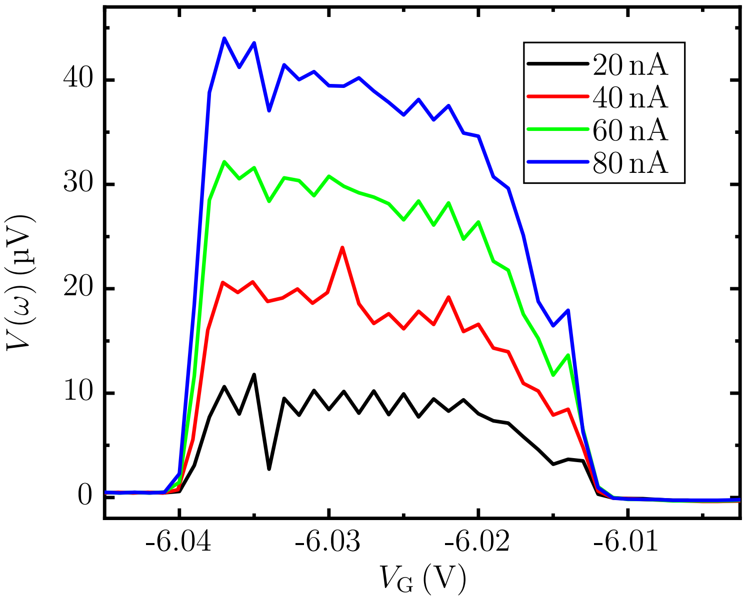

Figure 6.15: Voltage drop $V(\omega)$ over the QPC at $B = 0$ for various excitation currents I_{sd}. It appears that $V(\omega)$ increases linearly as I_{sd} is increased from 20 nA (black) to 40 nA (red), 60 nA (green) and 80 nA (blue).

to adjust the working range of the measuring multimeter for large variations in the measured signal.

As a next step, the magnetic field dependence of $V(\omega)$ must be investigated. A magnetic field B (anti)parallel to the spin accumulation changes the kinetic energy of a given spin species, thus making the constriction spin sensitive. Consequently, the voltage drop $V(\omega)$ across the QPC is linear in the magnetic field[6]. In fact, one finds that the derivative of $V(\omega)$ with respect to the magnetic field is linear in the spin accumulation $\delta\mu_s$ with

$$\left.\frac{\partial(\delta V(\omega))}{\partial B}\right|_{B=0} = \frac{g\mu_{\mathrm{B}}\pi}{2e\hbar\omega_x}\delta\mu_s, \tag{6.20}$$

where g, μ_{B} and ω_x are the g-factor, Bohr magneton and curvature of the QPC, respectively. The derivation for equation 6.20 is shown in the appendix (see A). In the case of a magnetic field oriented antiparallel to the spin accumulation, the spin accumulation's energy penalty reduces the spin transmission probability, thereby decreasing $V(\omega)$. Conversely, in a parallel configuration, the transmission probability is enhanced. When an antiparallel magnetic field

---

[6] The fact that G_3 is linear in B also follows from inserting equation 6.5 into equation 6.3c.

is increased, $V(\omega)$ decreases with B and the slope $\partial_B(\delta V(\omega))$ is negative. At the point where the spin injection contacts switch from an antiparallel configuration to a parallel one, it is expected that $V(\omega)$ will exhibit a sudden increase, accompanied by a change in the sign of $\partial_B(\delta V(\omega))$.

Figure 6.16 shows results from measurements conducted at small magnetic fields, $B \in [20, 40, ..., 140\text{mT}]$, which allows to switch between antiparallel and parallel configurations between the spin accumulation and the magnetic field. The measurement was done at an excitation current $I_{\text{sd}} = 100\,\text{nA}$ at the last conductance step $G_1 \to G_0$. In (a) the measured voltage $V(\omega)/I_{\text{sd}}$ normalized by the excitation current is shown. Plotted are curves at $B = 20\,\text{mT}$ (black), $B = 80\,\text{mT}$ (green) and $B = 140\,\text{mT}$ (red). In addition, the second harmonic voltage drop $V(2\omega)/I_{\text{sd}}^2$ normalized by the square of injection current is shown as a dotted line. $V(2\omega)$ is linear in the transconductance of the QPC and was covered in detail in the previous chapter. As G_3 is also linear in the transconductance, it is expected that both $V(\omega)$ and $V(2\omega)$ exhibit a similar slope. This behavior is observed for split-gate voltages $V_{\text{G}} > -6.32\,\text{V}$. Upon decreasing V_{G} further, $V(2\omega)$ decreases opposed to the observed increase in $V(\omega)$. The opposing behavior in the slope of $V(\omega)$ and $V(2\omega)$ may arise from a possible increased contribution of G_4 to the denominator in equation 6.19 as G_1 becomes small.

Due to high noise is it not possible to extract a relation between $V(\omega)$ and the applied magnetic field. To gain further insight, a moving average method was used to smooth the measurement data, which is shown in figure 6.16 (b). Even with the lower noise from the moving average, it is not possible to extract quantitative information on $V(\omega)$ with respect to B. While it appears that $V(\omega)$ has increased between $B = 20\,\text{mT}$ (black) and $B = 140\,\text{mT}$ (red), one does observe that $V(\omega)$ at $B = 80\,\text{mT}$ (green) intersects both the black and the red curve at various split-gate voltages. It should be noted that the moving average method must be used with caution, as a single high fluctuation during measurement can have a significant impact on the averaged signal over a wide range. Based on the data presented in figure 6.16 it appears that higher magnetic fields are necessary for achieving adequate resolution.

Consequently, measurements were conducted in the high magnetic field regime, and the results are displayed in figure 6.17. At any given magnetic field, the measurement was conducted at $I_{\text{sd}} \in [20, 40, 60, 80\,\text{nA}]$. The plot shows the voltage drop over the QPC, $V(\omega)/I_{\text{sd}}$, normalized by the excitation current. The data collapses on a single trace for each magnetic field, validating the aforementioned linear relation between excitation current and voltage drop. The data for $B = 0$ (red curves, for which the corresponding regions of high and low transconductance are highlighted), $B = 6\,\text{T}$ (green)

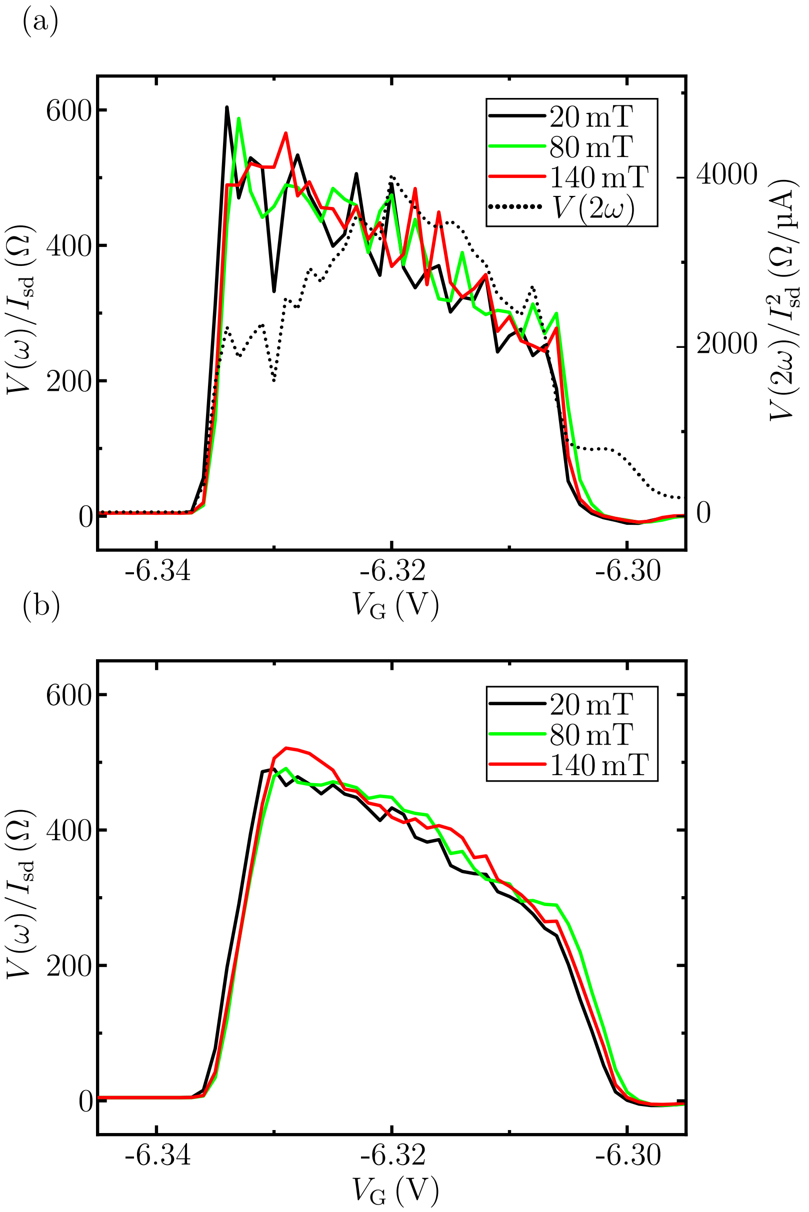

Figure 6.16: (a) Results of a non-local spin-to-charge conversion experiment at various in-plane magnetic fields $B = 20\,\mathrm{mT}$ (black curve), $B = 80\,\mathrm{mT}$ (green) and $B = 140\,\mathrm{mT}$ (red). Shown is the measured voltage drop across the QPC, $V(\omega)/I_{\rm sd}$, normalized by the excitation current $I_{\rm sd} = 100\,\mathrm{nA}$. As a reference for the slope of the signal, $V(2\omega)$ is also shown (dotted curve). Over a wide range of split-gate voltage $V_{\rm G}$, $V(\omega)$ and $V(2\omega)$ exhibit a similar slope. Due to the high noise, a magnetic field dependence cannot be extracted. (b) Moving average of the signal shown in (a). It seems that the signal increases with magnetic field. For unambiguity, higher magnetic fields appear imperative.

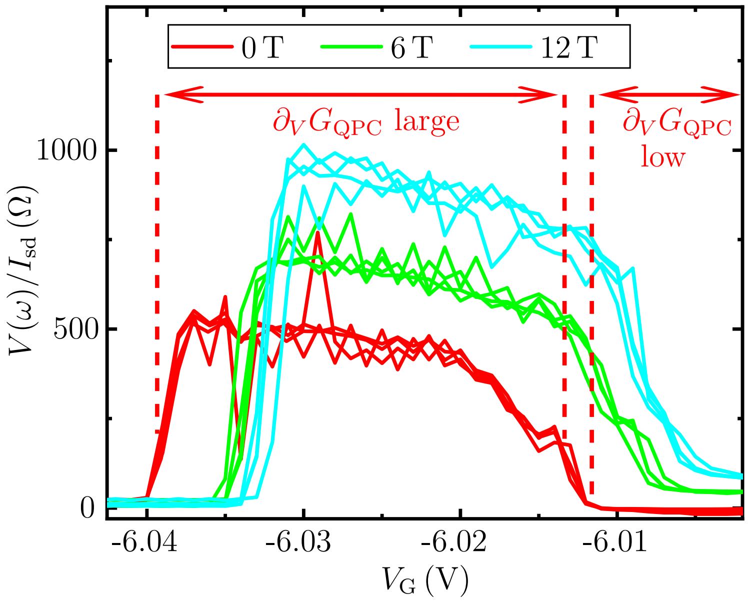

Figure 6.17: Voltage drop $V(\omega)/I_{\mathrm{sd}}$ over the QPC normalized by the excitation current. Measurements were conducted at $I_{\mathrm{sd}} \in [20, 40, 60, 80\,\mathrm{nA}]$, at magnetic fields $B = 0\,\mathrm{T}$ (red curves), $B = 6\,\mathrm{T}$ (green) and $B = 12\,\mathrm{T}$ (cyan). The data collapses on a single trace for a given magnetic field and it appears that $V(\omega)$ increases with B, indicating that the measured signal is of spin origin. For the data at $B = 0\,\mathrm{T}$, the dashed lines indicate the regions of high and low transconductance, respectively.

and $B = 12\,\mathrm{T}$ (cyan) are shown. For visual clarity, the data for $B = 3\,\mathrm{T}$ and $B = 9\,\mathrm{T}$ are not shown in the figure. $V(\omega)/I_{\mathrm{sd}}$ clearly increases with increasing magnetic field. At minimum transconductance, the splitting between values measured at high magnetic field and zero magnetic field is low, when the first subband is still populated at around $V_{\mathrm{G}} = -6.0\,\mathrm{V}$. As V_{G} decreases and the first subband is depopulated, $V(\omega)$ increases. At this point, an increased splitting between the voltages measured at high magnetic field and zero magnetic field is observed. While the voltage drop normalized by the excitation current reaches $\sim 550\,\Omega$ for $B = 0$ (red curves), it reaches $\sim 950\,\Omega$ for $B = 12\,\mathrm{T}$. As V_{G} is decreased further and the QPC pinches off, one finds $V(\omega) = 0$. The linearity of $V(\omega)$ in B is consistent with an interpretation that the measured signal originates from spin-related phenomena.

The increase in $V(\omega)$ with increasing magnetic field is consistent with the fact that B is parallel to the spin accumulation for such high values of B. As one cannot switch between a parallel and antiparallel orientation of B and the spin accumulation, the direction of the magnetic field can be reversed in order to check that $V(\omega)$ is spin related . In our samples, reversing the direction of $B \to -B$ should result in an increase in $V(\omega)$ as the magnetic field strength increases. It is expected that $V(\omega)$ is symmetric in B.

Figure 6.18 displays the results of linear spin-to-charge conversion measurements at negative magnetic fields in the high-field regime. The measurements were also conducted for multiple excitation currents $I_{\mathrm{sd}} \in [20, 40, 60, 80\,\mathrm{nA}]$. Shown is $V(\omega)/I_{\mathrm{sd}}$ as the averaged signal of all excitation currents at various magnetic fields. $V(\omega)/I_{\mathrm{sd}}$ increases linearly from $\sim 450\,\Omega$ at $B = -3\,\mathrm{T}$ (magenta curve) to higher values for $B = -6\,\mathrm{T}$ (cyan), $B = -9\,\mathrm{T}$ (blue) up to $\sim 685\,\Omega$ at $B = -12\,\mathrm{T}$ (green). The linear increase of $V(\omega)$ in a magnetic field parallel to the spin accumulation, regardless of the direction of B, agrees with expectations and further indicates that $V(\omega)$ is spin-related.

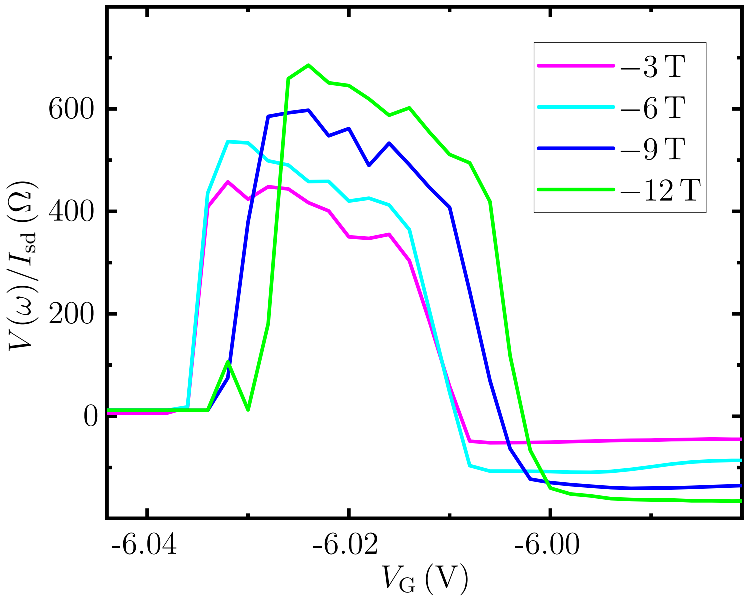

Figure 6.18: Measurements results of nonlinear spin-to-charge conversion for $I_{\mathrm{sd}} \in [20, 40, 60, 80\,\mathrm{nA}]$ at various magnetic fields. Shown is $V(\omega)/I_{\mathrm{sd}}$ averaged for all excitation currents at various negative magnetic fields. The alignment of the magnetic spin injection contacts with the external magnetic fields results in a spin accumulation parallel to the magnetic field. Thus, the correlation between the signal increase and the magnitude of the applied field indicates that the measured signal originates from spin.

Comparing the data presented in figures 6.17 and 6.18 reveals that $V(\omega)$ is not symmetric in B. At positive fields one finds larger resistances compared to the resistances at negative fields with $V(\omega, 12\,\mathrm{T})/I_{\mathrm{sd}} \sim 950\,\Omega > V(\omega, -12\,\mathrm{T})/I_{\mathrm{sd}} \sim 685\,\Omega$. Figure 6.19 shows magnetic field-resolved $V(\omega)/I_{\mathrm{sd}}$

at the point where the QPC is half open. To obtain the data, the average of $V(\omega)/I_{\mathrm{sd}}$ for all measured excitation currents was taken at a given magnetic field. The scatter plot confirms the linear relation between $V(\omega)/I_{\mathrm{sd}}$ and B. Shown are the results for negative magnetic fields (red dots) and for positive magnetic fields (black dots). For positive magnetic fields, $V(\omega)/I_{\mathrm{sd}}$ is linear in B. At $B = 9\,\mathrm{T}$ the data point is lower than expected, deviating from the linear relation. The linearity of $V(\omega)/I_{\mathrm{sd}}$ with respect to B is also observed for negative magnetic fields. One, however, finds that $V(\omega)/I_{\mathrm{sd}}$ has lower values at $B = -3\,\mathrm{T}$ compared to $B = 0$. In fact, figure 6.19 suggests that $V(\omega)/I_{\mathrm{sd}}$ is symmetric around $B = -3\,\mathrm{T}$. This would suggest that the applied magnetic field is antiparallel to the spin accumulation up to $B = -3\,\mathrm{T}$, which is imposisble for our devices. The spin contacts switch their magnetization configuration at $B \sim -30\,\mathrm{mT}$, see figure 5.3.

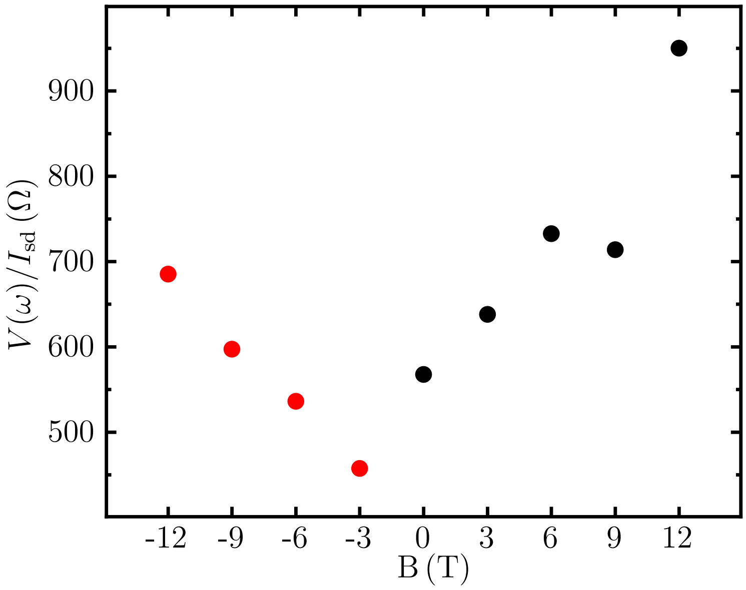

Figure 6.19: Magnetic field-resolved $V(\omega)/I_{\mathrm{sd}}$ at the point where the QPC is half open. Data are shown for negative magnetic fields (red dots) and positive magnetic fields (black dots). Although one observes linearity between $V(\omega)/I_{\mathrm{sd}}$ and B for positive and negative magnetic fields, one finds lower values of $V(\omega)/I_{\mathrm{sd}}$ at negative fields. This contradicts the expectation that $V(\omega)/I_{\mathrm{sd}}$ is symmetric around $B = 0$.

One possible explanation for the difference in $V(\omega)/I_{\mathrm{sd}}$ for positive magnetic fields and negative magnetic fields could be the fact that between measurements the pinch-off point of the QPC changes. More precisely, one finds that the pinch-off, which is the point at which $G = 0$ is reached and the constriction closes, shifts towards larger split-gate voltages V_G with time. This gradual shift in the pinch-off can also be observed in figures 6.17 and 6.18. In addition to the time-dependence of this shift, it appeared that sweeping B also resulted in a permanent[7] offset of the conductance curve to higher V_G. From a chronological point of view, linear spin-to-charge conversion experiments were first conducted at positive magnetic fields at $B = 0 \rightarrow 3\,\mathrm{T} \rightarrow 6\,\mathrm{T} \rightarrow 9\,\mathrm{T} \rightarrow 12\,\mathrm{T}$. After this, measurements were conducted at negative magnetic fields $B = -3\,\mathrm{T} \rightarrow -6\,\mathrm{T} \rightarrow -9\,\mathrm{T} \rightarrow -12\,\mathrm{T}$. In between linear spin-to-charge conversion experiments, no measurements of quantized conductance were performed to observe the properties of the QPC.

To investigate the impact of QPC-related properties, the measurements at positive magnetic fields were repeated. The results of the repeated measurement are shown in figure 6.20 (a). Shown are $V(\omega)/I_\mathrm{sd}$ as a function of V_G for $B = 0$ (red curve), $B = 3\,\mathrm{T}$ (green), $B = 6\,\mathrm{T}$ (blue), $B = 9\,\mathrm{T}$ (cyan) and $B = 12\,\mathrm{T}$ (magenta). In agreement with previous measurements, the curves show a δ-like curve and exhibit a linearity in both B and I_sd. It is interesting to note that the unexpected decrease in $V(\omega)/I_\mathrm{sd}$ at $B = 9\,\mathrm{T}$ is again observed. Possible reasons for this behavior are not known. To compare the data obtained in figure 6.20 (a) with previous results the curves were offset in V_G to align the points of maximum transconductance. The results are presented in figure 6.20 (b). Shown is $V(\omega)/I_\mathrm{sd}$ over V_G from the first measurement series for $B = 0$ (red curves), $B = 6\,\mathrm{T}$ (green) and $B = 12\,\mathrm{T}$ (cyan). The black dotted curves display the results from the measurement series repeating the experiment. One finds a good overlap between the original data and the data obtained from the second measurement series. This overlap includes not only the peak values of $V(\omega)/I_\mathrm{sd}$ but also the shape of the curves. The rising, plateau-like and falling features of the data all occur at the same points. These results suggest that the properties of the QPC remain stable and do not affect measurement outcomes, despite the fact that the pinch-off point changes with time. Consequently, the difference in $V(\omega)/I_\mathrm{sd}$ for positive and negative magnetic fields is not a result of a change in the properties of the QPC.

The difference in $V(\omega)/I_\mathrm{sd}$ for positive and negative magnetic fields can in fact be attributed to a background signal at the first conductance plateau. Figure 6.21 (a) displays $V(\omega)/I_\mathrm{sd}$ at $B = 0$ (black curve), $B = 12\,\mathrm{T}$ (blue) and $B = -12\,\mathrm{T}$ (red). The curves were adjusted in V_G so that the step in the signal occurs at the same point. Each curve is the average of all currents used,

---

[7] V_G can be shifted back to lower values by illuminating the sample. Too much illumination, however, may decrease step quality, see figure 5.7.

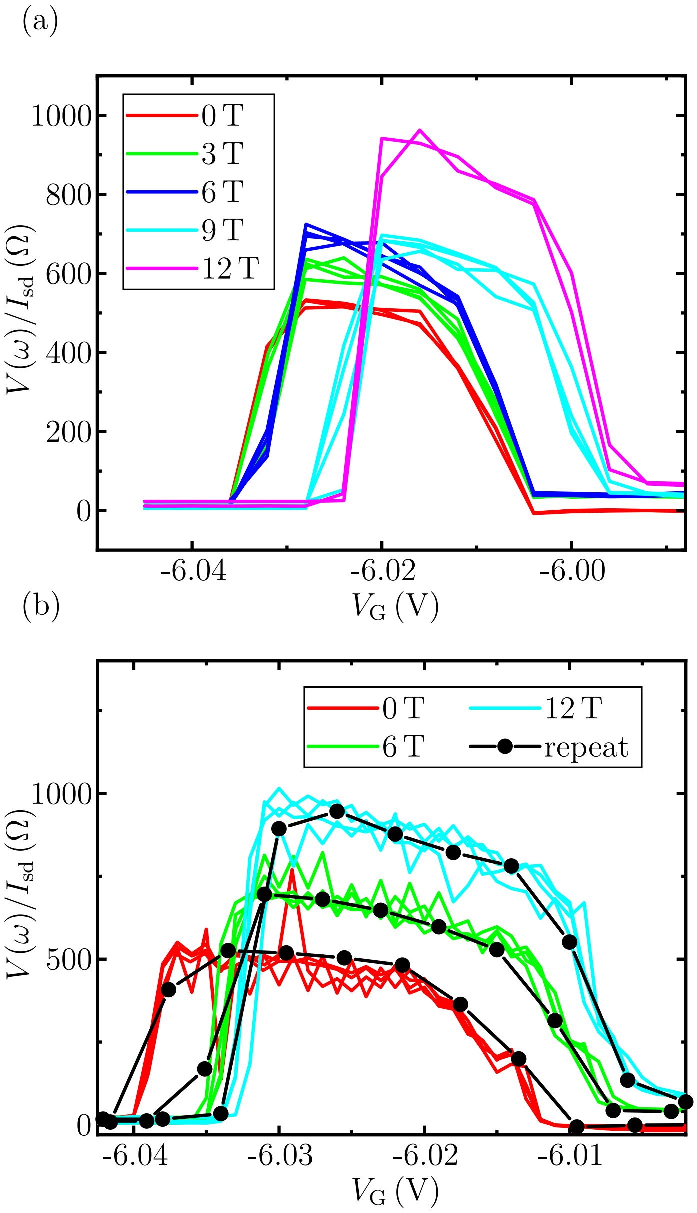

Figure 6.20: (a) Repeat of linear spin-to-charge conversion measurements at various magnetic fields. $V(\omega)/I_{\mathrm{sd}}$ over V_{G} shows the expected slope for various excitation currents. Similar to the previous measurement series, the linearity of the peak signal of $V(\omega)/I_{\mathrm{sd}}$ with applied magnetic field is not observed at $B = 9\,\mathrm{T}$. (b) First conducted linear spin-to-charge conversion measurements (colored curves) and the repeat measurement of linear spin-to-charge conversion (black dotted curves). To improve visibility, some curves were offset in V_{G}. The repeat measurement aligns well with the original data.

$I_{\mathrm{sd}} \in [20, 40, 60, 80\,\mathrm{nA}]$. To calculate the average, a linear interpolation of the data was performed prior to averaging. Since the transconductance is zero at the first conductance plateau (at $V_\mathrm{G} = -6.00\,\mathrm{V}$), one expects $V(\omega)/I_\mathrm{sd} = 0$. While the curve follows the expected behavior at $B = 0$, one finds $V(\omega)/I_\mathrm{sd} \neq 0$ for $B = 12\,\mathrm{T}$ and $B = -12\,\mathrm{T}$. The background $\Delta V'$ is correlated with the applied magnetic field. One finds that $\Delta V'$ is positive for $B > 0$ and negative for $B < 0$. Figure 6.21 (b) shows $V(\omega)/I_\mathrm{sd}$ with the removed background signal at the first conductance pleateau. Shown are the data at $B = 0$ (black curve), $B = 12\,\mathrm{T}$ (blue with solid dots), $B = 6\,\mathrm{T}$ (blue with empty dots), $B = -12\,\mathrm{T}$ (red with solid dots) and $B = -6\,\mathrm{T}$ (red with empty dots). After the background is removed, $V(\omega)/I_\mathrm{sd}$ still increases with increasing magnetic field. Furthermore, the signal overlaps for both positive and negative magnetic fields.

The fact that $V(\omega)/I_\mathrm{sd}$ is symmetric in B after removing the background signal is apparent in figure 6.22. Here, the value of $V(\omega)/I_\mathrm{sd}$ at maximum transconductance is shown with respect to applied magnetic field. Shown are data for positive magnetic fields (black dots) and negative magnetic fields (red). It is observed that $V(\omega)$ falls onto similar values as $B \rightarrow -B$ is reversed. In conclusion, one finds that all theoretical predictions for linear spin-to-charge conversion in our devices are met, namely a δ-like curve, linearity in B and I_sd and symmetry with respect to B.

As a next step, the value of the spin accumulation resulting from linear spin-to-charge conversion can be calculated. This calculation requires the slope of $V(\omega)$ with respect to B, which is obtained through a linear fit to the data in figure 6.22. Points marked as "x" were omitted for the calculation of linear fits, which are shown as solid lines for positive (black line) and negative (red) B. The linear fits yield a slope $\partial_B V(\omega)/I_\mathrm{sd} = -24\,\Omega/\mathrm{T}$ for negative magnetic fields and $\partial_B V(\omega)/I_\mathrm{sd} = 27\,\Omega/\mathrm{T}$ for positive magnetic fields, respectively. Inserting these results into equation 6.20 and using $g = -0.39$ [132] and $\hbar\omega_x = 1.84\,\mathrm{meV}$ yields

$$\delta\mu_s(B > 0) = -1416\,\mathrm{eV/A} \tag{6.21a}$$

$$\delta\mu_s(B < 0) = 1250\,\mathrm{eV/A}, \tag{6.21b}$$

respectively. Inserting $I_\mathrm{sd} = 20\,\mathrm{nA}$, which is an excitation current that was applied in the linear spin-to-charge conversion experiments, into equations 6.21a and 6.21b yields $\delta\mu_s(20\,\mathrm{nA}) = -28\,\mathrm{\mu eV}$ and $\delta\mu_s(20\,\mathrm{nA}) = 25\,\mathrm{\mu eV}$, respectively. Now, these values, which were obtained for a spin injection contact located $6.5\,\mathrm{\mu m}$ away from the QPC, can be compared to the results from spin valve measurements. Non-local spin valve measurements cannot be conducted at the excitation currents used for linear spin-to-charge conversion. However, one can assume a constant spin injection efficiency over a wide range of I_sd [154].

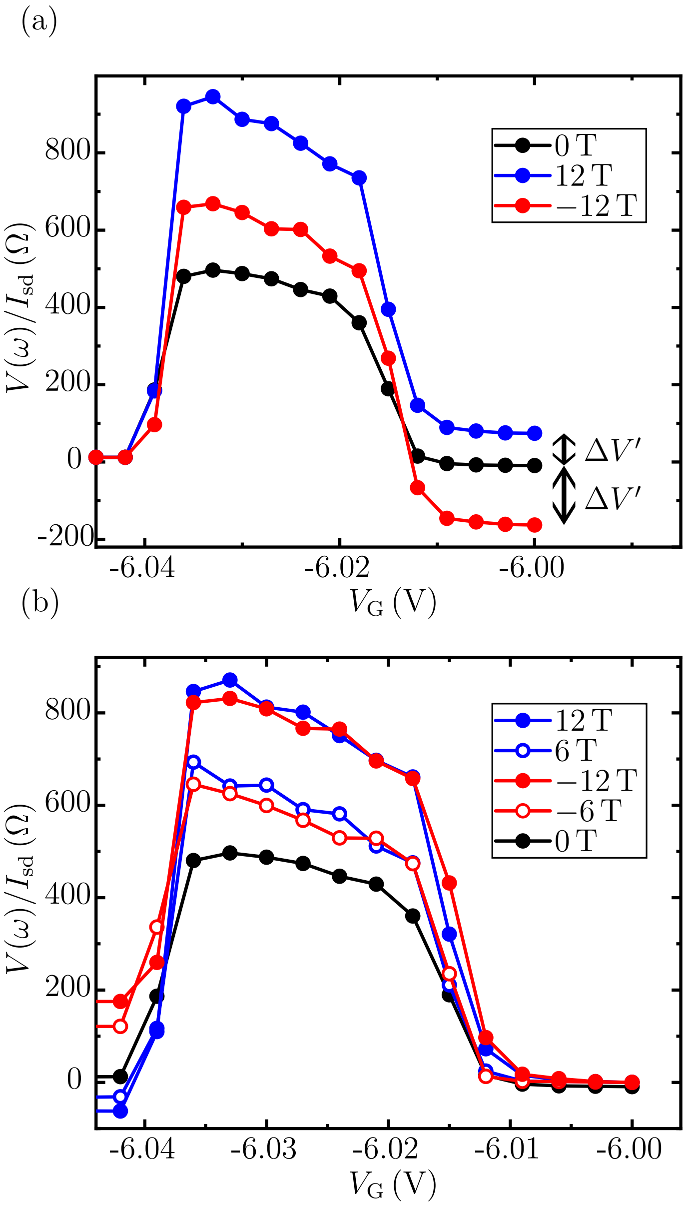

Figure 6.21: (a) $V(\omega)/I_{\mathrm{sd}}$ at $B = 0$ (black), $B = 12\,\mathrm{T}$ (blue) and $B = -12\,\mathrm{T}$ (red). To enhace data comparability, the curves were shifted in V_{G} to ensure that the signal rise occurs at the same point. At $V_{\mathrm{G}} = -6.00\,\mathrm{V}$, where the first conductance plateau is located, one finds a background signal $\Delta V'$ which correlates with the applied magnetic field. (b) $V(\omega)/I_{\mathrm{sd}}$ at $B = 0$ (black curve), $B = 12\,\mathrm{T}$ (blue with solid dots), $B = 6\,\mathrm{T}$ (blue with empty dots), $B = -12\,\mathrm{T}$ (red with solid dots) and $B = -6\,\mathrm{T}$ (red with empty dots) after subtracting $\Delta V'$. One finds that $V(\omega)/I_{\mathrm{sd}}$ remains linear in B and overlaps for positive and negative magnetic fields.

Equation 6.16 can then be utilized to calculate the spin accumulation from non-local spin valve measurements at low excitation currents. At $I_{\mathrm{sd}} = 20\,\mathrm{nA}$, one would find $\delta\mu_s(20\,\mathrm{nA}) = 27\,\mathrm{neV}$. In practice, the spin valve signal would be obscurred by noise while utilizing such low excitation currents. Compared to the results obtained from non-local spin valve measurements, the spin accumulation calculated from linear spin-to-charge conversion is then larger by three orders of magnitude. This cannot be explained by measurement uncertainties. Next, possible reasons for this large increase will be discussed.

One possible explanation for an increased signal can be an enhanced g-factor in a QPC as the contriction closes, which is attributed to electron-electron interactions [152]. The g-factor was observed to be enhanced up to 10 times its original value at the last subband [129]. Unfortunately, the sample broke before the experimental determination of the g-factor for the sample used in this work. An additional explanation for an increased signal may be the contribution from ballistic effects. In this work, the mean free path is $l_{\mathrm{mfp}} = 5.75\,\mu\mathrm{m}$. This is smaller than the spin diffusion length $L_s = 7.2\,\mu\mathrm{m}$ and also smaller than the distance between the spin contact and the QPC. Chen

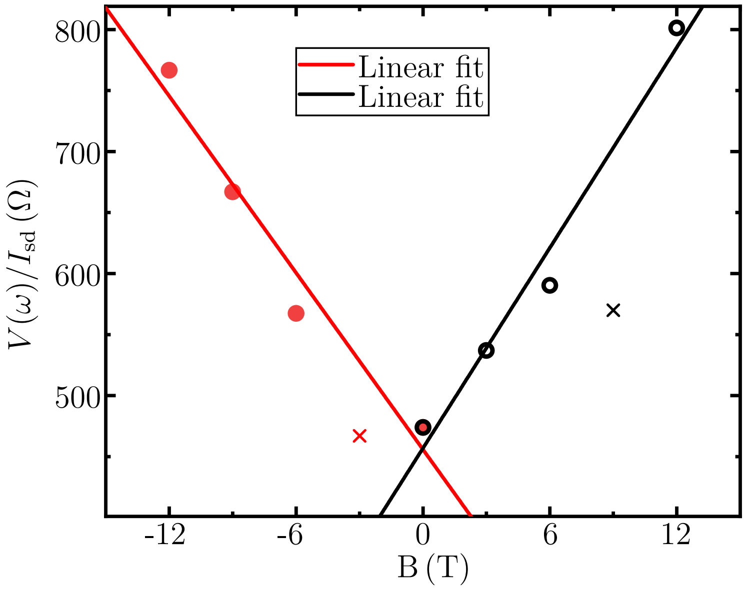

Figure 6.22: $V(\omega)/I_{\mathrm{sd}}$ at the point of maximum transconductance after the background has been removed. The data is both symmetric and linear in B. For both positive (black solid line) and negative (red) magnetic fields, a linear slope was fitted to the data. Points marked with an 'x' were excluded from the fits. The linear fits yield a slope of $\partial_B V(\omega)/I_{\mathrm{sd}} = -24\,\Omega/\mathrm{T}$ and $\partial_B V(\omega)/I_{\mathrm{sd}} = 27\,\Omega/\mathrm{T}$, respectively.

et al. calculated that the spin accumulation can be increased in the ballistic regime [155]. The prerequisites for an increase in spin accumulation in the ballistic regime are a spin dependent tunnel barrier with a large resistance and a mean free path greater than the spin diffusion length. This leads to an increase in the spin accumulation by a factor $\eta = 1 + l_{\mathrm{mfp}}^2/L_s^2$. If the spins are travelling ballistically towards the constriction, the enhancement factor in our devices would amount to ~ 1.7.

A third factor that could lead to an increase in the measured signal may be an enhanced spin accumulation at the QPC, which is a possibility that will now be shortly discussed. The presence of the constriction in the vincinity of the spin injection contact can change a distribution of spin accumulation in the channel. Therefore, it might be false to assume that the spin accumulation at the constriction has the same value as detected in a spin valve measurement with a non-constricted channel. The situation is illustrated in figure 6.23, which shows the channel without (a) and with a QPC (b). Two principal factors influence the physical principles underlying spin accumulation in the context of spin valve measurements and measurements employing a QPC for spin detection. The first reason for the discrepancy between spin valve measurements and spin-to-charge conversion experiments is that, for the latter, the spin accumulation must be at the center of the mesa where the constriction forms. This creates a two-dimensional problem as the constriction becomes narrow. The second difference is that the QPC creates a narrow channel at the point of the constriction, which can even be pinched-off at low split-gate voltages. This creates a bottleneck, which increases the spin accumulation. Enhancement of the spin accumulation in confined channels has been predicted theoretically within the standard model of spin injection [156] and observed experimentally as the enhancement of the local magnetoresistance signals [154]. In addition, it is possible that the QPC has other influences on the measured signals that extend beyond the description within the drift-diffusion model. Thomas *et al.* [152] found evidence of a possible spin polarization in a one-dimensional electron gas, even at zero magnetic field, which may have an influence on the spin accumulation detected by a QPC in our devices. All these factors may lead to a large increase in the measured signal compared to the expected value based on spin valve measurements. Nevertheless, we are unable to provide a quantitative explanation for the discrepancy in the spin accumulation detected by spin-to-charge conversion at the QPC, which is 1000 times larger than that observed with the spin valve effect.

An additional argument can be made in support of the interpretation that the measured signals originate from a spin accumulation that is enhanced by the presence of the QPC. This argument arises from a comparison of the spin accumulation calculated from linear and nonlinear measurements. At an excitation current of $I_{\mathrm{sd}} = 1\,\mu\mathrm{A}$, the spin accumulation extracted from linear spin-to-charge conversion measurements would amount to $\delta\mu_s = 1.35\,\mathrm{meV}$, assuming the standard value for the g-factor in a GaAs 2DEG, which is $g = -0.39$ [132]. It is, however, a known fact that the g-factor can be enhanced in a QPC [152], and the enhancement has been observed up to 10-fold [129]. Assuming a six-fold increase in the g-factor of the QPC, a spin accumulation of $\delta\mu_s = 225\,\mu\mathrm{eV}$ would be yielded at the constriction with an excitation current of $I_{\mathrm{sd}} = 1\,\mu\mathrm{A}$. This obtained value for the spin accumulation is still larger than expected. However, it must be noted again that the influence of the QPC on the spin accumulation is unknown. Therefore, it is possible that $\delta\mu_s = 225\,\mu\mathrm{eV}$ represents the spin accumulation value at the QPC.

Assuming the value of $\delta\mu_s = 225\,\mu\mathrm{eV}$, the expected signal for nonlinear spin-to-charge conversion experiments can be calculated using equation

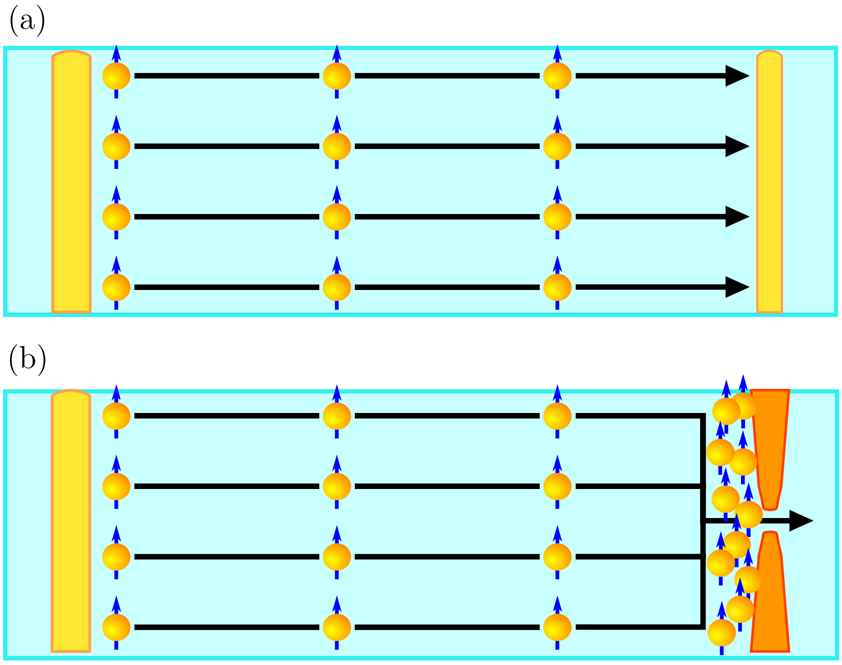

Figure 6.23: The theory for spin injection and spin detection is based on a one-dimensional random walk model, sketched in (a). During a spin valve measurement, a spin accumulation injected from the left spin contact (yellow) diffuses in x-direction and is detected by a second spin contact. (b) Nonlinear spin-to-charge conversion utilizing a QPC (orange). At the constriction imposed by the QPC, a bottleneck is created, which increases the spin accumulation. In addition, spins may have to travel in y-direction to pass through the constriction, making the problem two-dimensional.

6.17. Inserting $\hbar\omega_x = 1.84\,\text{meV}$, which was calculated in section 5.2, one finds that the measured voltage drop for nonlinear spin-to-charge conversion would amount to $V(2\omega) \sim 40\,\mu\text{V}$ at $I_{\text{sd}} = 1\,\mu\text{A}$. Nonlinear spin-to-charge conversion experiments at $I_{\text{sd}} = 1\,\mu\text{A}$ have been conducted in this work, and the results are shown in figure 6.3. The measured value of $V(2\omega) \sim 40\,\mu\text{V}$ is in good agreement with the calculations. These calculations show that the results obtained from nonlinear and linear spin-to-charge conversion are consistent with each other, and may be the result of the spin accumulation, under assumption that the latter is enhanced by the presence of the QPC.

If the measured nonlinear signal, $V(2\omega)$, and the linear signal, $V(\omega)$, are assumed to arise from the presence of a spin accumulation, it is important to note that the theoretical description of spin transport must be adjusted. The standard model of spin injection cannot be applied in this case. Using spin-to-charge conversion in a QPC appears to be not simply an alternative method of spin detection, but rather a distinct process with different physics. Simply speaking, a QPC is more than just a detector.

Utilizing linear spin-to-charge conversion to measure $\delta\mu_s$ offers the advantage of not requiring clear ferromagnetic switching, which is important for miniaturization. A spin accumulation can be measured using very low currents which are not accessible for spin valve measurements. In our devices, performing spin valve measurements at $I_{\text{sd}} = 20\,\text{nA}$ has never been achieved and may be impossible. Compared to spin valve measurements, however, various disadvantages have to be mentioned. These disadvantages include additional steps during sample fabrication. Defining split-gates by electron beam lithography requires precise cleanroom practice. Further drawbacks of linear spin-to-charge conversion are evident during measurement. To achieve quantized conductance, high mobilities are a prerequisite. Additionally, the measurement setup requires greater care. The last drawback is the fact that spin-to-charge conversion experiments require more time. While a spin valve measurement can be completed in $\sim 20\,\text{min}$, the linear spin-to-charge conversion measurements presented in this work extended over longer time periods. Obtaining data for a single measurement series required more than a day.

6.3 Conclusion

In this chapter, spin detection by means of nonlinear and linear spin-to-charge conversion in a QPC were analyzed. Experiments were conducted in a nonlocal setup where a spin-polarized current was injected on the left side of the QPC, and the right side was kept floating. The presence of a spin accumulation $\delta\mu_s$ at the constriction results in a measurable voltage drop across the

QPC. The measurement of nonlinear spin-to-charge conversion involves the second harmonic of the voltage drop, $V(2\omega) \propto \mu_s^2$, which is proportional to the square of the spin accumulation. In contrast, linear spin-to-charge conversion is measured by the first harmonic of the voltage drop, $V(\omega) \propto \mu_s$, which is linear in the spin accumulation.

The data obtained from nonlinear, non-local spin-to-charge conversion experiments aligned well with theoretical predictions. The shape of the measured curves follows the QPCs transconductance, weighted by the conductance of the QPC. Additionally, $V(2\omega)$ exhibited the expected proportionality with the square of the excitation current. The next step was to determine whether the measured signal originates from a spin accumulation or other effects. Here, one can utilize an out-of-plane magnetic field, which nullifies the effects of the spin accumulation, or distance-resolved measurements to prove the origin of spin. It was, however, not possible to confirm that the measured signal originates in spin.

For linear, non-local spin-to-charge conversion experiments, the measured signal, $V(\omega)$, is expected to be linear in both the transconductance of the QPC and the excitation current. These predictions were confirmed by the measured data. In addition, $V(\omega)$ is predicted to be linear in a magnetic field that is either parallel or anti-parallel to the spin accumulation. Measurements at low magnetic fields, which enable switching between parallel and antiparallel configurations, did not provide sufficient resolution for a definitive conclusion. Therefore, measurements in the high magnetic field regime, with fields up to $\pm 12\,\mathrm{T}$, were conducted. For the magnetic fields used in these experiments, the magnetization configuration of the spin contacts is always parallel to the magnetic field. Therefore, the spin accumulation is also always parallel to the magnetic field. This relationship is evident in the experimental data as the measured signal is linear in the magnitude of the applied external magnetic field, regardless of its sign. These facts suggest that the data obtained from linear, non-local spin-to-charge conversion experiments are of spin origin. Finally, the spin accumulation, $\delta\mu_s$, could be calculated and compared to the values obtained from spin valve measurements. The data from linear spin-to-charge conversion experiments, however, suggests a spin accumulation which is ~ 1000 times larger than predicted from spin valve measurements. The theory for spin-to-charge conversion presented in this work cannot explain this discrepancy. However, it is possible that the physics behind the spin accumulation is altered by the QPC. It is well-known that the g-factor may be enhanced in the QPC. Additionally, the constriction may create a bottleneck for the spin accumulation, increasing its magnitude.

When comparing the data from linear spin-to-charge conversion, where an enhanced g-factor was assumed, to that of nonlinear experiments, the measured signals indicate a similar spin accumulation. The absence of a proven spin origin for nonlinear spin-to-charge conversion may be attributed to the constriction, which could significantly alter the spin accumulation. Further investigation is required to fully comprehend the system's behavior, as the influence of a QPC might extend beyond mere spin detection.

Chapter 7

Summary

This work adressed spin detection by means of a quantum point contact (QPC), which acts as an energy barrier. Due to the different quasichemical potentials of spin-up and spin-down electrons, one finds different transmission probabilities through that energy barrier. This way, a QPC can be utilized for spin detection by means of *spin-to-charge conversion*. Prior to conducting the first spin-to-charge conversion experiments, certain requirements must be met. These include efficient spin injection and spin transport to obtain a large spin accumulation at the detection site, i.e., at the QPC. Additionally, a functioning QPC is necessary.

To examine the spin injection and spin transport properties of the devices used in this work, distance-resolved spin valve measurements were conducted. They revealed a high spin injection efficiency of $P = 56\%$ and a spin diffusion length of $L_s = 7.2\,\mu\text{m}$. Hanle measurements showed that small out-of-plane magnetic fields of $B_z = 60\,\text{mT}$ suppress the majority of the spin accumulation. These results confirm efficient spin injection and spin transport in the 2DEG.

The next step was to achieve quantized conductance, which is realized through split-gates across the mesa, perpendicular to the flow of electrons. To obtain the well-known step-like conductance pattern typical for a QPC, an appropriate split-gate geometry is required. As a first step, a split-gated device was fabricated on a wafer which has a large mobility, but no means of spin injection. By lowering the curvature of the split-gates, well defined plateaus could be achieved. The split-gate pattern was then transferred onto a device fabricated from a wafer suitable for spin injection. Source-drain biasing experiments then confirmed that the split-gate design used here is appropriate for measuring quantized conductance. As a final step, experiments showed that small out-of-plane magnetic fields up to $B_z = 50\,\text{mT}$ do not affect backscattering and leave the transmission properties of the QPC unaffected, which is important for future experiments. These experimental results demonstrate that all the necessary prerequisites for spin-to-charge conversion, namely efficient spin injection and transport, as well as quantized conductance, are met.

Finally, spin-to-charge conversion experiments were conducted. The experiments were conducted in a non-local setup where a spin-polarized current was injected on the left side of the QPC, and the right side was left floating. The presence of a spin accumulation $\delta\mu_s$ at the constriction results in a voltage drop across the QPC, which is measured during experiment. The measurement of nonlinear spin-to-charge conversion involves the second harmonic of the voltage drop, $V(2\omega) \propto \mu_s^2$, which is proportional to the square of the spin accumulation. In contrast, the measurement of linear spin-to-charge conversion involves the first harmonic of the voltage drop, $V(\omega) \propto \mu_s$, which is linear in the spin accumulation.

First, nonlinear spin-to-charge conversion experiments were conducted. Here, the measured data agrees well with the theoretical predictions for nonlinear spin-to-charge conversion. The first prediction is that the curves follow $\partial_V G/G$, which is the transconductance of the QPC, weighted by the QPCs conductance. In addition, $V(2\omega)$ is expected to be linear in the square of the spin accumulation, and, thus, linear in the square of the applied excitation current $V(2\omega) \propto I_{\mathrm{sd}}^2$, which is also observed during experiment. Now it had to be proven that $V(2\omega)$ arises from spin and not from other effects. This can be demonstrated by means of distance-resolved measurements, where an exponential decay of $V(2\omega)$ with a distance would be a clear sign of spin origin. In the first experiments, however, is was observed that $V(2\omega)$ increased as d is increased. It appeared that the geometry of the spin contacts play a significant role. To avoid ambiguity regarding the origin of $V(2\omega)$ in relation to different contact geometries, we fabricated a sample with identical spin contact geometries. With this sample, distance-resolved nonlinear spin-to-charge conversion measurements were performed once more. The measurements of $V(2\omega)$, however, could not provide evidence for a spin origin. Instead of the aforementioned exponential decay, a linear relation between $V(2\omega)$ and d was observed. Consequently, other means to prove spin origin were employed. The second method to prove the spin origin of $V(2\omega)$ was to utilize an out-of-plane magnetic field to suppress the spin signal, similar to Hanle measurements. This method, however, was also not successful in demonstrating that $V(2\omega)$ is related to spin. It is possible that the signal generated from thermopower obscures the signal generated from spin. Consequently, it was imperative to reduce the thermopower generated by the spin contacts. This was achieved by widening the spin contact to $w = 2\,\mu\mathrm{m}$. It was, however, still not possible to prove a spin-related component of $V(2\omega)$. This prompts the inquiry of whether it is possible to measure nonlinear spin-to-charge conversion for the devices utilized in this work. Therefore, a gedankenexperiment was presented as the final step. In this gedankenexperiment, we calculated the spin-related signal generated by an idealized device with a spin injection efficiency of $P = 100\%$ and ballistic spin transport. The calculations, however, demonstrate that the spin-related signal of $V(2\omega)$ is orders of magnitude below the measured data.

Next, linear spin-to-charge conversion experiments were conducted. From theory, it is expected that the measured signal, $V(\omega)$, is linear in the transconductance and linear in the spin accumulation, $\delta\mu_s$, and, therefore, in the excitation current I_{sd}. This was observed in the experimental data. In addition, $V(\omega)$ is predicted to be linear in an external magnetic field, which is either parallel or antiparallel to the spin accumulation. More precisely, the zero-field derivative of the measured signal, $\partial_B V(\omega)|_{B=0} \propto \delta\mu_s$, is predicted to be proportional to the spin accumulation. Therefore, measurements with in-plane magnetic fields were conducted. Initially, measurements were conducted in the low magnetic field regime, which allowed for switching between parallel and antiparallel configurations. However, the measurement data exhibited a low signal-to-noise ratio, which prevented the extraction of a magnetic field dependence of $V(\omega)$. Therefore, measurements in the high magnetic field regime were conducted. In this case, the magnetization configuration of the spin contacts, and, therefore, the spin accumulation, was always parallel to the magnetic field. This gave rise to the expectation that $V(\omega)$ is symmetric in B, which was confirmed by the measured data. To validate these experimental results, the measurement was repeated for positive magnetic fields. In the repeat measurements, the data from the initial measurements were successfully replicated. Next, the spin accumulation as a result from the linear spin-to-charge conversion experiments was calculated, and then compared to the results from spin valve measurements. At an excitation current of $I_{\mathrm{sd}} = 20\,\mathrm{nA}$, the data from linear spin-to-charge conversion experiments indicated a spin accumulation of $25\,\mu\mathrm{eV}$ and $-28\,\mu\mathrm{eV}$, respectively, which exceeds the value obtained from spin valve measurements by three orders of magnitude. It is, however, plausible that $V(\omega)$ is of spin origin, despite the discrepancy with spin valve measurements. In this case, the aforementioned discrepancy may arise from the QPC, which modifies the properties of the spin accumulation. These modifications include an enhanced g-factor and an enhancement of the spin accumulation at the constriction due to the formation of a bottleneck. Considering these factors, however, cannot explain the enhancement by three orders of magnitude.

The results from nonlinear and linear spin-to-charge conversion were then compared directly. If one calculates the spin accumulation resulting from linear spin-to-charge conversion under the assumption of a g-factor that is enhanced six-fold and uses the value of the spin accumulation to calculate the nonlinear signal, one finds a value that is similar to the results that were obtained experimentally. The implications are that the signal obtained for nonlinear spin-to-charge conversion experiments may be of spin origin and that a QPC is not only a detector. In the case of spin-to-charge conversion, it appears that a QPC is a complicated system with different physics compared to spin valve measurements. Spin-to-charge conversion via a QPC does not seem to be a substitute for the spin valve method, but rather a completely different system. Therefore, it is necessary to gain a better understanding of how the QPC affects spin accumulation in order to utilize spin-to-charge conversion in other devices.

Linear spin-to-charge conversion appears as to be a suitable method for spin detection in devices that cannot utilize the spin valve method, such as material systems that are incompatible with ferromagnets or materials that only allow for low current densities. For the devices used in this work, spin valve measurements were never performed with excitation currents below $I_{\mathrm{sd}} = 500\,\mathrm{nA}$ and at $I_{\mathrm{sd}} = 20\,\mathrm{nA}$, spin valve measurements would be impossible. Linear spin-to-charge conversion gives access to spin detection down to low current densities. In this work, we measured linear spin-to-charge conversion using an excitation current of $I_{\mathrm{sd}} = 20\,\mathrm{nA}$, and it seems possible to employ even lower current densities.

Appendix A

Calculations

Derivation of equation 6.7

One aims to calculate

$$\partial_E \mathcal{T}(E) = \partial_E \frac{1}{1+\exp(-2\pi(\frac{E-E_\mathrm{F}}{\hbar\omega_x}))}) \tag{A.1}$$

around $E = E_\mathrm{F}$ for $B \to 0$.

Utilizing the equations around small x

$$\partial_x \frac{1}{1+e^{-ax}} = \frac{ae^{-ax}}{(1+e^{-ax})^2} \tag{A.2a}$$

$$e^{-x} \approx 1 \tag{A.2b}$$

Thus, one finds

$$\partial_E \mathcal{T}(E) = \frac{a}{4} \tag{A.3}$$

At $E = E_\mathrm{F}$ one finds

$$-G_1 \mathrm{e}\delta V(\omega) = G_3 \delta\mu_s \tag{A.4a}$$

$$-\frac{1}{2}\frac{2\mathrm{e}}{\mathrm{h}}\mathrm{e}\delta V = \frac{-g\mu_\mathrm{B}B}{2}\frac{\frac{2\pi}{\hbar\omega_x}}{4}\frac{\mathrm{e}}{\mathrm{h}}\delta\mu_s \tag{A.4b}$$

$$\left.\frac{\partial V(\omega)}{\partial B}\right|_{B=0} = \frac{g\mu_\mathrm{B}\pi}{2\mathrm{e}\hbar\omega_x}\delta\mu_s. \tag{A.4c}$$

Equation 6.17 is derived in a similar manner.

Appendix B

Supplementary Measurements

Characterization of Wafer C210309A

Unless stated otherwise, measurements were conducted on devices fabricated from the wafer C191106B. It was, however, stated that the measurements presented in figure 6.6 were conducted on a different wafer. This wafer, C210309A, has the same heterostructure layout as wafer C191106B. For wafer C210309A, magnetotransport measurements, shown in figure B.1 yield a carrier density and mobility of $n_\mathrm{s} = 2.4 \cdot 10^{11}\,\mathrm{cm}^{-2}$ and $\mu_\mathrm{e} = 1.5 \cdot 10^{5}\,\mathrm{cm}^2/\mathrm{Vs}$, respectively.

This is in contrast to wafer C191106B, see figure 4.3, where the carrier density n_s and electron mobility μ_e were determined to be $n_\mathrm{s} = 3.5 \cdot 10^{11}\,\mathrm{cm}^{-2}$ and $\mu_\mathrm{e} = 5.9 \cdot 10^{5}\,\mathrm{cm}^2/\mathrm{Vs}$, respectively.

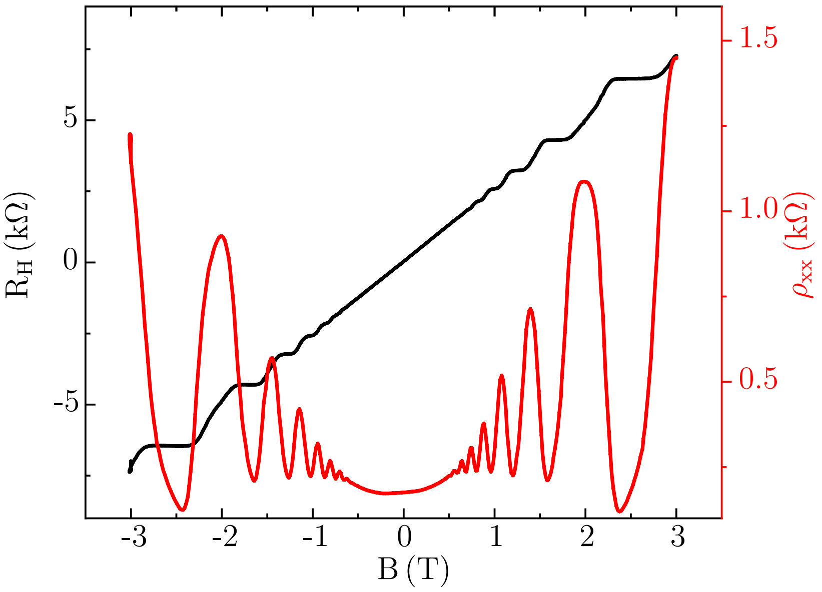

Figure B.1: Magnetotransport measurements of the wafer C210309A. One finds a carrier density and mobility of $n_\mathrm{s} = 2.4 \cdot 10^{11}\,\mathrm{cm}^{-2}$ and $\mu_\mathrm{e} = 1.5 \cdot 10^{5}\,\mathrm{cm}^2/\mathrm{Vs}$, respectively.

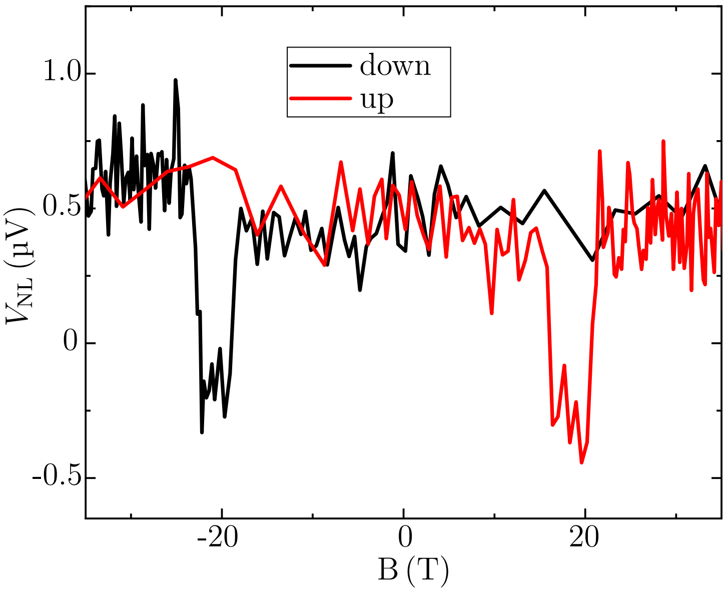

Figure B.2: Spin valve measurement conducted on wafer C210309A at an excitation current $I = 1\,\mu\mathrm{A}$.

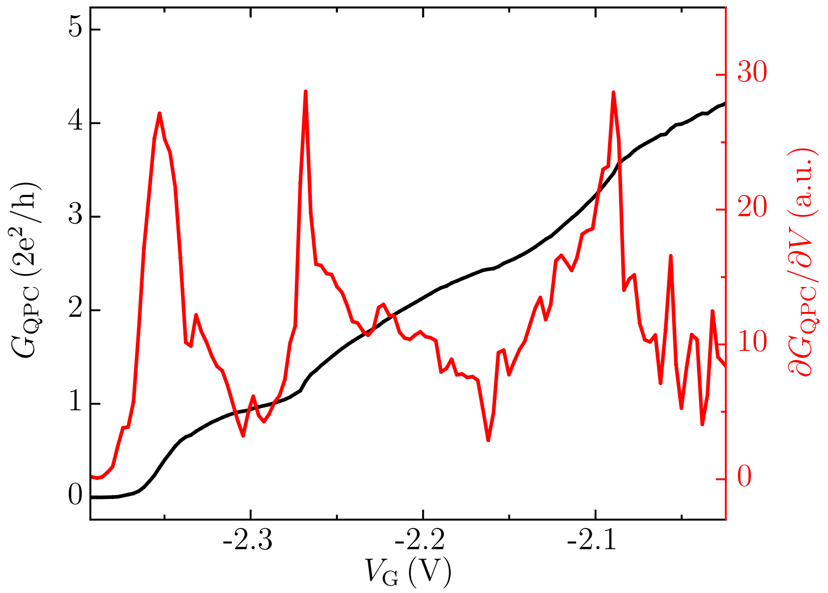

Figure B.3: Measurement of quantized conductance of a device fabricated from wafer C210309A.

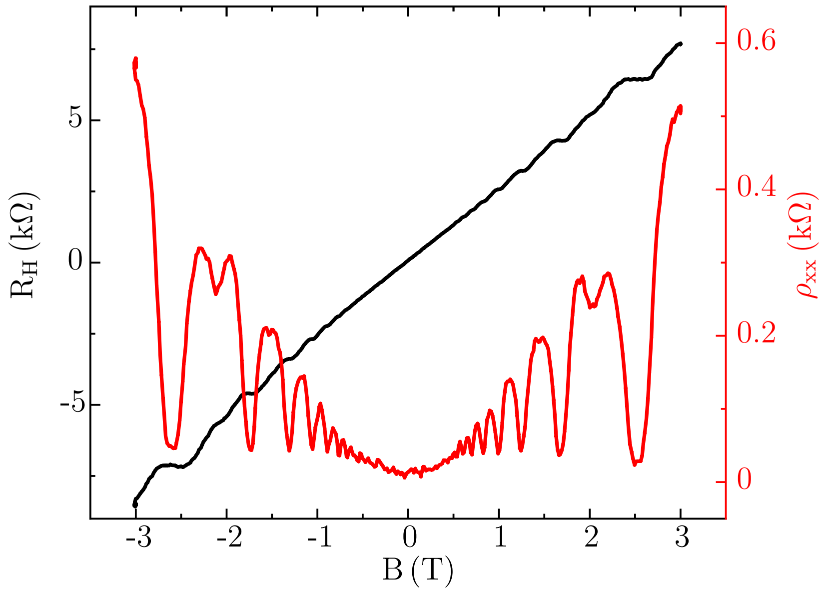

Figure B.4: Magnetotransport measurements conducted on wafer C120522B. This wafer was used for the fabrication of the devices in figure 5.6. The carrier density and mobility are $n_{\mathrm{s}} = 2.4 \cdot 10^{11}\,\mathrm{cm}^{-2}$ and $\mu_{\mathrm{e}} = 2.3 \cdot 10^{6}\,\mathrm{cm}^2/\mathrm{Vs}$, respectively.

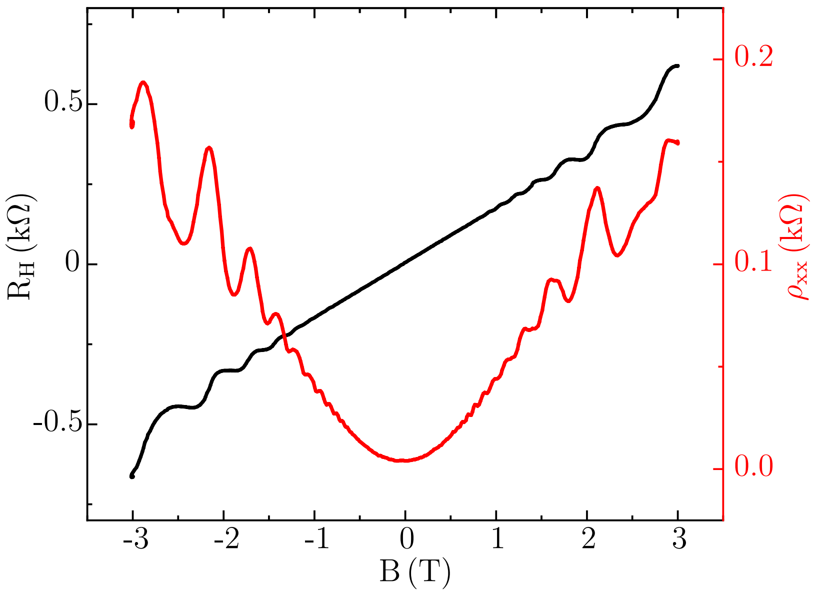

Figure B.5: Magnetotransport measurements conducted on wafer C191106B after too much illumination. The carrier density and mobility are $n_\mathrm{s} = 3.6 \cdot 10^{12}\,\mathrm{cm}^{-2}$ and $\mu_\mathrm{e} = 4.3 \cdot 10^5\,\mathrm{cm}^2/\mathrm{Vs}$, respectively.

Appendix C

Local Spin-to-Charge Coupling Measurements

In this subsection local measurements of spin-to-charge coupling are presented. The measurement setup is sketched in figure C.1. Basically, this is the setup used for measuring quantized conductance. Here, however, the source signal, which is a superimposed AC/DC voltage, is applied at a spin contact, while the drain is a reference contact on the other side of the constriction. This way, both a charge current and a spin current flow through the constriction. In addition to measuring the current flow through the device, the voltage drop over the constriction is also measured. More precisely, one is able to measure both the first harmonic of the voltage drop, which can be used to calculate the conductance, and also the second harmonic $V(2\omega)$. All measurements presented in this subsection were conducted in a dilution fridge at a temperature of 85 mK at an excitation frequency $f_{\mathrm{AC}} = 19\,\mathrm{Hz}$.

In contrast to a non-local configuration, the right side of the QPC is no longer a floating probe when conducting local measurements. Consequently, one expects that the presence of the spin accumulation leads to an increased current through the constriction [132] as the drain contact on the right side of the constriction has a fixed potential.

It has to be mentioned that the theory of spin-to-charge coupling from reference [132] was not developed for local experiments[1]. The voltage drop, which is measured across the QPC, depends on both the transconductance as well as on the spin accumulation ($V(\omega) \propto \delta\mu_s$ and $V(2\omega) \propto \delta\mu_s^2$).

In non-local spin-to-charge coupling experiments, the value of $\delta\mu_s$ may remain constant while the transconductance is varied by adjusting the split-gate voltage. In local experiments, this is not the case. Here, the spin accumulation, which is linear in the applied current, also varies upon sweeping split-

---

[1] This was confirmed by J. Fabian in conversation, one of the authors of reference [132].

gate voltage. As a result, the focus of this section does not lie in extracting calculated values of spin parameters, but rather in finding signatures of a spin-related signal. As mentioned before, applying an out-of-plane magnetic field provides means to suppress the spin-related signal through spin dephasing.

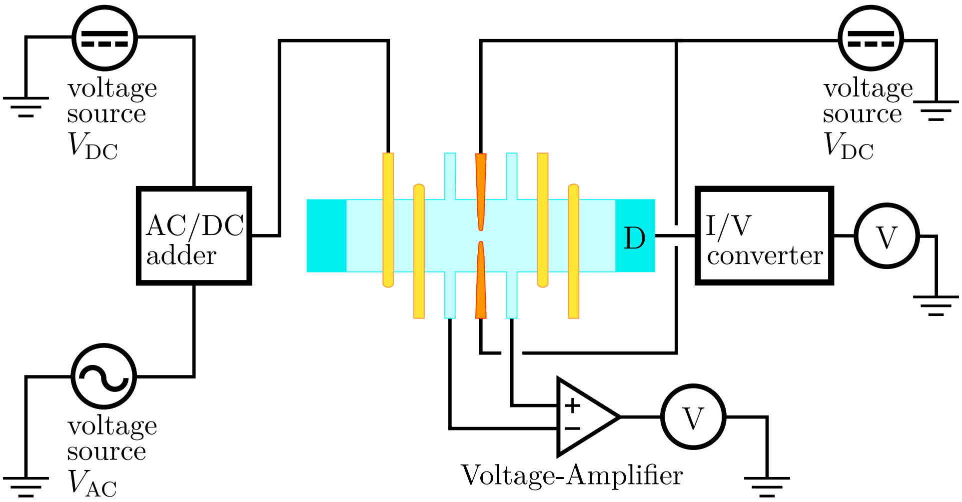

Figure C.1: Measurement setup for local spin-to-charge coupling experiments. A source voltage, which is a superposition of an AC/DC signal, is applied at a spin contact. This results in both a charge current and a spin current flowing through the QPC. The voltage drop over the constriction is measured using a multimeter. Both the first and second harmonics of the voltage drop are measured.

Figure C.2 (a) shows results of QPC measurements using a spin contact as a source. Shown are data for spin contacts located 6.5 µm (red curve), 9.5 µm (green), 12.5 µm (blue) and 15.5 µm (cyan) away from the constriction. In addition, measurements were conducted using a reference contact far away from the constriction (black). Five conductance plateaus can be observed for all curves with the clear, step-like transition between plateaus typical for QPC measurements. One can see that the curves obtained from spin contacts show more defined plateaus compared to the curve from the reference contact. The question now arises as to whether the improved step quality is a result of a spin accumulation.

Figure C.2 (b) displays the source-drain current through the sample during the measurements presented in (a). The current $I_{\mathrm{sd}} =\sim 50\,\mathrm{nA}$ at the last subband is of the same order of magnitude as for the measurements in the previous chapter. For all measurements, the same source drain-voltage was applied. In the case of the reference contact as a source, this results in a current which is significantly higher compared to the spin contacts. Most likely, the larger current through the constriction leads to a decreased step

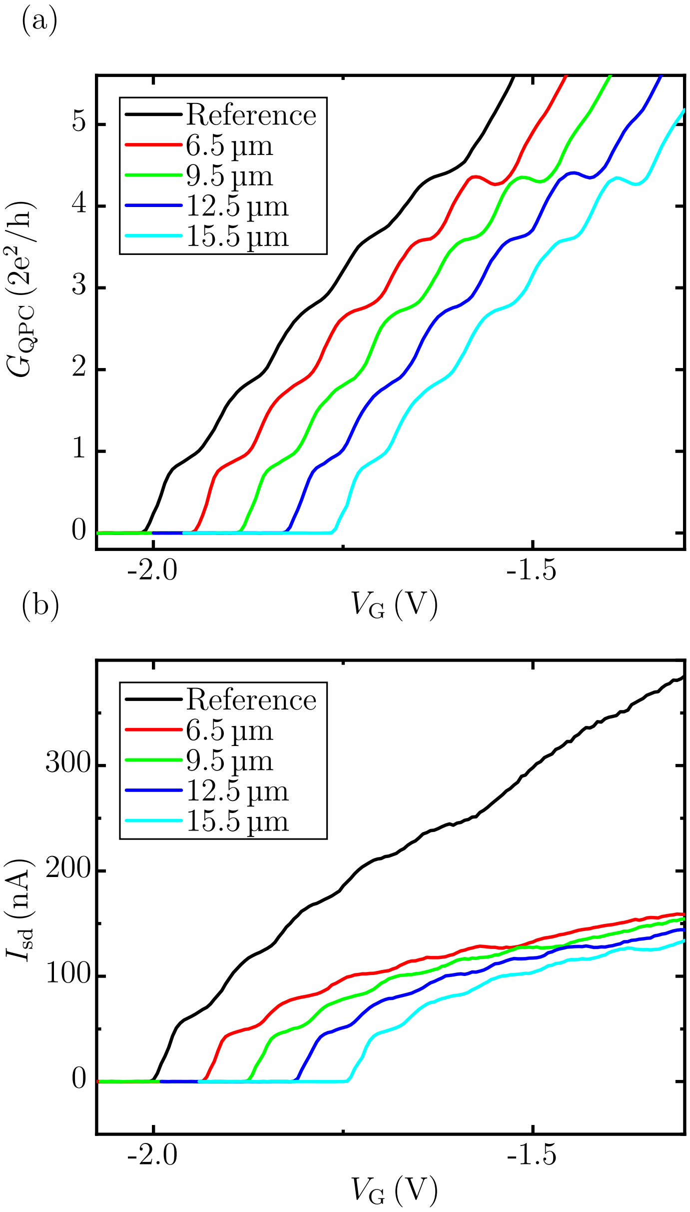

Figure C.2: Conductance curves obtained from local spin-to-charge coupling experiments. The spatial separation between the spin contacts and the QPC were 6.5 µm (red curve), 9.5 µm (green), 12.5 µm (blue) and 15.5 µm (cyan). In addition, a reference contact was utilized (black). The curves resulting from spin contacts exhibit more well defined plateaus. (b) Current through the sample during the measurements shown in (a). One finds that the reference contact has a larger current, which is most likely the reason for the difference in step quality.

quality. The current difference between the spin contacts and the reference contact also indicates a high resistance of the spin contacts resulting from the

Esaki diode. The reference contact, which is also made up of an Esaki diode, has an area of approximately $\sim 150 \times 150\,\mu\mathrm{m}$. Electrons travelling through the reference contact face a larger resistance caused by the mesa. However, for the spin contacts, the shorter mesa length is compensated by the large resistance of the Esaki diode, which has an area of $\sim 1 \times 20\,\mu\mathrm{m}$.

To evaluate the possible influence of a spin accumulation on the results presented in figure C.2 (a), the measurements were repeated in an out-of-plane magnetic field $B = 75\,\mathrm{mT}$. The results are presented in figure C.3. Shown is the conductance in units of $2\mathrm{e}^2/\mathrm{h}$ as a function of the split-gate voltage. The curves obtained for the spin contact (red curves), which is located $6.5\,\mu\mathrm{m}$ away from the QPC, are offset in V_g to better distinguish from the reference contact (black curves). The presence of an out-of-plane magnetic field $B = 75\,\mathrm{mT}$ (light black and light red curve, respectively) does not show a significant impact on the conductance traces. The overlap between $B = 0$ and $B = 75\,\mathrm{mT}$ is not perfect for the spin contact. However, the overlap upon applying a magnetic field is also not perfect for the reference contact. This implies that the difference between $B = 0$ and $B = 75\,\mathrm{mT}$ originates in the measurement setup in the form of fluctuations. As the various spin contacts vary in spatial separation to the QPC, one expects any spin dependent phenomenon to decay exponentially with distance. Observing the difference in conductance upon applying a magnetic field, no correlation with distance was observed (data not shown).

An in-plane magnetic field changes the Zeeman energy of a spin species. For large magnetic fields, spin degeneracy is broken and integer conductance values $G \sim \mathrm{e}^2/\mathrm{h}$ are observed. In long quantum wires, Liang *et al.* showed experimantally that electrons parallel to a magnetic field have a transmission probability of unity, whereas antiparallel electrons have a transmission probability of $\sim 65\%$ [157]. The manifestation of this was observed in the conductance traces. More precisely, the difference in conductance between plateaus amounted to $\Delta G \sim \mathrm{e}^2/\mathrm{h}$ or $\Delta G \sim 0.65\,\mathrm{e}^2/\mathrm{h}$. This represents either a situation where a change occurs from antiparallel to parallel ($\Delta G \sim \mathrm{e}^2/\mathrm{h}$) or from parallel to antiparallel $\Delta G \sim 0.65\,\mathrm{e}^2/\mathrm{h}$.

In this work, the measured conductance plateaus stay quantized to integer values of $2\mathrm{e}^2/\mathrm{h}$ up to in-plane magnetic fields of $B = 5\,\mathrm{T}$ (data not shown). No measurements were done at higher fields. For both the reference contact as well as the spin contact, a magnetic field changes the conductance curve. For various spin contacts, no distance dependence of relevant parameters was found. In reference [135], the spin current through the QPC was calculated to $I_{\text{spin, linear}} = 37\,\mathrm{pA}$ at the presence of a spin accumulation of $\delta\mu_s = 1\,\mu\mathrm{eV}$. While the curvature of the QPC is larger in this work, resulting in a larger

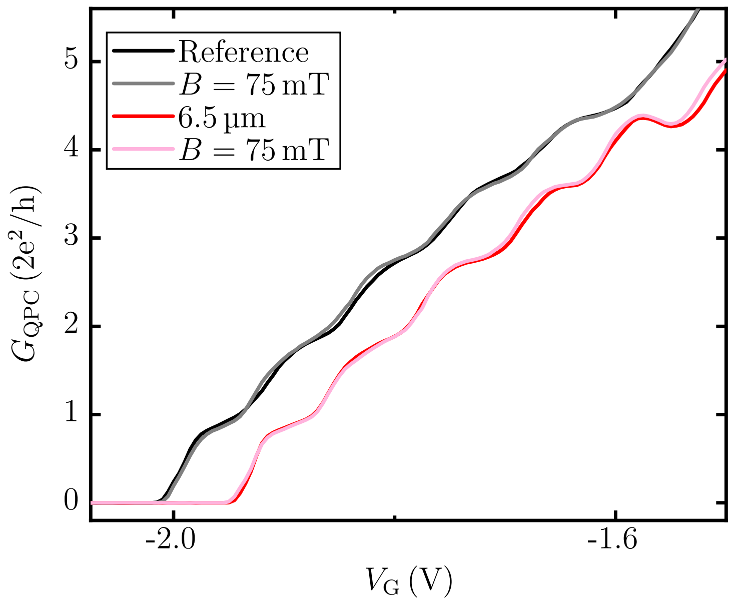

Figure C.3: Measurement of quantized conductance using a reference contact (black) at $B = 0$ and in an out-of-plane magnetic field $B = 75\,\mathrm{mT}$ (light gray). Also displayed are local spin-to-charge coupling measurements utilizing a spin contact 6.5 µm away from the QPC. These measurements were performed at $B = 0$ (red) and in an out-of-plane magnetic field $B = 75\,\mathrm{mT}$ (light red). There is no visible difference in the curves after dephasing a spin accumulation with a field.

spin current through the QPC [133], it has to be mentioned that the spin accumulation for the currents used during the measurements in this section are orders of magnitude below $\delta\mu_s = 1\,\mu\mathrm{eV}$ (see previous section).

Consequently, one finds that linear spin-to-charge coupling is not suitable for local measurements in the devices used in this work. The reason is that the change in current is obscured by noise and cannot be measured in experiment.

During local spin-to-charge coupling experiments, one can also measure the second harmonic of the voltage drop over the constriction. Figure C.4 shows $V(2\omega)$ as a function of split-gate voltage for the reference contact (black) and different spin contacts (colored curves) at $B = 0$. There is a clear difference between $V(2\omega)$ measured for the reference contact and for the spin contacts. For the former, the data is centered around zero for the full measurement range. Below $V_{\mathrm{g}}{-}0.75\,\mathrm{V}$, peaks resembling δ-functions are found at periodic intervals.

When utilizing spin contacts, the data looks different. From $V_{\mathrm{g}} \in [0, -0.75\,\mathrm{V}]$, one finds $V(2\omega) \approx 0$. Upon sweeping the split-gate voltage to lower values, the signal decreases. In general, it can be observed that the trace of $V(2\omega)$ follows the shape of the letter 'u' until the point where the QPC is pinched off. With the 'u' shape as an envelope function, δ-like peaks in $V(2\omega)$ are formed, which tend to increase in height as the constriction becomes more narrow.

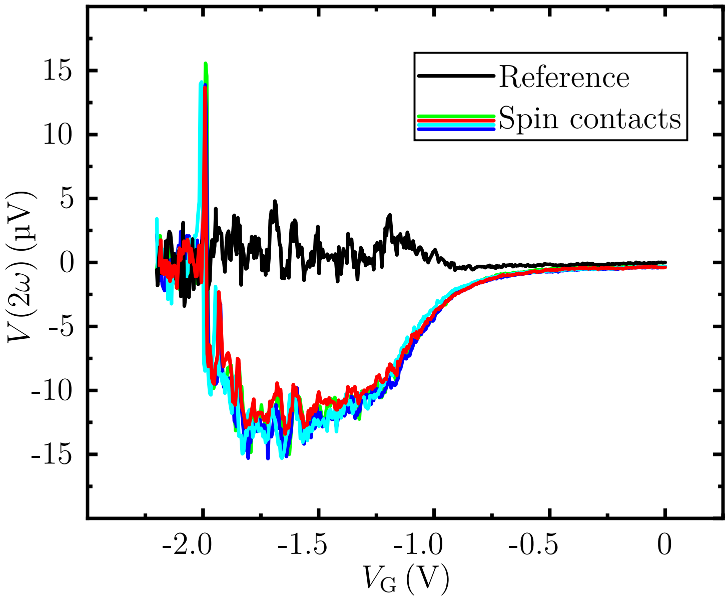

Figure C.4: Second harmonic of the voltage drop $V(2\omega)$ across a QPC during local measurements. One finds that the curve for the reference contact (black) has a different slope than the curves obtained using spin contacts (colored curves). All curves show δ-like peaks, which are observed periodically.

The main result from section 6.2.2, where non-local nonlinear spin-to-charge coupling experiments are discussed, is that thermopower dominates the nonlinear signal. One expects the same for local measurements. Regardless of the origin of $V(2\omega)$ in figure C.4, it is important to consider certain aspects.

First, no dependence between $V(2\omega)$ and the spatial separation between the QPC and the spin contact can be observed. On a second note it is important to consider that the shape of $V(2\omega)$ deviates from the expectation of simple δ-functions. This makes quantitative analysis difficult.

From equation 6.4 follows the expectation that the peak height increases with a decreasing number of modes. The spin accumulation, however, is also linear in the conductance of the QPC.

Consequently, as

$$\mathrm{e}\delta V(2\omega) = -\frac{1}{2}\frac{G_2}{G_1}\delta\mu_s^2 \propto -\frac{1}{2}\frac{G_2}{G_1}G_1^2 = -\frac{1}{2}G_2G_1, \tag{C.1}$$

the second harmonic voltage drop across the QPC is expected to be linear in the conductance of the constriction. In figure C.4, the opposite is observed. At the last step before the QPC closes, $V(2\omega)$ shows increased peak values, contrary to expectation.

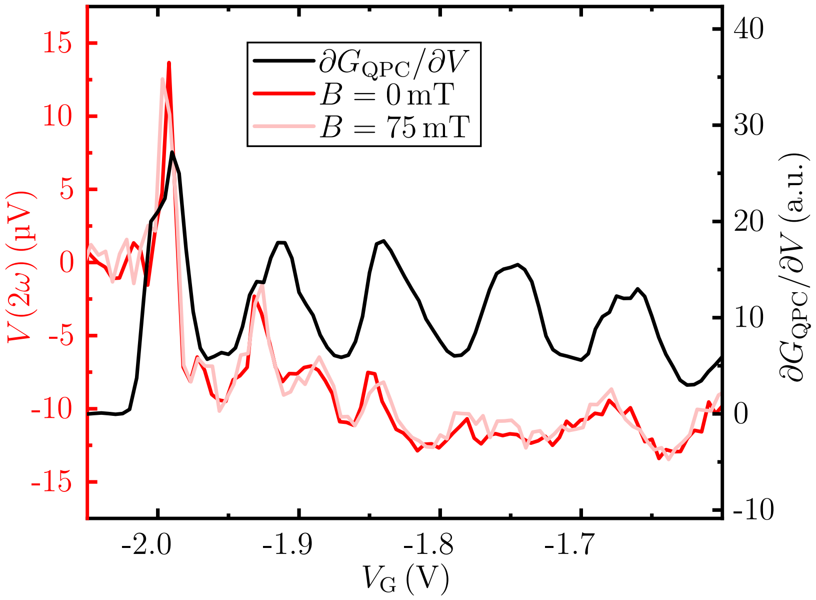

Figure C.5: Transconductance (black curve) and $V(2\omega)$ at $B = 0$ and in an out-of-plane magnetic field $B = 75\,\mathrm{mT}$. Although $V(2\omega)$ partially follows the transconductance, it is important to note that the correlation is not present at all times. The application of a magnetic field does not significantly alter $V(2\omega)$, suggesting that the signal originates in parameters unrelated to spin.

This shows that for local measurements, the theory presented in the beginning of this chapter cannot be applied.

Figure C.5 shows the transconductance (black curve) as well as $V(2\omega)$ at $B = 0$ (red) and at $B = 75\,\mathrm{mT}$ (light red). While the transconductance and $V(2\omega)$ display peaks at similar gate voltages, one finds a large difference in shape. At the final subband transition, $V(2\omega)$ and the transconductance overlap well.

Applying an out-of-plane magnetic field $B = 75\,\mathrm{mT}$ shows no visible influence on $V(2\omega)$. This confirms the expectation that, similar to section 6.2.2, a spin accumulation is not the driving force in the generation of $V(2\omega)$.

Bibliography

1. Bader, S. D. & Parkin, S. Spintronics. *Annu. Rev. Condens. Matter Phys.* **1,** 71–88 (2010).
2. Raffel, J. I. Operating characteristics of a thin film memory. *Journal of Applied Physics* **30,** S60–S61 (1959).
3. Pohm, A., Comstock, C. & Hurst, A. Quadrupled nondestructive outputs from magnetoresistive memory cells using reversed word fields. *Journal of applied physics* **67,** 4881–4883 (1990).
4. Childress, J. R. & Fontana Jr, R. E. Magnetic recording read head sensor technology. *Comptes Rendus Physique* **6,** 997–1012 (2005).
5. Solin, S. A. *et al.* Nonmagnetic semiconductors as read-head sensors for ultra-high-density magnetic recording. *Applied Physics Letters* **80,** 4012–4014 (2002).
6. Thomson, W. On the electro-dynamic qualities of metals: Effects of magnetization on the electric conductivity of nickel and of iron. *Proceedings of the Royal Society of London,* 546–550 (1857).
7. Zhao, C.-J., Ding, L., HuangFu, J.-S., Zhang, J.-Y. & Yu, G.-H. Research progress in anisotropic magnetoresistance. *Rare Metals* **32,** 213–224 (2013).
8. Gerlach, W. & Stern, O. Der experimentelle Nachweis des magnetischen Moments des Silberatoms. *Zeitschrift für Physik* **8,** 110–111 (1921).
9. Gerlach, W. & Stern, O. Der experimentelle nachweis der richtungsquantelung im magnetfeld. *Zeitschrift für Physik* **9,** 349–352 (1922).
10. Gerlach, W. & Stern, O. Das magnetische moment des silberatoms. *Zeitschrift für Physik* **9,** 353–355 (1922).
11. Julliere, M. Tunneling between ferromagnetic films. *Physics letters A* **54,** 225–226 (1975).
12. Butler, W., Zhang, X.-G., Schulthess, T. & MacLaren, J. Spin-dependent tunneling conductance of Fe| MgO| Fe sandwiches. *Physical Review B* **63,** 054416 (2001).

13. Ikeda, S. *et al.* Tunnel magnetoresistance of 604% at 300K by suppression of Ta diffusion in CoFeB/ MgO/ CoFeB pseudo-spin-valves annealed at high temperature. *Applied Physics Letters* **93** (2008).

14. Binasch, G., Grünberg, P., Saurenbach, F. & Zinn, W. Enhanced magnetoresistance in layered magnetic structures with antiferromagnetic interlayer exchange. *Physical review B* **39,** 4828 (1989).

15. Baibich, M. N. *et al.* Giant magnetoresistance of (001) Fe/(001) Cr magnetic superlattices. *Physical review letters* **61,** 2472 (1988).

16. Thompson, S. M. The discovery, development and future of GMR: The Nobel Prize 2007. *Journal of Physics D: Applied Physics* **41,** 093001 (2008).

17. Hirota, E., Sakakima, H. & Inomata, K. *Giant magneto-resistance devices* (Springer Science & Business Media, 2013).

18. De Groot, R., Mueller, F., van Engen, P. v. & Buschow, K. New class of materials: half-metallic ferromagnets. *Physical review letters* **50,** 2024 (1983).

19. Pickett, W. E. & Moodera, J. S. Half metallic magnets. *Physics Today* **54,** 39–44 (2001).

20. Soulen Jr, R. *et al.* Measuring the spin polarization of a metal with a superconducting point contact. *science* **282,** 85–88 (1998).

21. Park, J.-H. *et al.* Direct evidence for a half-metallic ferromagnet. *Nature* **392,** 794–796 (1998).

22. Schwarz, K. CrO2 predicted as a half-metallic ferromagnet. *Journal of Physics F: Metal Physics* **16,** L211 (1986).

23. Ohno, H. *et al.* (Ga, Mn) As: a new diluted magnetic semiconductor based on GaAs. *Applied Physics Letters* **69,** 363–365 (1996).

24. Dietl, T. & Ohno, H. Dilute ferromagnetic semiconductors: Physics and spintronic structures. *Reviews of Modern Physics* **86,** 187 (2014).

25. Braden, J., Parker, r. J., Xiong, g. P., Chun, S. & Samarth, N. Direct measurement of the spin polarization of the magnetic semiconductor (Ga, Mn) As. *Physical review letters* **91,** 056602 (2003).

26. Gross, R. & Marx, A. *Festkörperphysik* (Oldenbourg Wissenschaftsverlag Verlag, 2012).

27. Datta, S. & Das, B. Electronic analog of the electro-optic modulator. *Applied Physics Letters* **56,** 665–667 (1990).

28. Schäpers, T. *Semiconductor Spintronics* ISBN: 9783110425444. `https://doi.org/10.1515/9783110425444` (De Gruyter, Berlin, Boston, 2016).

29. Han, W. *et al.* Tunneling spin injection into single layer graphene. *Physical review letters* **105,** 167202 (2010).

30. Sasaki, T. *et al.* Electrical spin injection into silicon using MgO tunnel barrier. *Applied Physics Express* **2,** 053003 (2009).

31. Koo, H. C. *et al.* Electrical spin injection and detection in an InAs quantum well. *Applied physics letters* **90** (2007).

32. Bruski, P. *et al.* All-electrical spin injection and detection in the Co2FeSi/GaAs hybrid system in the local and non-local configuration. *Applied Physics Letters* **103** (2013).

33. Lou, X. *et al.* Electrical detection of spin transport in lateral ferromagnet–semiconductor devices. *Nature Physics* **3,** 197–202 (2007).

34. Van't Erve, O. *et al.* Electrical injection and detection of spin-polarized carriers in silicon in a lateral transport geometry. *Applied Physics Letters* **91** (2007).

35. Hammar, P. & Johnson, M. Spin-dependent current transmission across a ferromagnet–insulator–two-dimensional electron gas junction. *Applied Physics Letters* **79,** 2591–2593 (2001).

36. Ciorga, M. *et al.* Electrical spin injection and detection in lateral all-semiconductor devices. *Physical Review B* **79,** 165321 (2009).

37. Oltscher, M. *et al.* Electrical spin injection into high mobility 2D systems. *Physical Review Letters* **113,** 236602 (2014).

38. Eberle, F., Schuh, D., Bougeard, D., Weiss, D. & Ciorga, M. Diffusive Spin Transport in Narrow Two-Dimensional-Electron-gas Channels. *Physical Review Applied* **16,** 014010 (2021).

39. Eberle, F. *et al.* Controlled Rotation of Electrically Injected Spins in a Nonballistic Spin-Field-Effect Transistor. *Nano Letters* (2023).

40. Moore, G. E. Cramming more components onto integrated circuits, Reprinted from Electronics, volume 38, number 8, April 19, 1965, pp. 114 ff. *IEEE solid-state circuits society newsletter* **11,** 33–35 (2006).

41. Mollick, E. Establishing Moore's law. *IEEE Annals of the History of Computing* **28,** 62–75 (2006).

42. Thompson, S. E. & Parthasarathy, S. Moore's law: the future of Si microelectronics. *Materials today* **9,** 20–25 (2006).

43. Mott, N. F. The electrical conductivity of transition metals. *Proceedings of the Royal Society of London. Series A-Mathematical and Physical Sciences* **153,** 699–717 (1936).

44. Mott, N. F. The resistance and thermoelectric properties of the transition metals. *Proceedings of the Royal Society of London. Series A-Mathematical and Physical Sciences* **156,** 368–382 (1936).

45. Schmidt, G. & Molenkamp, L. Spin injection into semiconductors, physics and experiments. *Semiconductor science and technology* **17,** 310 (2002).

46. Schmidt, G., Ferrand, D., Molenkamp, L., Filip, A. & Van Wees, B. Fundamental obstacle for electrical spin injection from a ferromagnetic metal into a diffusive semiconductor. *Physical Review B* **62,** R4790 (2000).

47. Rashba, E. Theory of electrical spin injection: Tunnel contacts as a solution of the conductivity mismatch problem. *Physical Review B* **62,** R16267 (2000).

48. Fabian, J., Matos-Abiague, A., Ertler, C., Stano, P. & Zutic, I. Semiconductor spintronics. *Acta Phys. Slovaca* **57,** 567–907 (2007).

49. Aronov, A. Spin injection in metals and polarization of nuclei. *ZhETF Pisma Redaktsiiu* **24,** 37 (1976).

50. Johnson, M. & Silsbee, R. Thermodynamic analysis of interfacial transport and of the thermomagnetoelectric system. *Physical Review B* **35,** 4959 (1987).

51. Johnson, M. & Silsbee, R. Coupling of electronic charge and spin at a ferromagnetic-paramagnetic metal interface. *Physical Review B* **37,** 5312 (1988).

52. Van Son, P., Van Kempen, H. & Wyder, P. Boundary resistance of the ferromagnetic-nonferromagnetic metal interface. *Physical Review Letters* **58,** 2271 (1987).

53. Valet, T. & Fert, A. Theory of the perpendicular magnetoresistance in magnetic multilayers. *Physical Review B* **48,** 7099 (1993).

54. Fert, A. & Jaffres, H. Conditions for efficient spin injection from a ferromagnetic metal into a semiconductor. *Physical Review B* **64,** 184420 (2001).

55. Hershfield, S. & Zhao, H. L. Charge and spin transport through a metallic ferromagnetic-paramagnetic-ferromagnetic junction. *Physical Review B* **56,** 3296 (1997).

56. Rashba, E. I. Diffusion theory of spin injection through resistive contacts. *The European Physical Journal B-Condensed Matter and Complex Systems* **29,** 513–527 (2002).

57. Fabian, J., Žutić, I. & Sarma, S. D. Theory of spin-polarized bipolar transport in magnetic p- n junctions. *Physical Review B* **66,** 165301 (2002).

58. Žutić, I., Fabian, J. & Sarma, S. D. Spin-polarized transport in inhomogeneous magnetic semiconductors: theory of magnetic/nonmagnetic p- n junctions. *Physical review letters* **88,** 066603 (2002).

59. Vignale, G. & D'Amico, I. Coulomb drag, magnetoresistance, and spin-current injection in magnetic multilayers. *Solid state communications* **127,** 829–834 (2003).

60. Žutić, I., Fabian, J. & Sarma, S. D. Spintronics: Fundamentals and applications. *Reviews of modern physics* **76,** 323 (2004).

61. Johnson, M. Analysis of anomalous multilayer magnetoresistance within the thermomagnetoelectric system. *Physical review letters* **67,** 3594 (1991).

62. Silsbee, R. Novel method for the study of spin transport in conductors. *Bull. Magn. Reson* **2,** 284–285 (1980).

63. Johnson, M. & Silsbee, R. H. Interfacial charge-spin coupling: Injection and detection of spin magnetization in metals. *Physical review letters* **55,** 1790 (1985).

64. Ando, T., Fowler, A. B. & Stern, F. Electronic properties of two-dimensional systems. *Reviews of Modern Physics* **54,** 437 (1982).

65. Anderson, R. L. Experiments on ge-gaas heterojunctions. *Solid-State Electronics* **5,** 341–351 (1962).

66. Davies, J. H. *The physics of low-dimensional semiconductors: an introduction* (Cambridge university press, 1998).

67. Abramowitz, M. & Stegun, I. A. Handbook of Mathematical Functions with Formulas, Graphs, and Mathematical Tables. National Bureau of Standards Applied Mathematics Series 55. Tenth Printing. (1972).

68. Ihn, T. *Semiconductor Nanostructures: Quantum states and electronic transport* (OUP Oxford, 2009).

69. Van Houten, H., van Wees, B. J. & Beenakker, C. W. J. *Quantum and Classical Ballistic Transport in Constricted Two-Dimensional Electron Gases* in *Physics and Technology of Submicron Structures* (eds Heinrich, H., Bauer, G. & Kuchar, F.) (Springer Berlin Heidelberg, 1988), 198–207.

70. Büttiker, M. Quantized transmission of a saddle-point constriction. *Physical Review B* **41,** 7906 (1990).

71. Van Wees, B. *et al.* Quantized conductance of point contacts in a two-dimensional electron gas. *Physical Review Letters* **60,** 848 (1988).

72. Wharam, D. *et al.* One-dimensional transport and the quantisation of the ballistic resistance. *Journal of Physics C: solid state physics* **21,** L209 (1988).

73. Landauer, R. Spatial variation of currents and fields due to localized scatterers in metallic conduction. *IBM Journal of research and development* **1,** 223–231 (1957).

74. Landauer, R. Spatial variation of currents and fields due to localized scatterers in metallic conduction. *IBM Journal of Research and Development* **32,** 306–316 (1988).

75. Büttiker, M. Four-terminal phase-coherent conductance. *Physical review letters* **57,** 1761 (1986).

76. Beenakker, C. & van Houten, H. Quantum transport in semiconductor nanostructures. *Solid state physics* **44,** 1–228 (1991).

77. Glazman, L., Lesovik, G., Khmel'nitskii, D. & Shekhter, R. Reflectionless quantum transport and fundamental ballistic-resistance steps in microscopic constrictions. *ZhETF Pisma Redaktsiiu* **48,** 218 (1988).

78. Yacoby, A. & Imry, Y. Quantization of the conductance of ballistic point contacts beyond the adiabatic approximation. *Physical Review B* **41,** 5341 (1990).

79. Dietl, T., Ohno, o. H., Matsukura, a. F., Cibert, J. & Ferrand, e. D. Zener model description of ferromagnetism in zinc-blende magnetic semiconductors. *science* **287,** 1019–1022 (2000).

80. Dietl, T., Ohno, o. H. & Matsukura, F. Hole-mediated ferromagnetism in tetrahedrally coordinated semiconductors. *Physical Review B* **63,** 195205 (2001).

81. Esaki, L. New phenomenon in narrow germanium p- n junctions. *Physical review* **109,** 603 (1958).

82. MacDonald, A., Schiffer, r. P. & Samarth, h. N. Ferromagnetic semiconductors: moving beyond (ga, mn) as. *Nature materials* **4,** 195–202 (2005).

83. Oiwa, A. *et al.* Low-temperature conduction and giant negative magnetoresistance in III–V-based diluted magnetic semiconductor:(Ga, Mn) As/GaAs. *Physica B: Condensed Matter* **249,** 775–779 (1998).

84. Oiwa, A., Mitsumori, Y., Moriya, R., Słupinski, T. & Munekata, H. Effect of optical spin injection on ferromagnetically coupled Mn spins in the III-V magnetic alloy semiconductor (Ga,Mn)As. *Physical review letters* **88,** 137202 (2002).

85. Chiba, D., Matsukura, F. & Ohno, H. Electric-field control of ferromagnetism in (Ga,Mn)As. *Applied Physics Letters* **89** (2006).

86. Lee, S. *et al.* Effect of Be doping on the properties of GaMnAs ferromagnetic semiconductors. *Journal of applied physics* **93,** 8307–8309 (2003).

87. Yuldashev, S. U. *et al.* Effect of additional nonmagnetic acceptor doping on the resistivity peak and the Curie temperature of Ga 1- x Mn x As epitaxial layers. *Applied physics letters* **82,** 1206–1208 (2003).

88. Zemen, J., Kučera, J., Olejník, K. & Jungwirth, T. Magnetocrystalline anisotropies in (Ga, Mn) As: Systematic theoretical study and comparison with experiment. *Physical Review B* **80,** 155203 (2009).

89. Sawicki, M. *et al.* Temperature dependent magnetic anisotropy in (Ga, Mn) As layers. *Physical Review B* **70,** 245325 (2004).

90. Sawicki, M. Magnetic properties of (Ga, Mn) As. *Journal of magnetism and magnetic materials* **300,** 1–6 (2006).

91. Abolfath, M., Jungwirth, T., Brum, J. & MacDonald, A. Theory of magnetic anisotropy in III 1- x Mn x V ferromagnets. *Physical Review B* **63,** 054418 (2001).

92. Gould, C. *et al.* An extensive comparison of anisotropies in MBE grown (Ga, Mn) As material. *New Journal of Physics* **10,** 055007 (2008).

93. Lee, S., Chung, J.-H., Liu, X., Furdyna, J. K. & Kirby, B. J. Ferromagnetic semiconductor GaMnAs. *Materials Today* **12,** 14–21 (2009).

94. Hümpfner, S. *et al.* Lithographic engineering of anisotropies in (Ga, Mn) As. *Applied Physics Letters* **90** (2007).

95. Wunderlich, J. *et al.* Local control of magnetocrystalline anisotropy in (Ga, Mn) As microdevices: Demonstration in current-induced switching. *Physical Review B* **76,** 054424 (2007).

96. Hoffmann, F. *et al.* Mapping the magnetic anisotropy in (Ga, Mn) As nanostructures. *Physical Review B* **80,** 054417 (2009).

97. Wenisch, J. *et al.* Control of magnetic anisotropy in (Ga, Mn) As by lithography-induced strain relaxation. *Physical review letters* **99,** 077201 (2007).

98. Ohno, Y. *et al.* Electrical spin injection in a ferromagnetic semiconductor heterostructure. *Nature* **402,** 790–792 (1999).

99. Kohda, M., Ohno, Y., Takamura, K., Matsukura, F. & Ohno, H. A spin Esaki diode. *Japanese Journal of Applied Physics* **40,** L1274 (2001).

100. Johnston-Halperin, E. *et al.* Spin-polarized Zener tunneling in (Ga, Mn) As. *Physical Review B* **65,** 041306 (2002).

101. Umansky, V., De-Picciotto, R. & Heiblum, M. Extremely high-mobility two dimensional electron gas: Evaluation of scattering mechanisms. *Applied physics letters* **71,** 683–685 (1997).

102. Hwang, E. & Sarma, S. D. Limit to two-dimensional mobility in modulation-doped GaAs quantum structures: How to achieve a mobility of 100 million. *Physical Review B* **77,** 235437 (2008).

103. Oltscher, M. Spininjektion in zweidimensionale Elektronengase. *Master's Thesis* (2011).

104. Störmer, H., Dingle, R., Gossard, A., Wiegmann, W. & Sturge, M. Two-dimensional electron gas at a semiconductor-semiconductor interface. *Solid state communications* **29,** 705–709 (1979).

105. Nathan, M. I. Persistent photoconductivity in AlGaAs/GaAs modulation doped layers and field effect transistors: a review. *Solid-State Electronics* **29,** 167–172 (1986).

106. Mooney, P. Deep donor levels (DX centers) in III-V semiconductors. *Journal of Applied Physics* **67,** R1–R26 (1990).

107. Kane, M., Apsley, N., Anderson, D., Taylor, L. & Kerr, T. Parallel conduction in GaAs/AlxGa1-xAs modulation doped heterojunctions. *Journal of Physics C: Solid State Physics* **18,** 5629 (1985).

108. Ciorga, M., Utz, M., Schuh, D., Bougeard, D. & Weiss, D. Effect of contact geometry on spin-transport signals in nonlocal (Ga, Mn) As/GaAs devices. *Physical Review B* **88,** 155308 (2013).

109. Baca, A. G. & Ashby, C. I. *Fabrication of GaAs devices* **6** (IET, 2005).

110. Jäger, O. Effect of the Channel Geometry on Spin Signals in Lateral Spin Injection Devices. *Master's Thesis* (2022).

111. Wieand, M. Conductance Quantization in the High Spin-Orbit-Coupling Material InGaAs/InAlAs. *Master's Thesis* (2018).

112. Tombros, N., Van Der Molen, S. & Van Wees, B. Separating spin and charge transport in single-wall carbon nanotubes. *Physical Review B* **73,** 233403 (2006).

113. Jedema, F. J., Filip, A. & Van Wees, B. Electrical spin injection and accumulation at room temperature in an all-metal mesoscopic spin valve. *Nature* **410,** 345–348 (2001).

114. Bakker, F., Slachter, A., Adam, J.-P. & Van Wees, B. Interplay of Peltier and Seebeck effects in nanoscale nonlocal spin valves. *Physical review letters* **105,** 136601 (2010).

115. Johnson, M. & Silsbee, R. Calculation of nonlocal baseline resistance in a quasi-one-dimensional wire. *Physical Review B* **76,** 153107 (2007).

116. Garzon, S., Žutić, I. & Webb, R. A. Temperature-dependent asymmetry of the nonlocal spin-injection resistance: Evidence for spin nonconserving interface scattering. *Physical review letters* **94,** 176601 (2005).

117. Kuczmik, T. *et al.* Hanle spin precession in a two-dimensional electron system. *Physical Review B* **95,** 195315 (2017).

118. Thornton, T., Pepper, M., Ahmed, H., Andrews, D. & Davies, G. One-dimensional conduction in the 2D electron gas of a GaAs-AlGaAs heterojunction. *Physical review letters* **56,** 1198 (1986).

119. Zheng, H., Wei, H., Tsui, D. & Weimann, G. Gate-controlled transport in narrow GaAs/Al x Ga 1- x As heterostructures. *Physical Review B* **34,** 5635 (1986).

120. Van Wees, B. J. *et al.* Quantum ballistic and adiabatic electron transport studied with quantum point contacts. *Physical Review B* **43,** 12431 (1991).

121. Wharam, D. *et al.* Empirical relation between gate voltage and electrostatic potential in the one-dimensional electron gas of a split-gate device. *Physical Review B* **39,** 6283 (1989).

122. Nixon, J. A. & Davies, J. H. Potential fluctuations in heterostructure devices. *Physical Review B* **41,** 7929 (1990).

123. Williamson, J., Timmering, C., Harmans, C., Harris, J. & Foxon, C. Quantum point contact as a local probe of the electrostatic potential contours. *Physical Review B* **42,** 7675 (1990).

124. Smith, L. *et al.* *Disorder and interaction effects in quantum wires* in *Journal of Physics: Conference Series* **376** (2012), 012018.

125. Yakimenko, I. I. & Berggren, K.-F. Probing dopants in wide semiconductor quantum point contacts. *Journal of Physics: Condensed Matter* **28,** 105801 (2016).

126. Thomas, K. *et al.* Ballistic transport in one-dimensional constrictions formed in deep two-dimensional electron gases. *Applied physics letters* **67,** 109–111 (1995).

127. Patel, N. *et al.* Ballistic transport in one dimension: additional quantisation produced by an electric field. *Journal of Physics: Condensed Matter* **2,** 7247 (1990).

128. Patel, N. *et al.* Evolution of half plateaus as a function of electric field in a ballistic quasi-one-dimensional constriction. *Physical review B* **44,** 13549 (1991).

129. Rössler, C. *et al.* Transport properties of clean quantum point contacts. *New Journal of Physics* **13,** 113006 (2011).

130. Rössler, C., Herz, M., Bichler, M. & Ludwig, S. Freely suspended quantum point contacts. *Solid State Communications* **150,** 861–864 (2010).

131. Van Houten, H. & Beenakker, C. Quantum point contacts. *Physics today* **49,** 22–27 (1996).

132. Stano, P., Fabian, J. & Jacquod, P. Nonlinear spin to charge conversion in mesoscopic structures. *Physical Review B* **85,** 241301 (2012).

133. Stano, P. & Jacquod, P. Spin-to-charge conversion of mesoscopic spin currents. *Physical Review Letters* **106,** 206602 (2011).

134. Nichele, F. *et al.* Generation and detection of spin currents in semiconductor nanostructures with strong spin-orbit interaction. *Physical Review Letters* **114,** 206601 (2015).

135. Marcellina, E. *et al.* Nonlinear spin filter for nonmagnetic materials at zero magnetic field. *Physical Review B* **102,** 140406 (2020).

136. Bardarson, J., Adagideli, I. & Jacquod, P. Mesoscopic spin Hall effect. *Physical review letters* **98,** 196601 (2007).

137. Hirsch, J. Spin hall effect. *Physical review letters* **83,** 1834 (1999).

138. Brüne, C. *et al.* Evidence for the ballistic intrinsic spin Hall effect in HgTe nanostructures. *Nature Physics* **6,** 448–454 (2010).

139. Hankiewicz, E., Molenkamp, L., Jungwirth, T. & Sinova, J. Manifestation of the spin Hall effect through charge-transport in the mesoscopic regime. *Physical Review B* **70,** 241301 (2004).

140. Van Houten, H., Molenkamp, L., Beenakker, C. & Foxon, C. Thermoelectric properties of quantum point contacts. *Semiconductor Science and Technology* **7,** B215 (1992).

141. Sivan, U. & Imry, Y. Multichannel Landauer formula for thermoelectric transport with application to thermopower near the mobility edge. *Physical review b* **33,** 551 (1986).

142. Mott, N. & Jones, H. *The Theory of the Properties of Metals and Alloys* ISBN: 9780486604565 (Dover Publications, 1958).

143. Molenkamp, L., Van Houten, H., Beenakker, C., Eppenga, R. & Foxon, C. Quantum oscillations in the transverse voltage of a channel in the nonlinear transport regime. *Physical Review Letters* **65,** 1052 (1990).

144. Dzurak, A. *et al.* Thermopower of a one-dimensional ballistic constriction in the non-linear regime. *Journal of Physics: Condensed Matter* **5,** 8055 (1993).

145. Proetto, C. Thermopower oscillations of a quantum-point contact. *Physical review B* **44,** 9096 (1991).

146. Appleyard, N., Nicholls, J., Simmons, M., Tribe, W. & Pepper, M. Thermometer for the 2D electron gas using 1D thermopower. *Physical review letters* **81,** 3491 (1998).

147. Rejec, T. & Meir, Y. Magnetic impurity formation in quantum point contacts. *Nature* **442,** 900–903 (2006).

148. Iqbal, M. *et al.* Odd and even Kondo effects from emergent localization in quantum point contacts. *Nature* **501,** 79–83 (2013).

149. Wang, C.-K. & Berggren, K.-F. Spin splitting of subbands in quasi-one-dimensional electron quantum channels. *Physical Review B* **54,** R14257 (1996).

150. Bauer, F. *et al.* Microscopic origin of the '0.7-anomaly' in quantum point contacts. *Nature* **501,** 73–78 (2013).

151. Micolich, A. What lurks below the last plateau: experimental studies of the 0.7× $2e^2/h$ conductance anomaly in one-dimensional systems. *Journal of Physics: Condensed Matter* **23,** 443201 (2011).

152. Thomas, K. *et al.* Possible spin polarization in a one-dimensional electron gas. *Physical Review Letters* **77,** 135 (1996).

153. Smith, L. *et al.* Statistical study of conductance properties in one-dimensional quantum wires focusing on the 0.7 anomaly. *Physical Review B* **90,** 045426 (2014).

154. Oltscher, M. *et al.* Gate-tunable large magnetoresistance in an all-semiconductor spin valve device. *Nature Communications* **8,** 1807 (2017).

155. Chen, K. & Zhang, S. Enhancement of spin accumulation in ballistic transport regime. *Physical Review B* **92,** 214402 (2015).

156. Jaffrès, H., George, J.-M. & Fert, A. Spin transport in multiterminal devices: Large spin signals in devices with confined geometry. *Physical Review B* **82,** 140408 (2010).

157. Liang, C.-T., Pepper, M., Simmons, M., Smith, C. & Ritchie, D. Spin-dependent transport in a quasiballistic quantum wire. *Physical Review B* **61,** 9952 (2000).

Danksagung

Ich möchte mich bei verschiedenen Personen für die Unterstützung bei dieser Arbeit bedanken. Beginnend bei **Prof. Dr. Dieter Weiss** für die Möglichkeit, meine Arbeit an seinem Lehrstuhl durchzuführen. Am Lehrstuhl war stets eine freundliche, produktive Atmosphäre und ich hatte jederzeit das Gefühl, dass ich bei Problemen zu Herrn Weiss kommen kann.

Prof. Dr. Mariusz Ciorga gilt mein Dank für das Ausschreiben des Themas, für die Betreuung und die zahlreichen fachlichen Diskussionen über die Jahre. Mariusz hatte jederzeit gute Beiträge zu meinen Ideen, Messergebnissen und Lösungsansätze für Schwierigkeiten.

Für die Korrektur meiner Arbeit, sowie das bereit erklären zur Prüfung gilt mein Dank **Prof. Dr. Jaroslav Fabian**, **Prof. Dr. Jörg Wunderlich** und **Prof. Dr. Franz J. Gießibl**.

Meinen Masterstudenten, **Ole Jäger** und **Adrian Vanselow** will ich für ihre Zeit und Engagement zu dem Thema danken. Dank gilt auch ihrer Geduld mir gegenüber und dem, was ich durch die Betreuung lernen durfte.

Franz Eberle und **Albert Koop** gilt besonderer Dank für die Einarbeitung und Hilfestellung sowohl im Reinraum als auch im Magnetlabor. Vor allem Albert hat mir mit viel Geduld und Passion geholfen.

Dr. Dmitriy Kozlov gilt mein Dank für fachliche Diskussionen und einer angenehmen gemeinsamen Zeit im Büro. Mein größter Dank gilt Dima für Hilfe beim Aufbau meines Messsetups.

Für jegliche Hilfe während meiner Zeit an der Universität Regensburg möchte ich allen Mitgliedern und Angestellten des Lehrstuhls danken, sowie der Hilfe von Personen außerhalb des Lehrstuhls.

Für emotionale Unterstützung danke ich vor allem meiner Freundin, **Mona Wieland**, die immer ein offenes Ohr hatte und niemals müde wurde, mir zuzuhören (immer und immer und immer wieder). Dazu gilt mein Dank **meinen Eltern**, welche mir mein Studium, sowie meinen kompletten Werdegang ermöglicht haben, sowie meiner gesamten Familie.

Besonderer Dank gilt **Jan Bärenfänger** und **Stefan Hartl** für die gute gemeinsame Zeit im Arbeitsalltag.